Possible formation of QGP droplets in high-multiplicity events and measurement of ψ(2S) polarization in proton+proton collisions at $\sqrt{s}$ = 13 TeV with ALICE

Ph.D. Thesis

By

Dushmanta Sahu

DEPARTMENT OF PHYSICS

INDIAN INSTITUTE OF TECHNOLOGY INDORE

June 2024

Possible formation of QGP droplets in high-multiplicity events and measurement of ψ(2S) polarization in proton+proton collisions at $\sqrt{s}$ = 13 TeV with ALICE

A THESIS

Submitted in partial fulfilment of the requirements

for the award of the degree

of

DOCTOR OF PHILOSOPHY

By

Dushmanta Sahu

DEPARTMENT OF PHYSICS

INDIAN INSTITUTE OF TECHNOLOGY INDORE

June 2024

INDIAN INSTITUTE OF TECHNOLOGY INDORE

I hereby certify that the work which is being presented in the thesis entitled **"POSSIBLE FORMATION OF QGP DROPLETS IN HIGH-MULTIPLICITY EVENTS AND MEASUREMENT OF ψ(2S) POLARIZATION IN PROTON+PROTON COLLISIONS AT $\sqrt{s}$= 13 TeV WITH ALICE"** in the partial fulfilment of the requirements for the award of the degree of **DOCTOR OF PHILOSOPHY** and submitted in the **DEPARTMENT OF PHYSICS, Indian Institute of Technology Indore**, is an authentic record of my own work carried out during the time period from June 2019 to March 2024 under the supervision of Prof. Raghunath Sahoo, Professor, Department of Physics, Indian Institute of Technology Indore, M.P., India.

The matter presented in this thesis has not been submitted by me for the award of any other degree of this or any other institute.

Dushmanta Sahu
26.03.2024
signature of the student with date
(DUSHMANTA SAHU)

This is to certify that the above statement made by the candidate is correct to the best of my knowledge.

Sahoo 14.06.2024
Signature of Thesis Supervisor date
(Prof. RAGHUNATH SAHOO)

Mr. DUSHMANTA SAHU has successfully given his/her Ph.D. Oral Examination held on 14 June 2024

Sahoo 14.06.24
Signature of Thesis Supervisor date
(Prof. RAGHUNATH SAHOO)

Dedicated to my father

ACKNOWLEDGEMENTS

I am profoundly grateful to the incredible individuals who have been instrumental in the completion of my PhD thesis. I have learned so much from the interactions and support that I have had with everyone during my time in this institute. Their unwavering support and encouragement have made this academic journey not only possible but also immensely rewarding.

First and foremost, I am incredibly indebted to my supervisor, Prof. Raghunath Sahoo, whose dedicated guidance and expertise have been a guiding light throughout my journey. Your mentorship has been transformative, pushing me to surpass my own expectations and fostering a sense of resilience in the face of all the academic challenges. I will surely cherish our both professional and social interactions which have been really enjoyable for me. I have learned so much from you that I should remain forever indebted.

I also feel privileged to take part in one of the experiments (ALICE) at the Large Hadron Collider. This was a dream come true. I would like to thank the convenors of the Dilepton and Quarkonia physics working group (PWG-DQ) and co-ordinators of the QQ2MuMu physics analysis group in ALICE, especially Dr. Laure Marie Masscrier, Dr. Fiorella Fionda, Dr. Maxime Guillbaud and Dr. Luca Michelleti for their help in data analyses. I would also like to thank the conference committee chairs of the ALICE collaboration for giving me opportunities to represent the ALICE collaboration on multiple occasions at international/national conferences. I would also like to thank my analysis review committee: Dr. Maxime Guillbaud, and Dr. Chvetan for reviewing my analyses and for their constructive comments and suggestions.

I would like to thank my PSPC committee members Prof. Subhendu Rakshit and Prof. Chelvam Venkatesh for their support and motivation. I would also

like to thank all the faculty and staff members of IIT Indore for their support. I am very grateful to the Department of Physics, IIT Indore for providing me with all the required resources. I extend my deepest appreciation to my fellow lab-mates of the Experimental High Energy Physics lab at IIT Indore whose camaraderie and intellectual discussions have shaped my research and broadened my perspectives. In particular, I would like to express my gratitude towards Sushanta bhai, Dhananjaya bhai, Arvind bhai, Suman bhaiya, Aditya bhaiya, and Rutuparna didi who have guided me in some way or another during this journey. I also feel grateful to have been sharing the working space with Captain bhaiya, Jayanta bhaiya, Neelkamal, Girija, Ronald, Suraj, Debadatta, Kshitish, Bhagyarathi, Kamaljeet, Kangkan, Ashwathy, and Poornima. In addition, I also feel privileged to have collaborated with Dr. Swatantra Tiwari, Prof. Jan-e Alam, Prof. Reinhard Stock, and the late Prof. Jean Cleymans. Your insights and collaborative spirit have been invaluable, making the academic process both stimulating and enjoyable.

I also want to thank my friends, Sanjay, Debasis, Satya, Siddharth, and Sunil whose emotional support and understanding during the peaks and valleys of this journey have been a constant source of strength. Your belief in me, even when my own wavered, has been a beacon of motivation.

Lastly, my gratitude extends to my family, whose unwavering love and encouragement have been the bedrock of the pursuits of my life. Your sacrifices, understanding, and belief in me have been my greatest motivation. In acknowledging these individuals, and many more whom I haven't mentioned here, I recognize the collective effort that has shaped my academic achievement. This thesis stands as a testament to the power of collaboration, mentorship, and the unyielding support of our loved ones. Thank you all for being an integral part of this significant chapter in my life. May the force be with you.

(**Dushmanta Sahu**)

ABSTRACT

The main goal of the Large Hadron Collider (LHC) is to understand nature at the fundamental level. Through LHC, one can also study the behaviour of matter at extremely high temperatures and densities. This can be achieved by the collision of ultra-relativistic heavy-ions where quantum chromodynamics (QCD) predicts the formation of a new state of matter called the quark-gluon plasma (QGP). QGP is a thermalized soup of quarks and gluons which is expected to be prevalent in the early stage of the Universe, after a few microseconds of the Big Bang. Historically, the proton+proton (pp) collisions were taken as baseline measurements for QGP production in heavy-ion collisions, as their system size is significantly smaller than that of the heavy-ion collisions. However, recent measurements of strangeness enhancement and ridge-like structure formation in high multiplicity pp events have opened Pandora's box, which raises the question about the viability of using pp collisions as a baseline for the QGP study. Studying the formation of a QGP-like medium in hadronic collisions will help us better understand the experimental data. Thus, it is crucial to approach this problem in a two-fold manner. Firstly, one needs to study the possibility of QGP droplet formation in ultra-relativistic high multiplicity pp collisions through various theoretical and phenomenological models. Secondly, we should look into the experimental data and study the necessary observables that can point us in a conclusive direction in this context.

The study of thermodynamic and transport properties is of utmost importance in understanding the matter formed in ultra-relativistic collisions. Knowledge about the initial energy density (ϵ) can tell us whether the system can be possibly deconfined or not. Similarly, the squared speed of sound (c_s^2) helps us to characterize the system. The mean free path (λ) on the other hand gives us information about the possible thermalization in a medium. The isothermal compressibility (κ_{T}) can tell us about the system's deviation from a perfect fluid.

Moreover, transport properties like shear viscosity to entropy density ratio (η/s) and bulk viscosity to entropy density ratio (ζ/s) can tell us about the fluidity of the system. All these observables together can help us characterize the systems formed in an ultra-relativistic collision and can suggest whether there is a change in dynamics after a certain temperature. Additionally, one can study the jet transport parameter, which is related to jet quenching in the medium. Experimentally, jet quenching has not been observed in pp collisions. Thus, the study of jet transport parameter through various phenomenological approaches can bring essential insights. In this thesis, we take the well-established QCD-inspired color string percolation model (CSPM) and study various thermodynamic and transport properties, which help us to understand the system produced in hadronic and heavy-ion collisions.

In addition, one can also explore the hadronic phase lifetime of the systems from low multiplicity pp collisions to most central heavy-ion collisions. Resonances can be used to study various phases of the hadronic and heavy-ion collision evolution. In this thesis, we estimate the hadronic phase lifetime using a nuclear decay-inspired toy model by using the resonance K^{*0} as a probe. We also use another resonance, ϕ, to locate the QGP phase boundary. We fit the Boltzmann-Gibbs Blastwave function to the soft part of the transverse momentum spectra of ϕ and extract the thermal temperature and the average velocity. We finally estimate the effective temperature, which helps us understand how the system is formed in ultra-relativistic collisions.

For the experimental part of this thesis, we have studied ψ(2S) polarization in pp collisions at $\sqrt{s} = 13$ TeV with ALICE at the LHC. The study of polarization in hadronic collisions can help us to understand the production processes involved. There are various conflicting theoretical estimations for charmonia polarization, whereas the experiments show no polarization in pp collisions at $\sqrt{s} = 7$ and 8 TeV. Thus, one must study charmonia polarization at a higher center of mass energy with better statistics to reach a formal conclusion. Moreover, polarization

in pp collisions can be used as a benchmark for polarization studies in heavy-ion collisions where the effects of external magnetic field, initial angular momentum and the impact of QGP can be expected. We study the ψ(2S) through the dimuon decay channel with the help of the ALICE muon spectrometer. The polarization parameters can be extracted from the angular distribution of the dimuons. For our analysis, we chose two different frames of reference to remove the frame-dependent biases. Finally, we report our estimation and compare our results with various theoretical models.

The primary objective of this thesis is to study and understand polarization of charmonia, specifically ψ(2S) meson, in pp collisions at $\sqrt{s} = 13$ TeV with ALICE at the LHC. In addition, we take the phenomenological CSPM approach to study the matter formed in ultra-relativistic collisions. We also estimate the hadronic phase lifetime and locate the QGP phase boundary using resonances. This thesis is divided into five chapters. The organization of the thesis is as follows:

- **Chapter 1** briefly introduces Quantum Chromodynamics, Quark-Gluon plasma and the physics of heavy-ion collisions. Moreover, the motivation for the thesis is also presented here.

- **Chapter 2** discusses the color string percolation model. It gives the formulation of CSPM and then proceeds to estimate various thermodynamic and transport properties within the CSPM approach. In this chapter, we study the change in dynamics of the medium from hadronic to heavy-ion collisions, which can give us hints about the possible formation of QGP droplets in high multiplicity pp collisions.

- **Chapter 3** is dedicated to studying the hadronic phase lifetime and how it can be estimated. It discusses how resonances can be used to probe different phases of heavy-ion collisions. Then, a detailed description of the Boltzmann-Gibbs blastwave function is given, which is used to fit the ϕ

transverse momentum spectra to estimate the effective temperature, which gives information about the QGP phase boundary.

- **Chapter 4** discusses the study of ψ(2S) polarization in pp collisions at $\sqrt{s}$ = 13 TeV with the ALICE experiment. We briefly introduce the ALICE experiment at LHC, mainly the muon spectrometer, which is used for our analysis. We then give a brief theoretical formulation of charmonia polarization. Then, we discuss our experimental methods to extract the polarization parameters. Finally, we report our results and compare with existing theoretical estimations.

- **Chapter 5** summarizes our studies that have been done in this thesis with an outlook.

PUBLICATIONS

List of publications: (Publications marked with * are included in this thesis)

1. * D. Sahu, S. Tripathy, G. S. Pradhan and R. Sahoo, "Role of event multiplicity on hadronic phase lifetime and QCD phase boundary in ultra-relativistic collisions at energies available at the BNL Relativistic Heavy Ion Collider and CERN Large Hadron Collider", Phys. Rev. C 101, 014902 (2020)

2. * D. Sahu and R. Sahoo, "Thermodynamic and Transport Properties of Matter Formed in pp, p-Pb, Xe-Xe and Pb-Pb Collisions at the Large Hadron Collider using Color String Percolation Model", J. Phys. G 48, 125104 (2021)

3. * D. Sahu, S. Tripathy, R. Sahoo and S. K. Tiwari, "Formation of a Perfect Fluid in pp, p-Pb, Xe-Xe and Pb-Pb Collisions at the Large Hadron Collider Energies", Eur. Phys. J. A 58, 78 (2022)

4. * A. N. Mishra, D. Sahu and R. Sahoo, "Jet Transport Coefficient at the Large Hadron Collider Energies in a Color String Percolation Approach", MDPI Physics 4, 315 (2022)

5. * D. Sahu and R. Sahoo, "ψ(2S) polarization measurement in pp collisions at $\sqrt{s} = 13$ TeV", https://alice-notes.web.cern.ch/node/1472 (ALICE internal)

6. D. Sahu, S. Tripathy, R. Sahoo and A. R. Dash, "Multiplicity Dependence of Shear Viscosity, Isothermal Compressibility and Speed of Sound in pp collisions at $\sqrt{s} = 7$ TeV", Eur. Phys. J. A 56, 187 (2020)

7. D. Sahu and R. Sahoo, "Characterizing High-Energy pp Collisions at the Large Hadron Collider using Thermal Properties", MDPI Physics 3, 207 (2021)

8. S. Deb, D. Sahu, R. Sahoo and A. K. Pradhan, "Bose-Einstein Condensation of pions in Proton-Proton collisions at the Large Hadron Collider", Eur. Phys. J. A 57, 158 (2021)

9. K. Goswami, D. Sahu and R. Sahoo, "Understanding the QCD medium by the diffusion of charm quarks using Color String Percolation Model", Phys. Rev. D 107, 014003 (2023)

10. K. K. Pradhan, D. Sahu, R. Scaria and R. Sahoo, "Conductivity, diffusivity, and violation of Wiedemann-Franz Law in a hadron resonance gas with van der Waals interactions", Phys. Rev. C 107, 014910 (2023)

11. G. S. Pradhan, D. Sahu, S. Deb and R. Sahoo, "Hadron gas in the presence of a magnetic field using non-extensive statistics: A transition from diamagnetic to paramagnetic system", J. Phys. G 50, 055104 (2023)

12. R. Scaria, D. Sahu, C. R. Singh, R. Sahoo and J. e. Alam, "Fluidity of the system produced in relativistic pp and heavy-ion collisions: Hadron resonance gas model approach", Eur. Phys. J. A 59, 140 (2023)

13. B. Sahoo, C. R. Singh, D. Sahu, R. Sahoo and J. e. Alam, "Impact of vorticity and viscosity on the hydrodynamic evolution of hot QCD medium", Eur. Phys. J. C 83, 873 (2023)

14. K. Goswami, K. K. Pradhan, D. Sahu and R. Sahoo, "Diffusion and fluctuations of open charmed hadrons in an interacting hadronic medium", Phys. Rev. D **108**, 074011 (2023).

15. B. Sahoo, K. K. Pradhan, D. Sahu and R. Sahoo, "Effect of magnetic field on the thermodynamic properties of a high-temperature hadron resonance gas with van der Waals interactions", Phys. Rev. D **108**, 074028 (2023).

16. G. S. Pradhan, D. Sahu, R. Rath, R. Sahoo and J. Cleymans, "Role of chemical potential at kinetic freeze-out using Tsallis non-extensive statistics in proton-proton collisions at the Large Hadron Collider", Eur. Phys. J. A **60**, 52 (2024).

17. B. Sahoo, K. K. Pradhan, D. Sahu and R. Sahoo, "J/ψ and ψ(2S) polarization in proton-proton collisions at the LHC energies using PYTHIA8", Phys. Rev. C **109**, 034910 (2024).

18. K. Goswami, D. Sahu, J. Dey, R. Sahoo and R. Stock, "Anisotropy of magnetized quark matter", arXiv:2310.02711 (Accepted in PRD).

19. K. K. Pradhan, D. Sahu, C. R. Singh and R. Sahoo, "Effect of Bose-Einstein condensation on the viscosity of a hot pion gas", arXiv:2212.09288

20. K. K. Pradhan, B. Sahoo, D. Sahu and R. Sahoo, "Thermodynamics of a rotating hadron resonance gas with van der Waals interaction", arXiv:2304.05190

21. K. K. Pradhan, R. Scaria, D. Sahu and R. Sahoo, "Proton number cumulants in a modified van der Waals hadron resonance gas", arXiv:2308.09337

22. 158 other publications in collaboration with ALICE.

Conference Proceedings:

1. D. Sahu, S. Tripathy, G. S. Pradhan and R. Sahoo, "Hadronic Phase Lifetime and QCD Phase boundary in Ultra-relativistic Collisions at the RHIC and LHC: Collision System and Event Multiplicity Dependence", DAE Symp. Nucl. Phys. 64, 754 (2020) **(Best poster)**.

2. D. Sahu, A. N. Mishra and R. Sahoo, "Study of the jet transport coefficient at the Large Hadron Collider energies using Color String Percolation Model", PoS LHCP 2021, 232 (2021).

3. D. Sahu and R. Sahoo, "Dissipative properties of the matter formed at the Large Hadron Collider energies using Color String Percolation Model", DAE Symp. Nucl. Phys. 65, 626 (2022).

4. D. Sahu, S. Tripathy, R. Sahoo and S. K. Tiwari, "Multiplicity Dependence Study of Thermodynamic and Transport Properties of the Matter Formed in Ultra-Relativistic Collisions at LHC Using Color String Percolation Model", Springer Proc. Phys. 277, 369 (2022).

5. D. Sahu, S. Tripathy, G. S. Pradhan and R. Sahoo, "Estimation of Hadronic Phase Lifetime and Locating the QGP Phase Boundary", Int. J. M. Phys. E 31, 2250097 (2022).

6. K. K. Pradhan, D. Sahu, R. Scaria and R. Rahoo, "Electrical and thermal conductivities in a hadron resonance gas with van der Waals interactions", DAE Symp. Nucl. Phys. 66, 853 (2023).

7. R. Scaria, D. Sahu, C. R. Singh, R. Sahoo and J. e. Alam, "Probing thermalization and system size effect on a hadron resonance gas for hydrodynamical study of hadronic phase", DAE Symp. Nucl. Phys. 66, 948 (2023).

8. K. Goswami, D. Sahu and R. Sahoo, "Studying the diffusion of charm quarks in a deconfined medium using Color String Percolation approach", DAE Symp. Nucl. Phys. 66, 936 (2023).

9. G. S. Pradhan, D. Sahu, S. Deb and R. Sahoo, Insight into the magnetic response of hadron gas using non-extensive statistics, PoS LHCP 2022, 327 (2023).

10. S. Deb, D. Sahu, R. Sahoo and A. K. Pradhan, Hint of pion condensation in proton-proton collisions at the LHC using non-extensive Tsallis statistics, PoS LHCP 2022, 253 (2023).

11. R. Scaria, D. Sahu, C. R. Singh, R. Sahoo and J. e. Alam, Fluid properties of hadron gas produced in relativistic hadronic and heavy-ion collisions, PoS LHCP 2022, 332 (2023).

12. C. R. Singh, B. Sahoo, D. Sahu, R. Sahoo and J. e. Alam, "How do coupled viscosity, vorticity and magnetic field govern the QGP evolution?," DAE Symp. Nucl. Phys. **67**, 985 (2024).

13. B. Sahoo, K. K. Pradhan, D. Sahu and R. Sahoo, "Refractive index of the hadronic medium in presence of a magnetic field," DAE Symp. Nucl. Phys. **67**, 885 (2024).

14. G. S. Pradhan, D. Sahu, S. Deb and R. Sahoo, "Magnetic Field Effects in Hadron Gas: Non-Extensive Insights," DAE Symp. Nucl. Phys. **67**, 1063 (2024).

15. G. S. P. Pradhan, D. Sahu, R. Rath, R. Sahoo and J. Cleymans, "Decoding Chemical Potential Effects at the Kinetic Freeze-Out through Tsallis Non-Extensive Statistics at the LHC," DAE Symp. Nucl. Phys. **67**, 1065 (2024).

16. K. Goswami, K. K. Pradhan, D. Sahu and R. Sahoo, "Dynamics of charmed hadron in an interacting hadron gas," DAE Symp. Nucl. Phys. **67**, 883 (2024).

17. K. Pradhan, R. Scaria, D. Sahu and R. Sahoo, "Higher order proton number fluctuations in a modified van der Waals hadron resonance gas model," DAE Symp. Nucl. Phys. **67**, 887 (2024).

18. D. Sahu and R. Sahoo, "Is there a threshold in the final state charged particle multiplicity to form a plasma of quarks and gluons?," DAE Symp. Nucl. Phys. **67**, 1051 (2024).

19. B. Sahoo, S. Deb, D. Sahu, C. R. Singh and R. Sahoo, "Exploring J/ψ and ψ(2S) polarization dynamics in pp collisions at the LHC energies with PYTHIA8," DAE Symp. Nucl. Phys. **67**, 1035 (2024) **(Best poster)**.

20. D. Sahu, "Quarkonium polarization in pp and Pb-Pb collisions," DAE Symp. Nucl. Phys. **67**, 1053 (2024).

Contents

Figures

Chapter 1

Introduction

The most common school of thought regarding the creation of our universe is that it all started with a big bang nearly 13.7 billion years ago. In the infancy of the universe, when the condition was extremely hot and dense, it was supposed to be filled with a unique state of matter called the quark-gluon plasma (QGP). To understand the behavior of this matter, one needs to move towards collider physics, where heavy-ions such as lead (Pb) and gold (Au) are collided, creating little bangs, which briefly produce QGP in the laboratory. Thus, one can study heavy-ion collisions to understand the early universe scenario. However, to gain a better hold of this topic, one also needs to venture into the world of particle physics and study the forces that govern the universe.

There are four fundamental forces of nature, namely the strong force, the electromagnetic force, the weak force and the gravitational force. Apart from gravity, all the other forces are very well described by the Standard Model of particle physics. Ultra-relativistic collisions at the Large Hadron Collider (LHC) at the European Center for Nuclear Research (CERN) and the Relativistic Heavy Ion Collider (RHIC) at Brookhaven National Laboratory (BNL) can create a short-lived, strongly interacting, thermalized, deconfined state of matter called the QGP. Quantum Chromodynamics (QCD) is the widely accepted theory to understand matter undergoing strong interaction. It is a non-abelian gauge the-

ory, meaning the gauge bosons are self-interacting. The underlying symmetry group of QCD is SU(3), consisting of eight generators of the group, called gluons. The gluons and the quarks are the fundamental particles that participate in the strong interaction. Gluons are massless bosons with spin-1, whereas the quarks have finite masses and are fermions with spin-1/2. There are three generations of quarks, with each generation having two flavors; the up (u) and down (d), charm (c) and strange (s), top (t) and bottom (b). All the gluons have zero electric charges; however, the u, c, t quarks have $(+\frac{2}{3})e$, and the d, s, b quarks have $(-\frac{1}{3})e$ electric charge. Like the electric charge is responsible for electromagnetic interaction, the color charge is responsible for the strong interaction. All the quarks and gluons carry color charges, which allow them to interact strongly.

Because of its non-abelian nature, QCD has many exciting properties, mainly color confinement and asymptotic freedom. According to QCD, no colored singlets can exist freely in nature. Instead, the quarks and gluons are confined within the hadrons. Hadrons are color-neutral particles and come in two types: baryons and mesons. Baryons are fermions that consist of three quarks, and mesons are bosons that consist of one quark and an antiquark. The strength of the strong force increases with increased distance between the particles involved, making it impossible to separate two quarks. If we provide enough energy to separate two quarks, we end up with two sets of quark-antiquark pairs from the excess energy provided. This phenomenon is called color confinement. Moreover, when the quarks are bound inside a hadron, they can move almost freely in that short dimension; this phenomenon is called asymptotic freedom. Due to asymptotic freedom, the coupling between the quarks becomes weak at high energies and very small distances. Thus, we expect a weakly coupled mixture of quarks and gluons at extremely high temperatures and density. When thermalized, this soup of quarks and gluons behaves like a fluid with collective phenomena called quark-gluon plasma.

In order to understand the QGP, one needs to know the QCD Lagrangian,

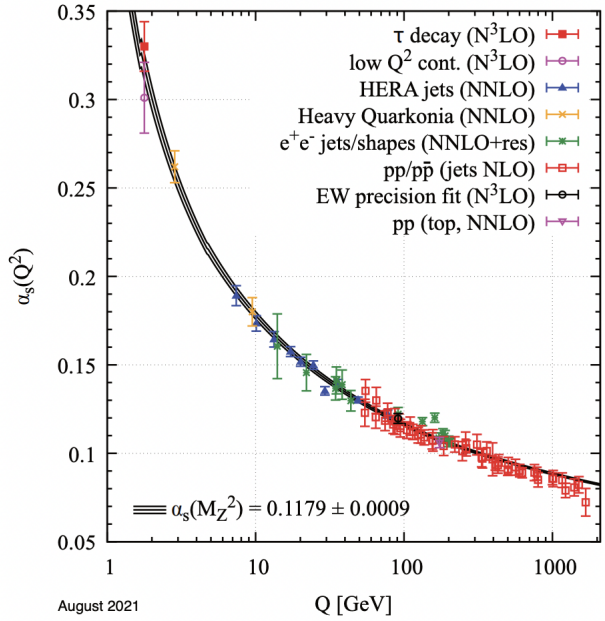

Figure 1.1: Running coupling constant of strong as a function of momentum transfer between partons [1, 2].

which is given by

$$\mathcal{L} = \sum_q \bar{\Psi}_{q,a}(\gamma^\mu \partial_\mu \delta_{ab} - g_s \gamma^\mu t^C_{ab} A^C_\mu - m_q \delta_{ab})\Psi_{q,b} - \frac{1}{4} F_{\mu\nu A} F^{A\mu\nu}. \tag{1.1}$$

The repeated indices are summed over. Here, γ_μ represents the Dirac-γ matrices, $\Psi_{q,b}$ is the quark-field spinor, m_q is the mass of the quark-flavour q. A_μ corresponds to the color field with the index C going from 1 to 8. 'a' is the flavor index for 3 flavors. The term t^C_{ab} is the SU(3) group generator corresponding to eight 3×3 matrices, and g_s is the QCD coupling constant. The field tensor $F^A_{\mu\nu}$ is given as,

$$F^A_{\mu\nu} = \partial_\mu A^A_\nu - \partial_\nu A^A_\mu - g_s f_{ABC} A^B_\mu A^C_\nu \tag{1.2}$$

Here, f_{ABC} is the structure constant of the SU(3) group. The third term in the above expression is the self interaction term in QCD, which allows the gluon-gluon interactions. This interaction term becomes the key difference between QCD and

QED and is responsible for asymptotic freedom and color confinement.

To understand the behavior of the partons, we need to look at the potential between them. The effective QCD potential between two partons is given as,

$$V_{\mathrm{QCD}}(r) = -\frac{4}{3}\frac{\alpha_{\mathrm{s}}}{r} + kr, \tag{1.3}$$

where α_{s} is the strong coupling constant related to g_{s} with the relation $\alpha_{\mathrm{s}} = g_{\mathrm{s}}/4\pi$, k is the color string tension constant and r is the distance between two interacting partons. This potential is the reason behind the color confinement of partons. The strong coupling constant α_{s} is analogous to the electromagnetic fine structure constant α. However, α_{s} is not exactly a constant but changes with momentum transfer between the partons, as can be seen from Fig. 1.1, thus otherwise called the running coupling constant. The running coupling constant, which is a function of four-momentum transfer, is given as,

$$\alpha_{\mathrm{s}}(Q^2) = \frac{12\pi}{(11n - 2n_f)\ ln(Q^2/\Lambda^2_{QCD})}, \tag{1.4}$$

where, n_f is the number of quark flavours and Λ_{QCD} is the non-perturbative QCD scale parameter. Q^2 is the momentum transfer between the partons. α_{s} decreases as a function of momentum transfer, suggesting the asymptotic freedom behavior of QCD. High momentum transfer refers to the area of perturbative QCD theory. As we go towards the lower value of Q^2, α_{s} increases, and the perturbation theory breaks down when approaching the scale of light hadron, i.e., 1 GeV. The large value of α_{s} in the low Q^2 limit indicates the partons' confinement.

Nonetheless, a deconfined partonic medium was believed to have been created in the early stages of the Universe's evolution as the extreme temperature and energy density condition was perfect for its production. We turn towards collider physics to understand and study such an early universe phase. Since the mid-twentieth century, many advancements have been made in collider physics. From linear accelerators to cyclotrons, physicists have probed the quantum scale extensively. After the establishment of QCD theory, the search for QGP has also been

at the forefront of collider physics and research. With a sufficient center of mass energy, two colliding heavy ions can produce a thermalized deconfined medium, much like what was present a few microseconds after the big bang. Thus, by studying the matter created in such heavy-ion collisions, we can, in principle, understand the early universe.

1.1 High energy collisions

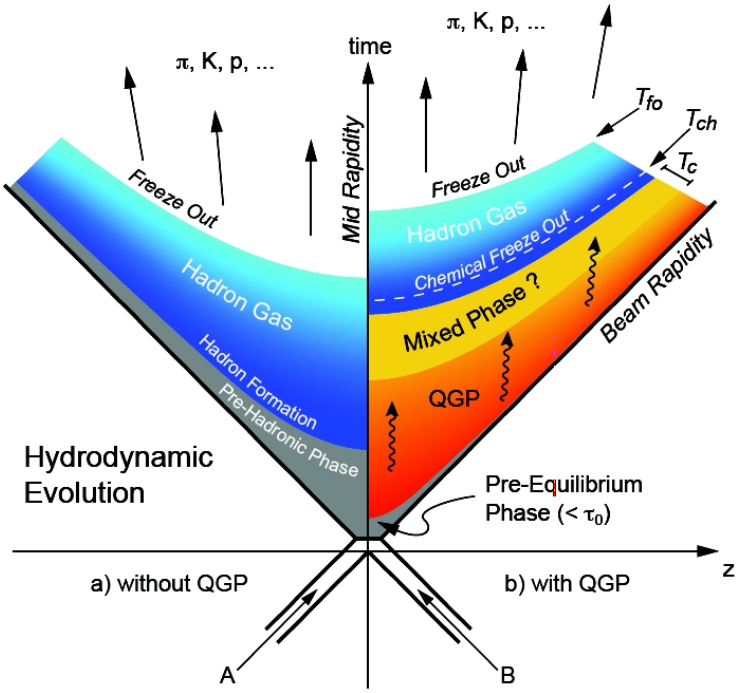

Figure 1.2: Space-time evolution of ultra-relativistic high energy collisions [3].

Fig. 1.2 shows a schematic diagram of the space-time evolution of the ultra-relativistic collisions for both with and without QGP cases. When two heavy ions travelling at ultra-relativistic velocities collide, the produced system goes through several phases of evolution. Due to Lorentz contraction in the direction of their motion, the colliding particles become almost disc-shaped. Then, at $t = 0$ and $z = 0$, the collision happens, and the first phase that is produced is a pre-equilibrium

of partons. The time period of this stage is $t \leq$ one fm/c. All the partons produced in this stage have high transverse momentum. As time evolves and the system thermalizes, the QGP phase occurs. Depending on the collision system and energy, this phase lasts a few fm/c. Then, the mixed phase happens, where some partons combine, forming hadrons, but both hadrons and partons exist together. Then, finally, the hadronization stops, and at a certain temperature, the chemical freeze-out happens, after which the inelastic collisions seize or in other words the particle producing interactions and the particle abundances are frozen. This is called the chemical freeze-out boundary, defined by the chemical freeze-out temperature ($T_{\rm ch}$). This is followed by the hadronic phase, where the particles can still interact elastically. This phase also lasts for a few fm/c depending on collision species and collision energies. In the end, the elastic collisions also stop at the kinetic freeze-out boundary, where the mean free path of the system becomes higher than the system size. This boundary is defined by the kinetic freeze-out temperature ($T_{\rm kin}$). The final state particles then free-stream toward the detectors and get detected. These types of evolution are generally expected in most central heavy-ion collisions.

On the other hand, if no QGP medium is formed during the evolution, the whole process is quite different. In such cases, there is a pre-hadronic phase after the collision, followed by the hadron gas phase. Finally, the kinetic freeze-out happens, and the final state particles travel toward the detectors. This is expected to occur in peripheral heavy-ion collisions and *pp* collisions, where QGP-type medium formation is usually not expected.

1.2 Quark-Gluon Plasma (QGP)

Much like the phase transition of water between the liquid-gas phases, QCD calculations show a phase transition of the hadronic matter into a deconfined, thermalized soup of partons. This new state of matter is created at very high

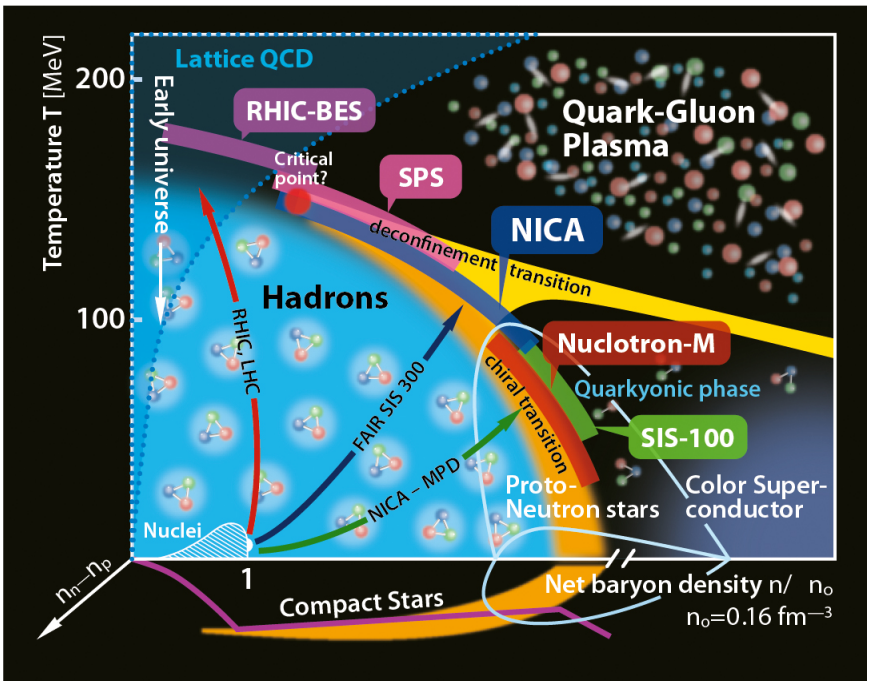

Figure 1.3: Schematic picture of QCD phase diagram [4].

temperatures and/or baryon densities. The QGP temperature at the LHC reaches almost 10^5 times that of the Sun's core. The pressure-temperature $(P-T)$ phase diagram in a basic thermodynamical system gets converted to the baryochemical potential-temperature $(\mu_B - T)$ phase diagram when we study the quark-gluon plasma and deconfinement transition. Mapping the QCD phase diagram is of utmost importance and creates a lot of intrigue in the scientific community. The hadrons are the degrees of freedom at low temperatures and low baryon density. Conversely, partons become the degrees of freedom at very high temperatures and/or baryon densities. The phase transition between hadrons to partons is not trivial. As can be seen from Fig. 1.3, the very high temperature and low $\mu_{\rm B}$ region in the QCD phase diagram is described by the collider experiments at the LHC and RHIC. The phase transition in this region is of a crossover type, as shown by the lattice QCD (lQCD) calculations. As we decrease the collision energy, the baryochemical potential increases, and the temperature decreases. The phase

transition is first-order at very high μ_B and low-temperature regime. This area is described by the fixed target experiment environments such as FAIR and NICA. The high baryon-rich environment can also signify the physics of neutron stars. A critical point of second-order phase transition is expected to exist where both the first-order and the cross-over lines meet. Searching this critical point is crucial as it is still elusive experimentally. Due to the breakdown of lQCD theory at high μ_B region, there is no first principle calculation of this second-order phase transition. However, there are a lot of phenomenological models which try to constrain the location of this critical point and thus, the study of the QCD phase diagram has been a matter of intense research.

1.2.1 Signatures of QGP

QGP is very short-lived, with a lifetime of a few fm/c. Thus, it is impossible to detect QGP directly. However, various signatures of QGP can be studied explicitly, giving important information about this new state of matter. Several signatures have been proposed, such as jet quenching, strangeness enhancement, charmonia suppression, collective flow, etc. Observing these signatures may indicate a possible QGP medium being formed in ultra-relativistic collisions.

- **Jet Quenching**

  The partons produced in the initial stage of an ultra-relativistic heavy-ion collision carry very high momenta, being formed from the perturbative QCD interaction. They traverse through the deconfined medium and interact with other partons. Through radiative and collisional processes, they lose energy before hadronizing. The hadrons form a conical collimated back-to-back structure called a jet. Thus, due to the interaction in the medium, p_{T} of these hadrons get suppressed. This phenomenon is called jet quenching, which was first observed in RHIC and later confirmed in LHC. It is measured by the nuclear modification factor (R_{AA}), which gives the p_{T} dependent

ratio of invariant yields of hadrons in A+A collisions to that of *pp* collisions scaled by the number of binary collisions ($N_{\rm coll}$).

$$R_{\rm AA} = \frac{\sigma_{\rm inel}}{\langle N_{\rm coll}\rangle} \frac{(\frac{d^2N}{dydp_{\rm T}})_{\rm AA}}{(\frac{d^2N}{dydp_{\rm T}})_{\rm pp}}. \tag{1.5}$$

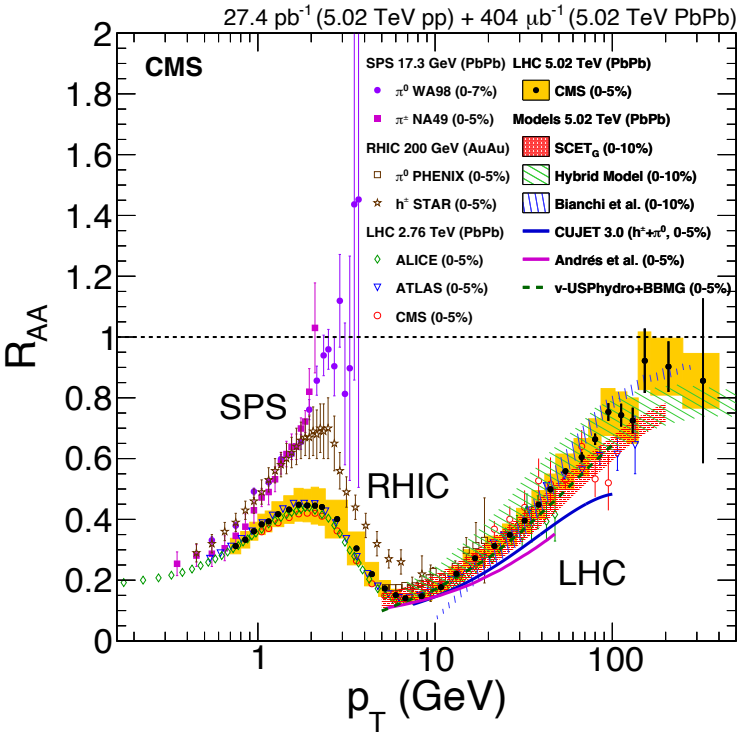

Figure 1.4: Nuclear modification factor, $R_{\rm AA}$, for neutral pions, charged hadrons, and charged particles in central heavy-ion collisions at SPS, RHIC and the LHC [5].

$R_{\rm AA} = 1$ suggests that nuclear collisions are a linear superposition of *pp* collisions, and there is no formation of QGP. When it becomes less than 1 at high-$p_{\rm T}$, it indicates quenching in the QGP medium. From theoretical studies, the parton energy loss can be attributed to a series of jet transport coefficients, such as the jet quenching parameter ($\hat{q}$). It is defined as the transverse momentum squared per unit length of the propagating parton

as well as the energy loss per unit length, $\Delta E = \frac{dE}{dx}$. $\hat{q}$ is also related to the gluon distribution density of the medium. Thus, it characterizes the medium property as probed by an energetic jet. The behavior of the jet quenching parameter can give us a hint about the possible formation of a QGP medium through the path-length-dependent energy loss in the medium.

Fig. 1.4 shows the variation of R_{AA} of various charged particles as a function of p_{T}. The data is collected from Pb–Pb collisions at different collision energies at the SPS, RHIC, and LHC and compared with different theoretical models. It can be observed that there is a clear suppression of the nuclear modification factor at the intermediate and high transverse momentum region for the RHIC and LHC cases, which hints towards the formation of a dense medium.

- **Strangeness enhancement**

  The enhancement of strange and multistrange particle production in the heavy-ion collisions compared to the hadronic collisions is a proposed signature of QGP formation. The colliding particles in the heavy-ion collisions don't contain strange quantum numbers. The dominant mechanism of strange quarks production is $gg \rightarrow s\bar{s}$. In the plasma phase, this reaction will be prevalent, and thus, a large number of particles with strange quarks will be produced. However, considering a system with no QGP (hadronic collision), the strange quarks will be produced only from the gluon-gluon hard scattering. But in a system that goes through the QGP phase, the temperature of QGP is much higher than the strange quark mass; thus, an abundance of strange quark production can happen in the medium. Hence, while comparing in the final state, a system with QGP should show an enhancement of strange particle production (ratio of strange hadrons to pions) compared to a system without QGP. The observation of this enhanced

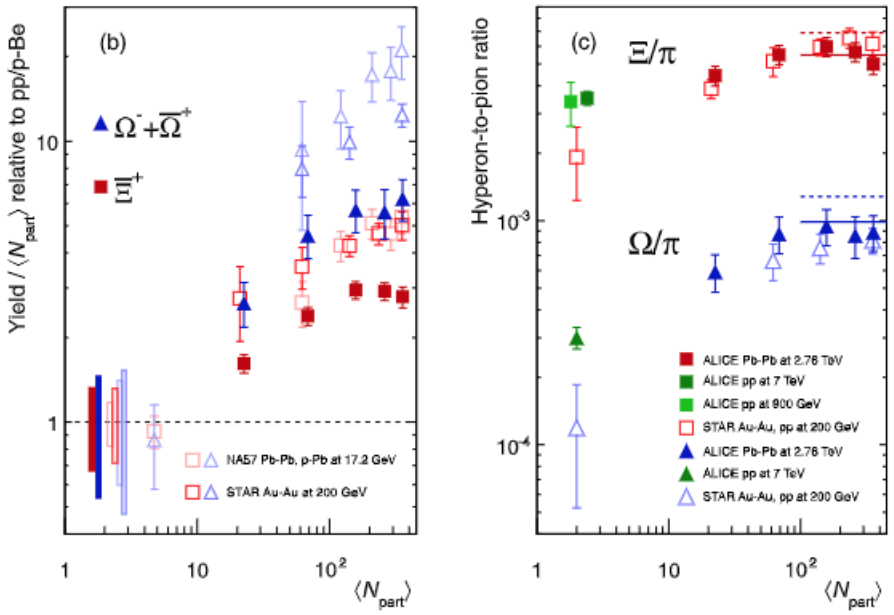

Figure 1.5: Strangeness enhancement of multistrange hadrons as a function of $\langle N_{\text{part}} \rangle$ for various collision systems at the SPS, RHIC and LHC [6].

production of strange and multi-strange particles in the heavy-ion collisions is called strangeness enhancement compared to the hadronic collisions. It has been experimentally observed in RHIC and LHC, where the ratios of Ξ/π and Ω/π are relatively higher in the most central heavy-ion collisions compared to *pp* collisions as shown in Fig. 1.5.

- **Charmonia suppression**

  The charmonia ($c\bar{c}$) are bound states of a charm and anticharm quark. They are produced relatively early in evolution from the hard scattering interactions due to their higher masses. When a thermalized deconfined medium forms, the charmonia dissociates, and the charm and anticharm quarks get separated. Due to the color screening, similar to the Debye screening in the electromagnetic plasma, the charm and anticharm quarks have better probabilities of combining with other lighter quarks. For example, the J/ψ,

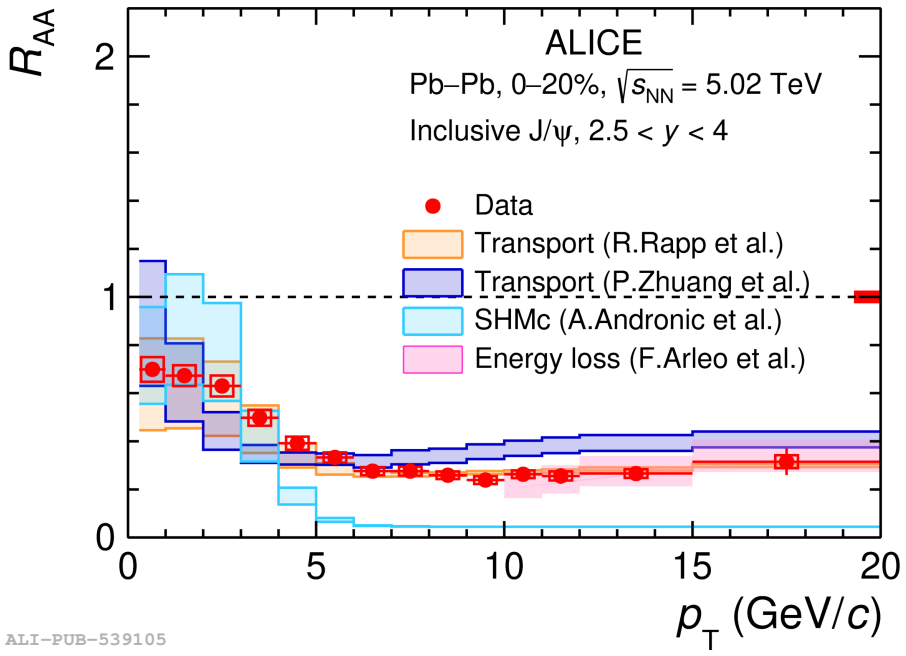

Figure 1.6: Transverse-momentum dependence of the J/ψ $R_{\rm AA}$ at forward rapidity in the 0–20 % centrality class [7].

formed in the evolution's early stage, will dissociate into c and $\bar{c}$ in the deconfined medium. In the presence of other lighter quarks, the c quark may get bound with a $\bar{u}$ quark, forming a D^0 boson in the final state. Thus, in the final state, the number of charmonia gets suppressed. However, in a hadronic collision where no QGP medium is expected to form, there is no color screening, and thus the number of charmonia stays the same. This is called charmonia suppression, one of the cleanest probes of a QGP medium formation. Fig. 1.6 shows the nuclear modification factor of forward rapidity inclusive J/ψ as a function of $p_{\rm T}$ for central Pb–Pb collisions at $\sqrt{s_{\rm NN}}$ = 5.02 TeV showing a clear suppression up to $p_{\rm T} \sim 20$ GeV/c.

- **Electromagnetic probes**

  Photons and dielectrons are called electromagnetic probes, which can be used to understand the QGP medium. The photons and electrons don't

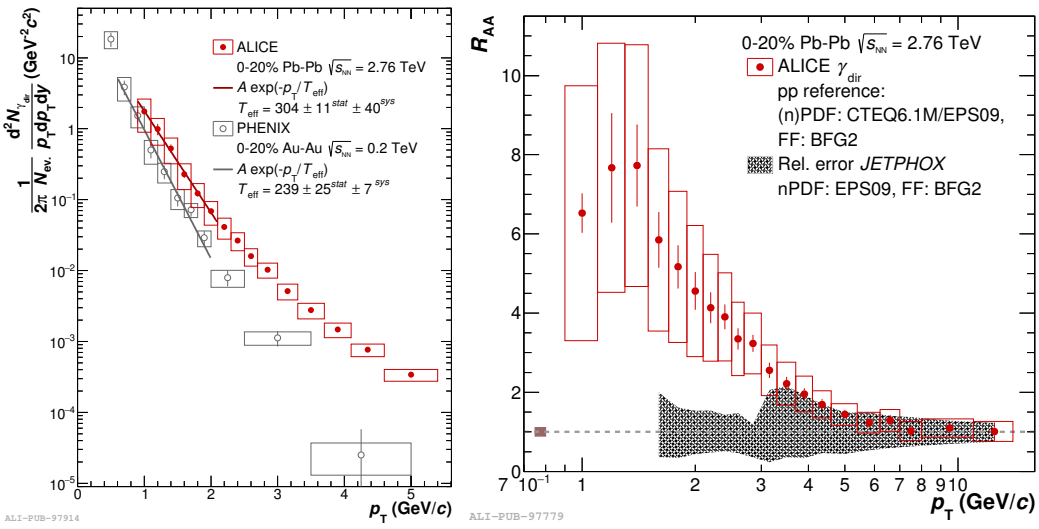

Figure 1.7: Initial photon spectra (left panel) and nuclear modification factor of direct photons for $0-20\%$ centrality Pb–Pb collisions at $\sqrt{s_{\rm NN}} = 2.76$ TeV [8] (right panel).

interact strongly; thus, they travel through the QGP without losing any energy. This makes them an ideal probe to study QGP. The hard scatterings produce these photons and dielectrons early in the system. As a result, the transverse momentum spectra of thermal photons can be used to estimate the initial temperature of the QGP medium.

$R_{\rm AA}$ can also be used to quantify nuclear effects in heavy-ion collisions. From pQCD calculation, $R_{\rm AA}$ for direct photons was calculated, which is taken as *pp* reference. $R_{\rm AA}$ is another way to show the strong enhancement of the direct photon production at low transverse momentum with respect to $N_{\rm coll}$ scaled *pp* collisions. The left panel of Fig. 1.7 shows the $p_{\rm T}$ spectra of the photon, which is fitted with the Boltzmann function to extract the effective temperature. An effective temperature of $T_{eff} \simeq 304$ MeV is obtained at the ALICE, which is substantially higher than the critical temperature for QGP. The right panel of Fig. 1.7 shows the $R_{\rm AA}$ of the

photon as a function of p_{T}. A strong enhancement can be seen at the low transverse momentum region.

- **Heavy quarks as probes of QGP**

  Heavy quarks, such as the charm and bottom quarks, are produced relatively early in the system after the collision through gluon-gluon hard scatterings. The thermalization time of the heavy quarks is also relatively high; for charm quarks, it is estimated to be around 10-15 fm/c; for bottom quarks, it is around 25-30 fm/c [9, 10], which are significantly larger than the QGP lifetime. Thus, they can carry important information about the deconfined system. Due to their higher mass, the heavy quarks suffer Brownian-type motion in the medium; thus, one can, in principle, extract information about the deconfined medium by studying their drag and diffusion coefficients [11]. Moreover, in the hadronic medium, open charmed hadrons such as D^0 meson will diffuse considerably larger than hidden charmed hadrons like J/ψ. This essentially results in a suppressed v_2 of D^0. But, because J/ψ remains largely undiffused in the hadronic phase, the elliptic flow of J/ψ will give unfiltered information about the deconfined phase, making J/ψ a cleaner probe for studying QGP.

1.2.2 Signatures of QGP droplets in *pp* collisions

Previously it was believed that no QGP-like medium is expected to be formed in *pp* collisions due to the production of low energy density. However, recent advances have shown hints of the possible formation of a thermalized medium in high multiplicity *pp* collisions. The first observation of such a hint was through the strangeness enhancement in high multiplicity *pp* collisions [12]. In Fig. 1.8, the ratio of strange particles such as K^0_S, $\Lambda+\bar{\Lambda}$, $\Xi^-+\Xi^+$ and $\Omega^-+\Omega^+$ to $\pi^-+\pi^+$ comes almost the same in high multiplicity

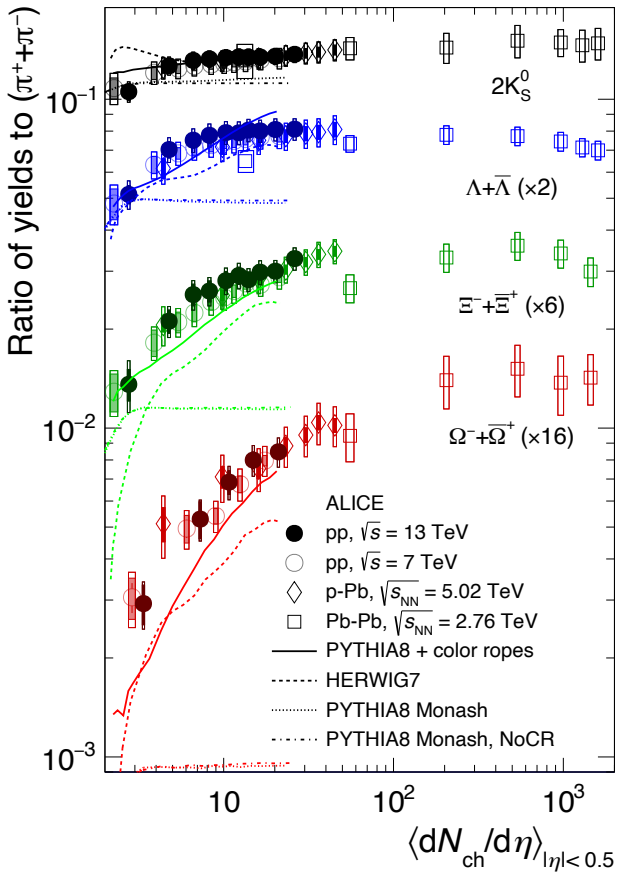

Figure 1.8: Strangeness enhancement as a function of final state charged particle multiplicity for various collision systems measured by ALICE [13].

pp collisions and peripheral heavy-ion collisions. This was a path-breaking observation regarding the possibility of QGP medium formation in small systems. Apart from this, ridge-like structures were also observed in high multiplicity *pp* collisions. In two-particle azimuthal correlations, the ridge, which is a long-range near-side structure, was initially observed in Cu–Cu and Au–Au collisions at RHIC and later at the LHC. The reason for this ridge formation in the heavy-ion systems is because of the collective flow of the strongly interacting matter. The CMS experiment has observed a same-side ($\Delta\phi \sim 0$) ridge in high multiplicity *pp* collisions, which hints

towards the presence of collectivity in small systems [14].

In view of these, it is fascinating to explore the high multiplicity *pp* events and look for more evidence of possible QGP formation.

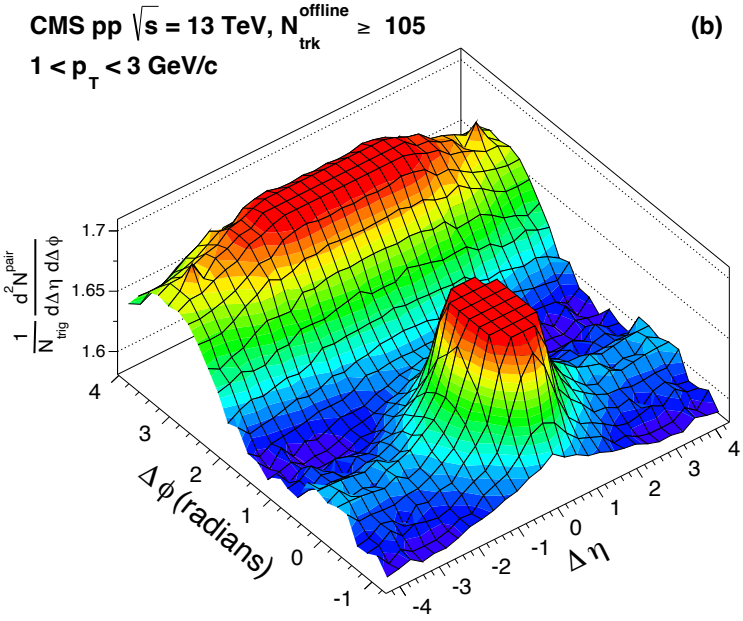

Figure 1.9: Two particle correlation function in high multiplicity *pp* collisions [14].

Many experimental and theoretical studies are going on in this domain. In Ref.[15], J/ψ suppression in *pp* collisions has been studied using a theoretical unified quarkonia suppression model (UMQS). The authors report a finite suppression of J/ψ in high multiplicity *pp* events while explaining the experimental data of relative yield of J/ψ in *pp* collisions at $\sqrt{s}$ = 7 and 13 TeV. Exploring phenomenological avenues requires new insights into jet quenching in *pp* collisions. Thus, it would be interesting to look for a possible QGP medium formation by studying various thermodynamic and transport properties of the matter formed in *pp* collisions to heavy-ion collisions.

1.3 Thermodynamic and transport properties of QCD matter

In addition to various signatures of QGP, substantial important information can be extracted by understanding the thermodynamic and transport properties of the matter formed in an ultra-relativistic collision. To describe any system, the essential observables are pressure (P), energy (E), entropy (S), and number (N). As we are dealing with a relativistic system where extracting the volume information is not very straightforward, it becomes convenient to consider the densities of the abovementioned observables, such as energy density (ϵ), entropy density (s) and number density (n). The basic Euler's thermodynamic relation is given by,

$$\epsilon + P = Ts + \mu n, \tag{1.6}$$

where, the total chemical potential, $\mu = B\mu_{\rm B} + S\mu_{\rm S} + Q\mu_{\rm Q}$, with B, S and Q denoting the baryon number, strangeness and charge and $\mu_{\rm B}$, $\mu_{\rm S}$ and $\mu_{\rm Q}$ are their corresponding chemical potentials.

With the help of these fundamental quantities, along with the temperature and chemical potential information, we can estimate various important thermodynamic variables. Some of the essential thermodynamic observables are the mean free path (λ), speed of sound ($c_{\rm s}^2$), specific heat ($c_{\rm v}$), and isothermal compressibility ($\kappa_{\rm T}$), etc. These thermodynamic quantities are essential to understand the system formed in an ultra-relativistic collision. For example, the initial energy density can hint at the possible formation of a QGP-like medium. From the lattice QCD estimations, the critical energy density for forming a deconfined medium is $\epsilon_c = 1$ GeV/fm^3. The initial Bjorken energy density can help us know whether the system under consideration can produce QGP. Moreover, the scaled energy density (ϵ/T^4) gives us information about the degree of freedom in the

system, approaching the ideal Stefan-Boltzmann limit at very high temperatures.

The mean free path of the system is defined as the average distance between two successive collisions among the constituent particles. It is the inverse of the number density of the system and the scattering cross-section between the particles. It can tell us how dense a system is. On the other hand, the speed of sound tells us about the interaction in the system under scrutiny. It can quantify the deviation of a system from an ideal massless gas. The specific heat is related to the entropy in the system and, thus, is an excellent measure of phase transition. In addition, isothermal compressibility tells us about the deviation of a fluid from a perfect fluid behavior.

Moreover, the study of the transport properties of the matter formed in ultra-relativistic collisions is extremely beneficial. The shear viscosity (η) and bulk viscosity (ζ) along with the electrical conductivity ($\sigma_{\rm el}$) and thermal conductivity ($\kappa_{\rm th}$) are dissipative properties which govern the dynamics of the medium evolution. These dissipative properties are related to the diffusion of matter or energy. Similarly, the diffusion of the heavy quark, such as charm, is also a vital transport property to study, as charm quarks are good probes of a QGP-like medium. In addition, the jet transport coefficient can also be estimated, which can give us information about a deconfined dense medium formation. In the present thesis we have considered some of the important thermodynamic and transport properties of the medium using theoretical models.

1.4 Polarization measurement as a test for QCD

Polarization is the alignment of the spin of a particle in a given direction. Mostly, quarkonia polarization studies can help us to understand the particle production mechanism better. In literature, there are numerous quarkonia production mechanisms that give different results for quarkonia polarization. The non-relativistic QCD (NRQCD) model explains the quarkonia production very well; however, it

fails to explain the experimental quarkonia polarization data. The color-octet NRQCD model gives a transverse polarization at high transverse momentum, whereas the color-singlet NRQCD predicts a longitudinal polarization for quarkonia at high p_{T}. The incompatibility between various theoretical models and the existing experimental data begs the question of the inherent mechanism of quarkonia production and polarization. From the experimental point of view, J/ψ polarization has been studied in ALICE collaboration for pp collisions at $\sqrt{s} = 7$ and 8 TeV. J/ψ polarization has also been studied for pp collisions at $\sqrt{s} = 200$ GeV in the STAR experiment in both dielectron and dimuon channels [16]. The CDF collaboration has measured both J/ψ and $\psi(2\mathrm{S})$ polarization in $\mathrm{p\bar{p}}$ collisions at $\sqrt{s} = 1.8$ TeV [17]. Moreover, the CMS and LHCb collaborations have measured the J/ψ and $\psi(2\mathrm{S})$ polarization in pp collisions at 7 TeV from the dielctron and dimuon decay channel by taking different kinematic ranges [18–20]. All the results are compatible with zero within uncertainties, contrasting with the theoretical predictions. Thus, it is crucial to have new studies with higher statistics and at higher center of mass energies, which can give us conclusive experimental results.

Fig. 1.10 shows the polarization parameters λ_ϑ and λ_φ obtained by the ALICE experiment as a function of p_{T} in the Collins-Soper frame. Theoretical calculations from the color-singlet and color-octet NRQCD models are also shown for comparison. The ALICE results are compatible with zero within uncertainties, without any compatibility with the theoretical models, which warrants for further studies with higher center of mass energies and higher statistics.

Aside from helping us to constrain the quarkonia production mechanisms, quarkonia polarization in pp collisions can serve as a baseline for heavy-ion studies. In heavy-ion, the polarization of quarkonia can be affected by the external magnetic field produced by the spectator protons. In addition, the vorticity created initially can also affect the polarization of quarkonia significantly. In a system where a thermal medium is produced, polarization can happen through

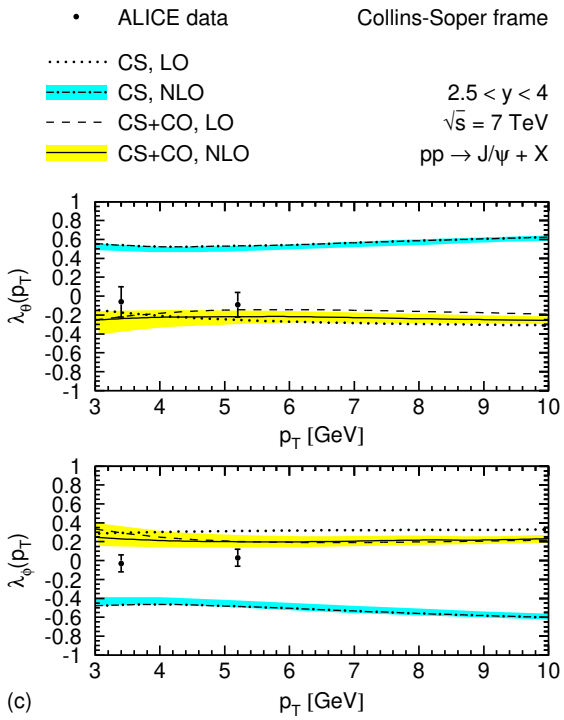

Figure 1.10: J/ψ polarization as a function of transverse momentum [21].

the spin-vorticity coupling. Assuming minimum-bias *pp* collision does not have a QGP-like medium, one can use the minimum-bias measurement as a benchmark for polarization studies in high multiplicity *pp* or heavy-ion collisions.

1.5 Thesis motivation

The primary motivation of this thesis is to understand the medium formed in ultra-relativistic hadronic collisions. It has been explored in two different parts: phenomenological and experimental.

1.5.1 Phenomenological motivation

In the first part, we have estimated different thermodynamic and transport properties of the matter formed in high-energy *pp* collisions and compared that with the heavy-ion collisions. One can use any well-established theoretical model to study the thermodynamic and transport properties of the hot and dense QCD matter. The lattice QCD (lQCD) is one of the most successful theories derived from the first principle calculations. It works at high temperatures and vanishing baryochemical potential regions. However, at high $\mu_{\rm B}$, lQCD breaks down because of the fermion sign problem [22]. A great alternative to lQCD in low temperatures (up to $T \leq 150$ MeV) is the hadron resonance gas (HRG) model [23]. It can explain the hadron yields very well and matches with the lQCD results. It can also work in a very high baryochemical potential regime. However, this theory breaks down after $T = 150$ MeV as the hadrons melt at this temperature. Thus, the results from the HRG model deviate from those of the lQCD. Many other established models exist, such as the Nambu-Jona Laisino (NJL) model [24] and its extension, the Polyakov loop NJL (PNJL) model [25]. These are alternatives to the QCD theory and can explain the lQCD data very well, albeit they have their own assumptions. Several other models, such as the Parton-Hadron Cascade Dynamics (PHSD) [26], the Dynamical Quasiparticle model (DQPM) [27], and the Holographic QCD theory [28], etc. have been used to estimate the thermodynamic and transport properties of the QCD matter.

In this thesis, we have used a QCD-inspired model called the Color String Percolation model (CSPM) [29] to estimate various thermodynamic and transport properties of the hot and dense QCD medium. CSPM assumes colored strings to be stretched between partons of the colliding nuclei. These colored strings have very high color fields, quantified by their string tension. These strings break via Schwinger's string-breaking mechanism and form quark-antiquark pairs. The quarks finally hadronize and form the hadrons, which are detected in the final

state of the collisions. The colored strings formed in the initial stage overlap in the transverse space, forming clusters of colored discs. A percolation phase transition happens when these clusters occupy 2/3rd of the overlapping area. The idea is to have an analogy between this percolation phase transition and the QCD phase transition and study the systems formed in high-energy collisions. Such studies can help us to have a new perspective on estimating such important observables while constraining their theoretical values. We have also estimated the hadronic phase lifetime of various collision systems and collision species which helps us to understand the hadronic phase of the high-energy collisions in a better way.

1.5.2 Experimental motivation

A brief description of the ALICE experiment is given in the second part of the thesis. Then we discuss the processes behind quarkonia polarization, some literature review and finally, we give the preliminary results of ψ(2S) polarization in pp collisions at $\sqrt{s}$ = 13 TeV from the ALICE collaboration. For this study, we have used the dimuon decay channel with the help of the muon spectrometer at the forward rapidity ($4.0 < |y| < 2.5$) in the ALICE detector. This study helps us to constrain the theoretical models and strengthen our understanding of quarkonia production, which is extremely important. In addition, this can also give a benchmark measurement for quarkonia polarization in heavy-ion collisions where the medium effect would modify the final polarization.

This thesis is organized as follows. In chapter 2, we discuss various thermodynamic and transport properties of the matter produced in ultra-relativistic collisions by using the QCD-inspired color string percolation model. In chapter 3, we study the hadronic phase lifetime of ultra-relativistic collisions by using a toy model. In addition, we locate the QGP phase boundary with the help of the effective temperature of ϕ meson. In chapter 4, we discuss the ψ(2S) polarization measurement in pp collisions at $\sqrt{s}$ = 13 TeV with the ALICE experiment. We

briefly discuss the ALICE detector, specifically the forward muon spectrometer, which is used in this study. The theoretical foundation of charmonia polarization is given, and then we explain the obtained polarization results. Finally, in chapter 5, we summarize the work in this thesis.

Chapter 2

Estimation of thermodynamic and transport properties by using Color String Percolation Model

2.1 Introduction

To understand the matter formed in ultra-relativistic hadronic and heavy-ion collisions, it is essential to study its thermodynamic and transport properties. Lattice QCD (lQCD) theory, which comes from the first principle calculation, is a robust and reliable method to study various thermodynamic properties of such matter. One can estimate the scaled pressure (P/T^4), scaled energy density (ϵ/T^4), scaled entropy density (s/T^3) at vanishing baryochemical potential using the lQCD theory. In addition, the trace anomaly (Δ/T^4), the squared speed of sound (c_s^2), scaled specific heat (c_v/T^3) and various conserved charge fluctuations have also been estimated using the lQCD [23, 30]. However, the applicability of lQCD breaks down at high baryochemical potential regions due to the negative fermion sign problem [22]. Although there have been recent attempts to bypass this issue, the problem still persists largely [31–33]. Many alternative theories have emerged to explain different aspects of ultra-relativistic collisions and the QCD phase diagram. There have been various other theoretical and phenomeno-

logical models that work better in high μ_{B} regime while explaining the lQCD data at vanishing baryochemical potential. The hadron resonance gas (HRG) model is a widely used alternative that works at low temperatures and effectively explains the lQCD data up to $T \leq 150$ MeV [23, 34]. However, HRG is a simplistic model that does not consider the interactions between the hadrons. It also fails to explain the high-temperature regime due to the melting of hadrons beyond the critical temperature, T_{c}. There have been several modifications to the HRG model by introducing interactions through excluded volume effect (EVHRG) and mean-field potential (MFHRG), which help the model to better explain lQCD data up to a slightly higher temperature ($T \leq 170$ MeV). Other models are alternatives to the QCD theory, such as the Nambu-Jona-Laisino (NJL) model [24]. NJL and its various modifications, such as the Polyakov-loop NJL (PNJL) [25] and Entangled Polyakov-loop NJL (EPNJL) [35], can explain the thermodynamics of the hot and dense matter formed in the ultra-relativistic collisions with a good agreement with the lQCD data. The dynamic quasi-particle model (DQPM) [27] is also quite effective in explaining the lQCD data even at high μ_B region. In this thesis, we focus on the application of the color string percolation model (CSPM) [29], which is a QCD-inspired model that works at zero-baryochemical potential and explains the lQCD data very well. In addition, CSPM allows one to extract useful information from the p_{T}–spectra of the collision systems. Thus, in principle, one can study various thermodynamic and transport properties as a function of the center of mass energy or charged particle multiplicity, which is not usually the case when considering other established models. This makes CSPM instrumental for studying the hot and dense matter formed in ultra-relativistic collisions, taking experimental data as input.

Observables such as pressure (P), energy density (ϵ), entropy density (s), and temperature (T) are the basic properties of any thermodynamic system. In addition, the mean free path (λ), speed of sound (c_{s}), isothermal compressibility (κ_{T}), and bulk modulus (B), each provides us unique understandings which can help us

to characterize the system in a better way. Moreover, transport properties such as shear viscosity to entropy density ratio (η/s) and bulk viscosity to entropy density ratio (ζ/s) show minima at the critical temperature, after which a deconfined medium is expected to form, while giving us information about the fluidity of the system. Quantities such as entropy density, squared speed of sound and specific heat are very important to characterize the QCD phase transition. At low chemical potential, they show a crossover phase transition, whereas at very high μ_B, they show discontinuity which is the characteristics of a first order phase transition. There exists a QCD critical point at the point where the cross-over and first-order phase transitions meet, which is defined by a second order phase transition. In addition, it is also observed that the isothermal compressibility estimation from NJL model shows discontinuity, which is the signature of a first order chiral phase transition [36]. In this chapter, we use the well-established CSPM to estimate the abovementioned quantities. In particular, we focus on the charged particle multiplicity dependence of the thermodynamic and transport properties, spanning from the small systems such as that formed in *pp* collisions at $\sqrt{s}$ = 7 TeV and 13 TeV up to large systems created in Pb–Pb collisions at $\sqrt{s_{\rm NN}}$ = 5.02 TeV.

2.1.1 Temperature

In this thesis, we deal with various temperatures at distinct phases of the hot QCD matter evolution. When two incoming beams collide, at the onset of equilibrium, the temperature can be denoted as the initial temperature ($T_{initial}$). In heavy-ion experiments, this temperature is obtained by fitting the direct photon transverse momentum spectra, whose inverse slope is given as the temperature. This is termed as $T_{initial}$ because the direct photons are produced at the initial hard scatterings, and they remain unaffected in the QCD medium and the subsequent evolution. Thus, they give us unfiltered information about the initial

condition. However, in this thesis, when we talk about initial temperature in the context of CSPM, we mean the temperature at which the quark-antiquark pairs are produced from the color field in the medium. There is a discrepancy between the initial temperature coming from direct photon spectra and that from CSPM, which is due to the model. However, when we study thermodynamic and transport parameters as functions of temperature, we use the symbol (T) for simplicity, and we also compare it with other existing model estimations. After the QGP medium is formed, the hadrons are produced through inelastic collisions and at the chemical freeze-out temperature (T_{ch}), the hadron production stops fixing the particle yield. Further, the system expands, and at a later time, the elastic collisions between the particles stop at the kinetic freeze-out boundary, defined by the kinetic freeze-out or thermal temperature (T_{th}). Earlier, the general consensus was that all the particles freeze-out at the same temperature. But, recent studies regarding differential freeze-out scenarios predict that due to the difference in masses of the charged-particles, they freeze out at different temperatures. Thus, each particle has its own kinetic freeze-out temperature (T_{th}), which is estimated by fitting the transverse momentum spectra with a Boltzmann-type function. We can also define their effective temperature (T_{eff}), which is estimated by taking the information of the particle's average velocity and kinetic freeze-out temperature. Moreover, the temperature at which the hadrons melt to produce partons is called the critical temperature (T_c), which is around 155 MeV, estimated from the lQCD. In this thesis, we have followed the given definitions for consistency.

2.2 Color String Percolation in strongly interacting matter

The color string percolation model is a theoretical framework used to describe the initial stage of the formation of a deconfined medium in high-energy hadronic

and heavy-ion collisions. This model is based on the idea that colliding particles produce a large number of color strings, which are essentially strings of gluons connecting pairs of quarks in the colliding nuclei. These strings have some finite area in the transverse space. As the collision energy or the number of participants increases, the number of strings also grows, thus overlapping in the transverse space and forming clusters of colored strings. After a certain percolation density (ξ_c), a macroscopic cluster appears when 2/3rd of the transverse space is filled with strings, marking the percolation phase transition [37]. The main idea is to have a parallelism between the percolation phase transition and the QCD phase transition and study the behaviour of the matter produced using the CSPM. The color string percolation model has been used to study a wide range of phenomena in heavy-ion collisions, including the distribution of particle production [38], flow in the plasma [29], and the behavior of various thermodynamic quantities such as temperature and pressure. It has also been used to make predictions about the properties of the quark-gluon plasma, such as its viscosity and equation of state.

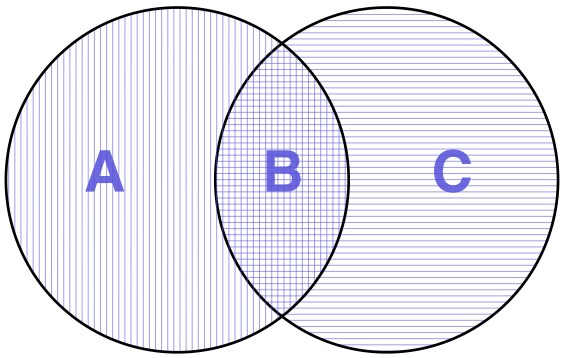

Figure 2.1: A schematic diagram of the overlapping of two colliding nuclei [39].

Let us now understand the formulation of CSPM. Assume that there are two color strings A and C, each with a transverse area of S_1. Their non-overlapping

area is $S_A(\equiv S_C)$, and they partially overlap in the area S_B. The average transverse momentum squared ($\langle p_{\rm T}^2\rangle$) and the string multiplicity (μ_n) are linked to the string's field strength and, in turn, to the generating color of the string. With the assumption of independent emission from the three regions A, B and C in Fig. 2.1, we get [40],

$$\mu_n/\mu_1 = 2(S_A/S_1) + \sqrt{2}\,(S_B/S_1), \tag{2.1}$$

where μ_1 is a multiplicity for a single string. To obtain $\langle p_{\rm T}^2\rangle$, the total transverse momentum squared of all observed particles is divided by the total multiplicity. Hence, for a cluster of two strings we get [40],

$$\begin{aligned}\frac{\langle p_{\rm T}^2\rangle}{\langle p_{\rm T}^2\rangle_1} &= \frac{2(S_A/S_1) + \sqrt{2}\sqrt{2}\,(S_B/S_1)}{2(S_A/S_1) + \sqrt{2}\,(S_B/S_1)} \\ &= \frac{2}{2(S_A/S_1) + \sqrt{2}(S_B/S_1)}.\end{aligned} \tag{2.2}$$

Here, $\langle p_{\rm T}^2\rangle_1$ is the average transverse momentum squared for a single string.

After generalizing this to N_s number of overlapping strings, the total multiplicity can be written as [40],

$$\mu_n/\mu_1 = \sum_i \sqrt{n_i}\,(S^{(i)}/S_1), \tag{2.3}$$

where, the sum is over all individual overlaps i of n_i strings with areas $S^{(i)}$. Similarly, for the $\langle p_{\rm T}^2\rangle$ we can write,

$$\frac{\langle p_{\rm T}^2\rangle}{\langle p_{\rm T}^2\rangle_1} = \frac{\sum_i n_i\,(S^{(i)}/S_1)}{\sum_i \sqrt{n_i}\,(S^{(i)}/S_1)} = \frac{N_s}{\sum_i \sqrt{n_i}\,(S^{(i)}/S_1)}. \tag{2.4}$$

In order to calculate the sums over i, we identify all individual overlaps of the strings with their areas. We combine all the terms with $n_i = n$ overlapping strings into a single term. This sums all such overlaps into a total area of n overlapping strings $S_{\rm N}$. Now we have,

$$\mu_n/\mu_1 = \sum_{n=1}^{N_s} \sqrt{n}\,(S_{\rm N}/S_1) \tag{2.5}$$

and,

$$\langle p_{\rm T}^2\rangle/\langle p_{\rm T}^2\rangle_1 = \frac{N_s}{\sum_{n=1}^{N_s}\sqrt{n}\,(S_{\rm N}/S_1)}. \tag{2.6}$$

Let us assume the projections of the strings onto the transverse space are distributed uniformly in the interaction area $S_{\rm N}$ with a density ρ. Now, we introduce a dimensionless parameter which is known as percolation density [40],

$$\xi = \rho S_1 = \frac{N_s S_1}{S_{\rm N}}. \tag{2.7}$$

For our work, the values of $S_{\rm N}$ for Pb–Pb, Xe–Xe and p–Pb collisions are taken from Ref. [41], and for the pp collisions, the radius is calculated from IP-Glasma model and then is used to estimate the interaction area [42].

In the thermodynamic limit, the number of strings $N_s \to \infty$ while ξ is fixed. In this case, the distribution of the overlaps of n strings is Poissonian, having a mean value ξ,

$$p_n = \frac{\xi^n}{n!}e^{-\xi}. \tag{2.8}$$

From Eq. 2.5, we see that the multiplicity is damped as a result of overlapping by a factor

$$F(\xi) = \frac{\mu_n}{N_s\mu_1} = \frac{\langle\sqrt{n}\rangle}{\xi}, \tag{2.9}$$

where the average is taken over the Poissonian distribution.

From Eq. 2.8, the fraction of the total area occupied by the strings is given by

$$\sum_{n=1} p_n = 1 - e^{-\xi}. \tag{2.10}$$

After dividing by ξ, the above equation gives the compression factor. According to the CSPM picture, the multiplicity is damped by the square root of the compression factor. Thus, the damping factor or the color suppression factor is given by [40],

$$F(\xi) = \sqrt{\frac{1-e^{-\xi}}{\xi}}. \tag{2.11}$$

We can now evaluate ξ by the following process. We fit the experimental data of pp collisions at $\sqrt{s} = 200$ GeV with the following function [43],

$$\frac{d^2N_{\rm ch}}{dp_{\rm T}^2} = \frac{a}{(p_0 + p_{\rm T})^{\alpha}}, \tag{2.12}$$

where a is the normalization factor. p_0 and α are the fitting parameters, which are given as $p_0 = 1.982$ GeV/c and $\alpha = 12.877$. This collision system and energy choice is due to the fact that one can expect no medium formation in low energy pp collisions. To evaluate the interaction of strings in high energy pp, p-A and A-A collisions, we update the parameter p_0 as,

$$p_0 \rightarrow p_0 \left(\frac{\langle \frac{N_s S_1}{S_N} \rangle_{pp,pA,AA}}{\langle \frac{N_s S_1}{S_N} \rangle_{pp,\sqrt{s}=200GeV}} \right)^{1/4}. \tag{2.13}$$

In the thermodynamic limit, where $N_{\rm s}$ and $S_{\rm N} \rightarrow \infty$, keeping ξ fixed we get,

$$\left\langle \frac{N_s S_1}{S_N} \right\rangle = \frac{1}{F^2(\xi)}. \tag{2.14}$$

Using Eq.(2), for pp, p–Pb, Xe–Xe and Pb–Pb collision systems at LHC energies, we obtain,

$$\frac{d^2N_{ch}}{dp_T^2} = \frac{a}{(p_0 \sqrt{F(\xi)_{pp,\sqrt{s}=200\ \rm GeV}/F(\xi)_{pp,pA,AA}} + p_{\rm T})^{\alpha}}. \tag{2.15}$$

We fit the above function to the soft part of the experimental charged-particle $p_{\rm T}$ spectra from 0.12 to 1 GeV/c. Here $F(\xi)$ is a fitting parameter. Due to low string overlap probability in low energy pp collisions, we assume $\langle \frac{N_s S_1}{S_N} \rangle \sim 1$. After getting $F(\xi)$, we can get the values of ξ with a simple back-calculation technique by using Eq. 2.11.

In ultra-relativistic heavy-ion collisions thermalization can occur through the Hawking-Unruh effect [44, 45]. Here, fast thermalization happens with the existence of an event horizon, which is caused by the rapid deceleration of the colliding nuclei [46]. In the CSPM framework, the strong color field inside the large cluster decelerates the $q\bar{q}$ pair, which can be perceived as a thermal temperature because of the Hawking-Unruh effect. This suggests that the radiation temperature can

be determined by the transverse extension of the color flux tube in terms of the string tension.

The Schwinger distribution for massless particles can be expressed in terms of p_{T}^2 as [29, 47]:

$$dn/dp_{\mathrm{T}}^2 \sim \exp(-\pi p_{\mathrm{T}}^2/x^2) \tag{2.16}$$

where $\langle x^2 \rangle$ is the average value of string tension. As the chromoelectric field is not constant, the tension of the macroscopic cluster fluctuates around its mean value. Due to these fluctuations, we get a Gaussian distribution of the string tension given as,

$$\frac{dn}{dp_{\mathrm{T}}^2} \sim \sqrt{\frac{2}{\langle x^2 \rangle}} \int_0^\infty dx \exp\left(-\frac{x^2}{2\langle x^2 \rangle}\right) \exp\left(-\pi \frac{p_{\mathrm{T}}^2}{x^2}\right) \tag{2.17}$$

which in turn gives rise to a thermal distribution,

$$\frac{dn}{dp_{\mathrm{T}}^2} \sim \exp\left(-p_{\mathrm{T}}^2 \sqrt{\frac{2\pi}{\langle x^2 \rangle}}\right). \tag{2.18}$$

From Eq. 2.17 and 2.18, the initial temperature in terms of $F(\xi)$ can be expressed as [48],

$$T(\xi) = \sqrt{\frac{\langle p_{\mathrm{T}}^2 \rangle_1}{2F(\xi)}}, \tag{2.19}$$

where, $\langle x^2 \rangle = \pi \langle p_{\mathrm{T}1}^2 \rangle / F(\xi)$. By using $T_c = 167.7 \pm 2.8$ MeV [49] which is estimated from the statistical hadronization model and $\xi_c \sim 1.2$ which is the critical percolation density, we get $\sqrt{\langle p_T^2 \rangle_1} = 207.2 \pm 3.3$ MeV. We can estimate the initial temperature for different $F(\xi)$ values by using the above values in Eq. 2.19.

Fig. 2.2 shows the color suppression factor as a function of charged particle multiplicity scaled with the nuclear overlap area. For low multiplicity pp collisions, $F(\xi)$ has a higher value, and it goes on decreasing with an increase in charged particle multiplicity. This suggests that for a system to have a higher number of final state charged particle multiplicity, the color suppression factor

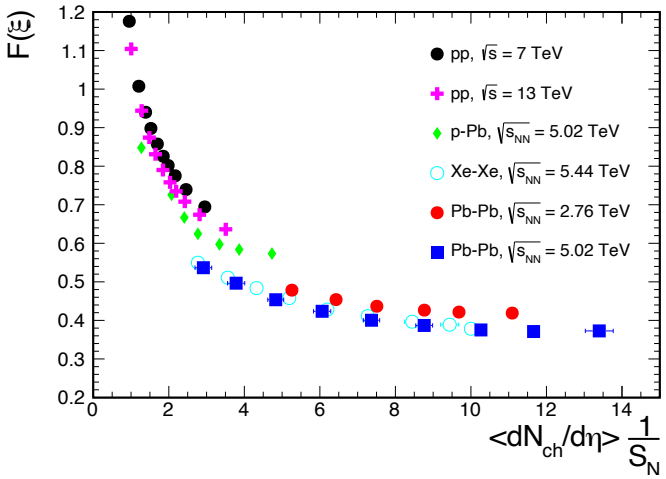

Figure 2.2: Color suppression factor as a function of scaled charged particle multiplicity density for pp collisions at $\sqrt{s}$ = 7 and 13 TeV, p–Pb collisions at $\sqrt{s_{\rm NN}}$ = 5.02 TeV, Xe–Xe collisions at $\sqrt{s_{\rm NN}}$ = 5.44 TeV, Pb–Pb collisions at $\sqrt{s_{\rm NN}}$ = 2.76 and 5.02 TeV [50] estimated from the CSPM.

should be low. Fig. 2.3 shows the percolation density parameter as a function of charged particle multiplicity. An increasing trend can be seen with the increase in multiplicity. One can observe that after a certain $\langle dN_{\rm ch}/d\eta\rangle$, the percolation density becomes higher than the critical value, suggesting a percolation phase transition. In Fig. 2.4, the initial percolation temperature is plotted as a function of charged particle multiplicity. The temperature increases with an increase in charged particle multiplicity. After a threshold of $\langle dN_{\rm ch}/d\eta\rangle \simeq 10-20$, the temperature exceeds that of the hadronization temperature, suggesting a possible deconfinement. In this view, one can clearly see that high multiplicity pp collisions show the possibility of deconfinement, which is very intriguing.

To estimate various thermodynamical observables, we have used the obtained temperature and ξ values, whereas the $\langle dN_{\rm ch}/d\eta\rangle$ values are taken from Refs. [51, 53–57, 98]. In the following subsections, we briefly describe the formulation of different thermodynamic observables in CSPM approach.

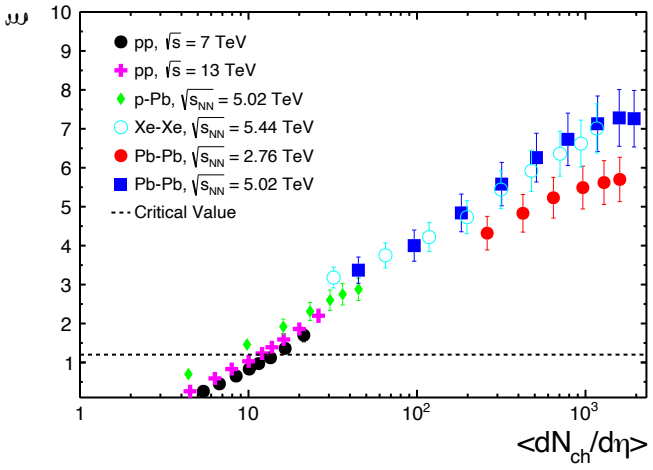

Figure 2.3: Percolation parameter (ξ) as a function of charged particle multiplicity for pp collisions at $\sqrt{s}$ = 7 and 13 TeV, p–Pb collisions at $\sqrt{s_{\rm NN}}$ = 5.02 TeV, Xe–Xe collisions at $\sqrt{s_{\rm NN}}$ = 5.44 TeV and Pb–Pb collisions at $\sqrt{s_{\rm NN}}$ = 2.76 and 5.02 TeV [39] estimated from the CSPM. The dotted line represents the critical string density, after which a macroscopic cluster appears.

2.3 Thermodynamic and transport properties

2.3.1 Initial Energy Density

A tremendous amount of energy is deposited at the collision point when two ultra-relativistic particles/ions collide. This can be quantified by the initial energy density (ϵ), which is the energy stored in the volume created at the initial state of the collisions. From the estimations of lattice QCD calculation, it is known that if the initial energy density exceeds 1 GeV/fm^3, a deconfined medium can be formed. Thus, a better understanding of how the matter behaves after a collision can be obtained if we have information about the initial energy density. This also drives the time evolution of the system through pressure gradient and hence is related to the equation of state of the system.

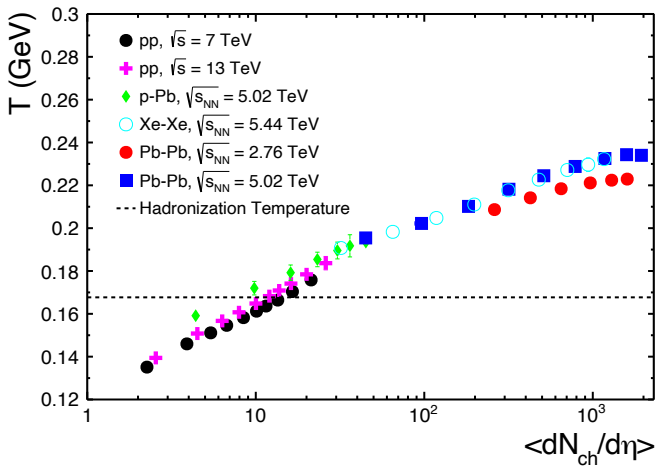

Figure 2.4: Initial temperature as a function of charged particle multiplicity for pp collisions at $\sqrt{s}$ = 7 and 13 TeV, p–Pb collisions at $\sqrt{s_{\rm NN}}$ = 5.02 TeV, Xe–Xe collisions at $\sqrt{s_{\rm NN}}$ = 5.44 TeV and Pb–Pb collisions at $\sqrt{s_{\rm NN}}$ = 2.76 and 5.02 TeV [39] estimated from the CSPM. The dotted line represents the reported hadronization temperature [49].

The CSPM framework uses the Bjorken formula to estimate the initial energy density [29, 58],

$$\epsilon = \frac{3}{2}\frac{dN_{\rm ch}/dy\langle m_{\rm T}\rangle}{S_{\rm N}\tau_{\rm pro}}, \tag{2.20}$$

where $\langle m_{\rm T}\rangle$ is the mean transverse mass of the partons and $\tau_{\rm pro}$ is the parton production time which is assumed to be $\sim$ 1 fm/c and $\tau_{\rm pro} = \frac{2.405\hbar}{\langle m_{\rm T}\rangle}$. Hence, $\langle m_{\rm T}\rangle$ is fixed from the string level, and its variation as a function of charged particle multiplicity is not taken into account. Here, we have assumed $dN_{\rm ch}/dy$ to be $dN_{\rm ch}/d\eta$ by assuming a Bjorken rapidity and pseudorapidity correlation. After solving, the final expression looks like,

$$\epsilon = 0.71153\frac{dN_{\rm ch}/d\eta}{S_{\rm N}}. \tag{2.21}$$

Using the above equation, we have estimated the initial energy density for various systems at different collision energies.

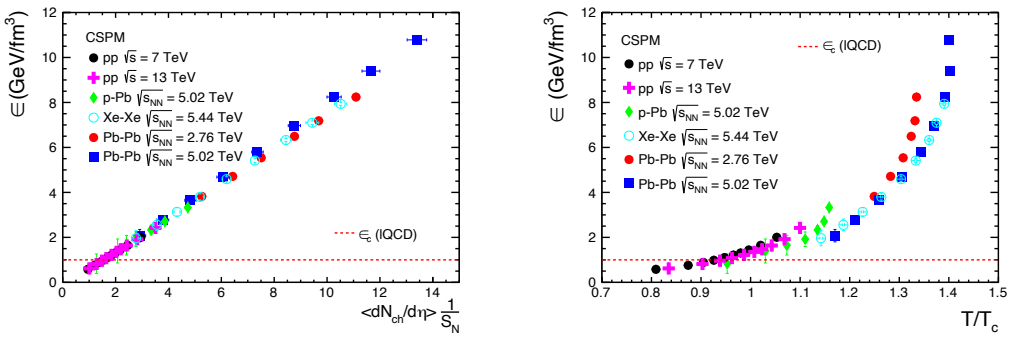

Figure 2.5: Initial energy density as a function of scaled charged particle multiplicity density (left panel) and initial percolation temperature scaled with the critical temperature (right panel) for pp collisions at $\sqrt{s} = 7$ and 13 TeV, p–Pb collisions at $\sqrt{s_{\rm NN}} = 5.02$ TeV, Xe–Xe collisions at $\sqrt{s_{\rm NN}} = 5.44$ TeV, Pb–Pb collisions at $\sqrt{s_{\rm NN}} = 2.76$ and 5.02 TeV [50] estimated from the CSPM.

From Fig. 2.5, one can see the behavior of initial energy density as a function of scaled charged particle multiplicity and temperature for various system sizes at different center of mass energies. In the left panel, a universal straight line trend is observed, with high multiplicity pp events crossing the lQCD threshold values, indicating that such events may create a deconfined medium. On the right-hand plot of Fig. 2.5, we have shown the initial energy density as a function of initial temperature. One can observe system-dependent trends in this case, suggesting that initial temperature and system size also play crucial roles in estimating ϵ.

2.3.2 Mean Free Path

Mean free path (λ) is defined as the average distance travelled by a particle after between consecutive collisions. In thermodynamics, the mean free path of a medium is inversely proportional to the number density of the system. Denser is the system, lower is the mean free path. It is given by the following expression;

$$\lambda = \frac{1}{n\sigma}, \tag{2.22}$$

where n is the number density and σ is the scattering cross-section of the particles. For simplicity, in this work, it is assumed that the particles collide elastically.

In CSPM the number density can be written as the effective number of sources per unit volume [29],

$$n = \frac{N_{\text{sources}}}{S_{\text{N}} L}.$$

Now, the area occupied by the strings and the percolation density parameter are related through the following relation $(1 - e^{-\xi})S_{\text{N}}$. Hence, the effective no. of sources can be written as the total area occupied by the strings divided by the area of an effective string,

$$N_{\text{sources}} = \frac{(1 - e^{-\xi})S_{\text{N}}}{S_1 F(\xi)}.$$

Thus, the number density becomes,

$$n = \frac{(1 - e^{-\xi})}{S_1 F(\xi) L}.$$

By using these relations, we obtain the mean free path as [29, 48],

$$\lambda = \frac{L}{(1 - e^{-\xi})}, \tag{2.23}$$

where, L is the length of a string, taken to be 1 fm for simplicity. From the above equation, one can deduce that the mean free path becomes constant for a very large value of ξ. The mean free path of a system is used to estimate the Knudsen number ($Kn = \lambda/R$), which is a proxy for thermalization in any system, where R is the system size. If $Kn << 1$, then the system is thermalized. Thus, mean-free path is essential to understand the degree of thermalization in a medium.

From the left panel of Fig. 2.6, we observe that λ decreases with increasing charged-particle multiplicity. The values for high multiplicity pp collisions are almost comparable with those of the heavy-ion collisions. Similarly, the right panel shows λ as a function of temperature for various system sizes and center of mass energies. A universal decreasing trend is observed, and the value is seen to

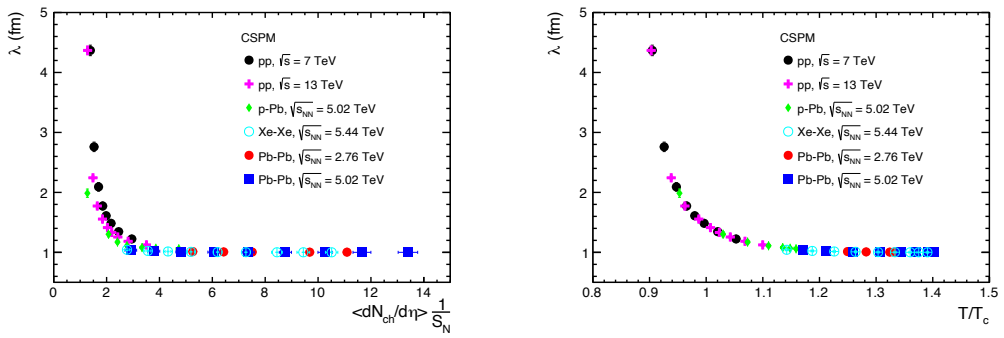

Figure 2.6: Mean free path of the collision systems as a function of scaled charged particle multiplicity density (left panel) and initial percolation temperature scaled with a critical temperature (right panel) for pp collisions at $\sqrt{s} = 7$ and 13 TeV, p–Pb collisions at $\sqrt{s_{\rm NN}} = 5.02$ TeV, Xe–Xe collisions at $\sqrt{s_{\rm NN}} = 5.44$ TeV, Pb–Pb collisions at $\sqrt{s_{\rm NN}} = 2.76$ and 5.02 TeV [50] estimated from the CSPM.

be saturated at 1 fm for high multiplicity pp and heavy-ion events. In ref. [59], the authors have estimated λ using the HRG model, where a similar trend can be observed but with higher values due to hadron gas being a less dense system than a deconfined medium. λ has also been estimated for gas of various particle species using the non-extensive Tsallis statistics in ref. [60] by taking the experimental inputs.

2.3.3 Shear Viscosity to Entropy Density Ratio

The shear viscosity to entropy density ratio is a measure of the fluidity of the system. From the Anti De-Sitter Conformal Field Theory (Ads/CFT) calculations, a lower bound (KSS bound) to the shear viscosity to entropy density ratio (η/s) for any fluid has been estimated. Large values of elliptic flow have been found in the medium formed in heavy-ion collisions at RHIC, which might indicate that the matter formed in such collisions behaves as a nearly perfect fluid having η/s value close to the KSS bound [61]. In a relativistic heavy-ion collision, the shear viscosity of the matter formed is a time-dependent quantity. This suggests that,

in the partonic phase of such collisions, we would expect a very low value of η/s, and after hadronization, it is expected to increase. Several investigations indicate that in the vicinity of a first-order/cross-over phase transition, η/s should reach a minimum but then again start increasing in the deconfined phase [62].

From relativistic kinetic theory, the shear viscosity to entropy density ratio can be expressed as [48].

$$\eta/s \simeq \frac{T\lambda}{5}$$

We then substitute the expression of the mean free path from Eq. 2.20 in the above equation. The final expression for the shear viscosity to entropy density ratio in the CSPM formalism is given by,

$$\eta/s = \frac{TL}{5(1-e^{-\xi})} \tag{2.24}$$

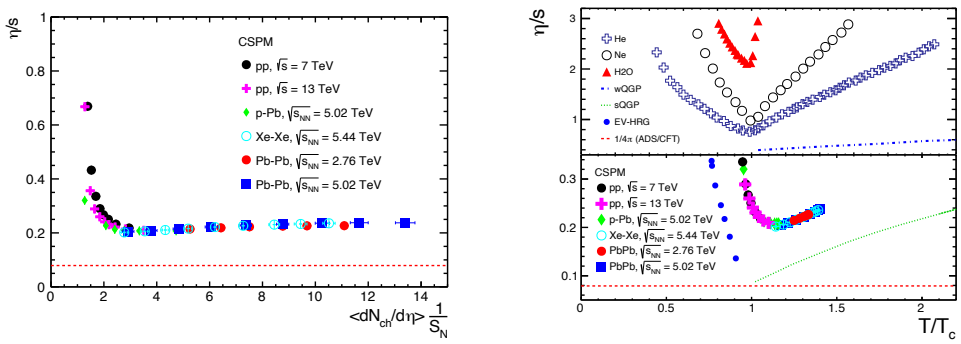

Figure 2.7: The ratio of shear viscosity to entropy density as a function of scaled charged particle multiplicity density (left panel) and initial percolation temperature scaled with critical temperature (right panel) for pp collisions at $\sqrt{s} = 7$ and 13 TeV, p–Pb collisions at $\sqrt{s_{\rm NN}} = 5.02$ TeV, Xe–Xe collisions at $\sqrt{s_{\rm NN}} = 5.44$ TeV, Pb–Pb collisions at $\sqrt{s_{\rm NN}} = 2.76$ and 5.02 TeV [50] estimated from the CSPM.

In the left panel of Fig. 2.7, we show the variation of η/s as a function of scaled charged-particle multiplicity. A minima can be observed at high multiplicity

pp and peripheral heavy-ion events. In the right panel of Fig. 2.7, our results show a minimum around T_c, while it again starts to increase with increasing temperature. The results are compared with the predictions from AdS/CFT conjecture [61], excluded volume hadron resonance gas model [63] as well as with physical systems like helium (He), neon (Ne) and water (H_2O) [64]. The results are also compared with the estimations for the weakly interacting (wQGP) and strongly interacting (sQGP) coupled QCD plasma [65]. It can be clearly seen that η/s of the deconfined medium is the lowest compared to any other known material found in nature, thus making the system almost a perfect fluid.

2.3.4 Speed of Sound

The speed of sound (c_s) is defined as the distance travelled by a sound wave in any elastic medium per unit time. It can be defined for any continuous media from the Euler's equation. It describes the conversion of the change in the energy density profile of the created medium into the pressure gradient. In hydrodynamics, collective expansion is observed because of the pressure gradient created in the medium. It is an essential observable as this can give us information about the equation of state of the system. The lQCD predicts a minimum of c_s^2 near the critical temperature [22, 66]. Moreover, c_s^2 for a hadron gas is 1/5, whereas for a massless ideal gas it is 1/3. This helps us to characterize the systems formed in ultra-relativistic collisions, ultimately to state whether the system behaves like a hadron gas or more like a massless ideal gas.

From boost-invariant Bjorken 1D hydrodynamics, the squared speed of sound is given by [29],

$$\frac{1}{T}\frac{dT}{d\tau} = -c_s^2/\tau, \tag{2.25}$$

where τ is the proper time. The proper time derivative of temperature can be

otherwise written as,

$$\frac{dT}{d\tau} = \frac{dT}{d\epsilon}\frac{d\epsilon}{d\tau}.$$

By differentiating the initial energy density with proper time, we get

$$\frac{d\epsilon}{d\tau} = -Ts/\tau,$$

where s is the entropy density, which is given by $s = (\epsilon + P)/T$, and $P = (\epsilon - \Delta T^4)/3$. By using the above expressions in Eq. 2.25 and simplifying, we get,

$$\frac{dT}{d\epsilon}s = c_s^2.$$

In the CSPM approach, the above expression can be simplified and written in terms of the percolation density parameter (ξ) as [29],

$$c_s^2 = (-0.33)\left(\frac{\xi e^{-\xi}}{1-e^{-\xi}} - 1\right) + 0.0191(\Delta/3)\left(\frac{\xi e^{-\xi}}{(1-e^{-\xi})^2} - \frac{1}{1-e^{-\xi}}\right), \quad (2.26)$$

where, $\Delta = (\epsilon - 3P)/T^4$ is the trace anomaly.

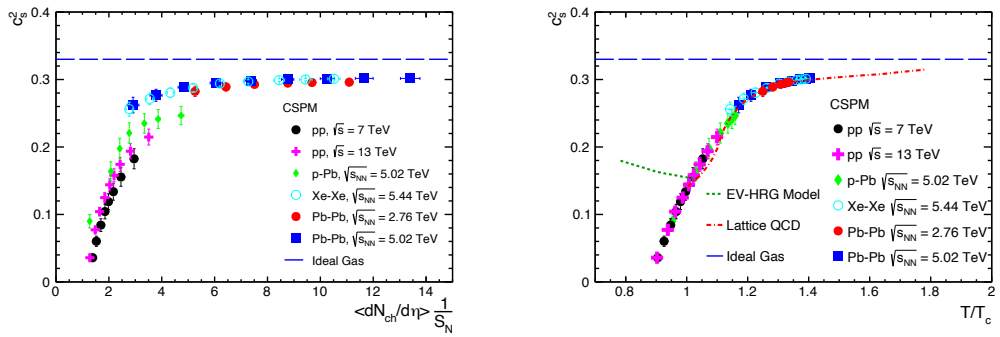

Figure 2.8: Squared speed of sound as a function of scaled charged particle multiplicity density (left panel) and initial percolation temperature scaled with the critical temperature (right panel) for pp collisions at $\sqrt{s} = 7$ and 13 TeV, p–Pb collisions at $\sqrt{s_{\rm NN}} = 5.02$ TeV, Xe–Xe collisions at $\sqrt{s_{\rm NN}} = 5.44$ TeV, Pb–Pb collisions at $\sqrt{s_{\rm NN}} = 2.76$ and 5.02 TeV [50] estimated from the CSPM.

Fig. 2.8, shows the variation of $c_{\rm s}^2$ as a function of scaled charged particle multiplicity in the left panel. Regardless of system sizes, an increasing trend is

observed, which gets saturated after a $\langle dN_{\rm ch}/d\eta \rangle \simeq 10$–$20$ approaching the ideal gas limit. On the right panel, our results are compared with the lattice QCD predictions [67] and excluded volume hadron resonance gas model [63]. A good agreement can be seen between the CSPM and lQCD estimations.

2.3.5 Bulk Viscosity to Entropy Density Ratio

Bulk viscosity (ζ) or volume viscosity is the property that characterizes the flow of a fluid. The bulk viscosity is relevant only if the density of the medium is changing. It plays an important role in attenuating sound waves in fluids and can be estimated from the magnitude of the attenuation. For an almost incompressible fluid, the changes in density can be ignored. Due to longitudinal expansion, the energy density decreases with proper time in the perfect fluid limit. In the meantime, the viscosity prevents the system from performing useful work while expanding longitudinally. The study of bulk viscosity to entropy density ratio (ζ/s) is crucial as it can quantify the critical charged particle multiplicity density, after which a change in the system's dynamics can be observed.

From the relaxation time approximation, the bulk viscosity of a system is given as [68],

$$\zeta = 15\eta\left(\frac{1}{3} - c_{\rm s}^2\right)^2.$$

The bulk viscosity to entropy density ratio can be written as [48],

$$\zeta/s = 15\frac{\eta}{s}\left(\frac{1}{3} - c_{\rm s}^2\right)^2. \tag{2.27}$$

We have estimated the values of ζ/s by using the above expression. The left panel of Fig. 2.9 shows the bulk viscosity to entropy density ratio as a function of scaled charged-particle multiplicity. A decreasing trend can be observed, with ζ/s being lower for higher multiplicities. The bulk viscosity rises dramatically near the phase transition, which was also seen in lQCD estimations [69]. A large bulk viscosity suggests a strong coupling between the dilatational modes of the system

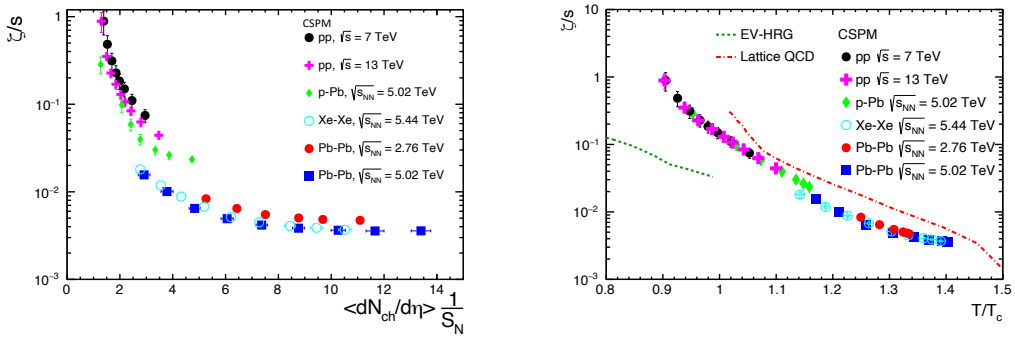

Figure 2.9: The ratio of bulk viscosity to entropy density as a function of charged particle multiplicity density (left panel) and initial percolation temperature scaled with critical temperature (right panel) for pp collisions at $\sqrt{s} = 7$ and 13 TeV, p–Pb collisions at $\sqrt{s_{\rm NN}} = 5.02$ TeV, Xe–Xe collisions at $\sqrt{s_{\rm NN}} = 5.44$ TeV, Pb–Pb collisions at $\sqrt{s_{\rm NN}} = 2.76$ and 5.02 TeV [50] estimated from the CSPM.

and the internal degrees of freedom. Our results are also compared with the excluded volume hadron resonance gas model [63], in the right panel of Fig. 2.9, for a hadronic sector comparison.

2.3.6 Isothermal compressibility

Isothermal compressibility ($\kappa_{\rm T}$) is defined as the change in the volume of a system with a change in pressure at constant temperature. For a perfect fluid, $\kappa_{\rm T}$ is zero, suggesting it is incompressible. Thus, isothermal compressibility can tell us about the deviation of a system from a perfect fluid. It is also related to the number fluctuation in the system, making it one of the useful thermodynamic properties that can be estimated from experimental data inputs [70, 71].

In the Grand Canonical Ensemble (GCE) framework, the variance (σ^2) of N number of particles is directly related to the isothermal compressibility [72],

$$\sigma^2 = \frac{k_{\rm B}T\langle N\rangle^2}{V}\kappa_{\rm T},$$

where $k_{\rm B}$ is the Boltzmann constant. The charged particle multiplicity fluctuations can be characterized by scaled variances of the multiplicity distributions such as,

$$\omega_{\rm ch} = \frac{\langle N_{\rm ch}^2\rangle - \langle N_{\rm ch}\rangle^2}{\langle N_{\rm ch}\rangle} = \frac{\sigma^2}{\mu}$$

where $N_{\rm ch}$ is the charged particle multiplicity per event, and $\mu = \langle N_{\rm ch}\rangle$. From the above two equations, we get

$$\omega_{\rm ch} = \frac{k_{\rm B}T\mu}{V}\kappa_{\rm T}, \tag{2.28}$$

This equation has been used to estimate the upper limit of isothermal compressibility in Pb–Pb collisions at $\sqrt{s_{\rm NN}} = 2.76$ TeV in ALICE [71].

From basic thermodynamics, the isothermal compressibility is given as,

$$\kappa_{\rm T} = -\frac{1}{V}\frac{\partial V}{\partial P}\bigg|_T, \tag{2.29}$$

where V, P, and T are the volume, pressure and temperature of the system, respectively. To express this thermodynamic quantity in terms of the CSPM parameter, we write,

$$\kappa_{\rm T} = -\frac{1}{V}\frac{\partial V}{\partial \xi}\frac{\partial \xi}{\partial P} \Rightarrow \kappa_{\rm T} = -\frac{1}{V}\frac{\partial V}{\partial \xi}\frac{1}{\frac{\partial P}{\partial \xi}} \tag{2.30}$$

The volume, in this case, can be defined as $V = S_{\rm N}L$, where L is the longitudinal dimension of the string ($\sim$ 1 fm). Also, pressure can be defined as, $P = (\epsilon - \Delta T^4)/3$, where ϵ is the energy density given by Bjorken hydrodynamics and Δ is the trace anomaly [48]. The energy density is given by Eq. 2.18. By using these values and simplifying, we finally get

$$\kappa_{\rm T} = \frac{1}{\frac{\langle m_{\rm T}\rangle dN_{ch}/dy}{2\tau_{\rm pro}S_{\rm N}} - \frac{5T^3e^{-\xi}\xi}{3L}}. \tag{2.31}$$

Fig. 2.10 shows the variation of $\kappa_{\rm T}$ as a function of final state charged particle multiplicity in the left panel and as a function of temperature in the right panel.

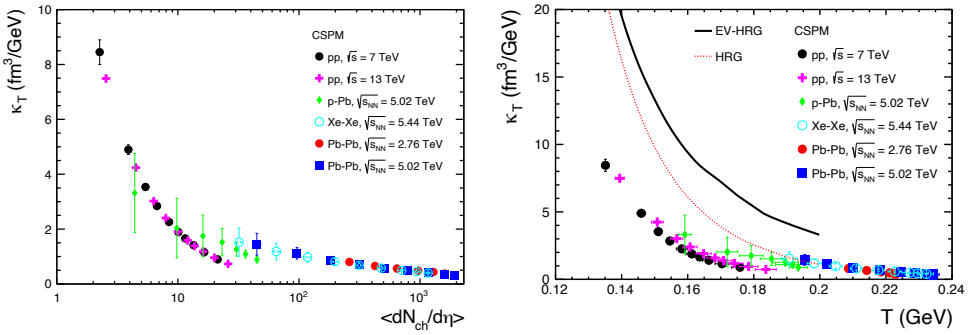

Figure 2.10: κ_{T} as a function of charged particle multiplicity (left panel) and as a function of temperature (right panel) for pp collisions at $\sqrt{s} = 7$ and 13 TeV, p–Pb collisions at $\sqrt{s_{\mathrm{NN}}} = 5.02$ TeV, Xe–Xe collisions at $\sqrt{s_{\mathrm{NN}}} = 5.44$ TeV and Pb–Pb collisions at $\sqrt{s_{\mathrm{NN}}} = 2.76$ and 5.02 TeV [39] estimated from the CSPM.

We observe that κ_{T} decreases with increasing $\langle dN_{\mathrm{ch}}/d\eta \rangle$; however, a slight system size dependency is observed as one goes from small systems to heavy-ion systems. The value of isothermal compressibility is the lowest for most central heavy-ion collisions. However, high multiplicity pp collision gives a similar value of κ_{T} compared to peripheral heavy-ion collisions. On the other hand, the trend of κ_{T} as a function of temperature shows a universal decreasing trend. We have also shown the HRG and EVHRG model estimations for model comparison [73].

For liquids, the value of isothermal compressibility is expected to be small because a unitary change in pressure causes a very small volume change. In contrast, for a gaseous system κ_{T} is expected to be higher. Our result suggests that at the highest charged particle multiplicity, the value of isothermal compressibility is lowest and close to zero. This could be related to the liquid-like behavior of QCD matter. The sudden decrease in κ_{T} as a function of $\langle dN_{\mathrm{ch}}/d\eta \rangle$ could indicate possible system dynamics change. Moreover, the reported values of isothermal compressibility for water at room temperature and mercury are 6.62×10^{42} fm^3/GeV [74] and 5.33×10^{41} fm^3/GeV [75], respectively, which are

very high compared to the value obtained for the QCD matter for the most central Pb–Pb collisions. This indicates QGP is the closest to a perfect fluid found in nature. This measurement nicely complements the measurements of lowest shear viscosity to entropy density ratio for a possible QGP medium [61].

2.3.7 Bulk Modulus

A system's bulk modulus (B) measures its degree of resistance to any external compression. It is the inverse of isothermal compressibility and is defined as the infinitesimal change in pressure with respect to the resulting change in the volume of the system. It can be expressed as

$$B = -V\frac{\partial P}{\partial V} \tag{2.32}$$

Thus, the bulk modulus is,

$$B = \frac{1}{\kappa_{\mathrm{T}}}, \tag{2.33}$$

where, κ_{T} is given by Eq. 2.31. The bulk modulus gives information about the coupling of the constituents in a system – the higher the value of the bulk modulus, the higher the degree of coupling.

Fig. 2.11 shows the bulk modulus as a function of scaled final state charged particle multiplicity in the left panel and scaled temperature in the right panel. A universal increasing trend can be seen for bulk modulus, with the *pp* system giving the lowest B values and the most central Pb–Pb system giving the highest. This means that the most central Pb–Pb system, where one can expect a QGP medium, is the most resistant to external pressure. Here, we also observe that high multiplicity *pp* events show similar values compared to peripheral heavy-ion systems.

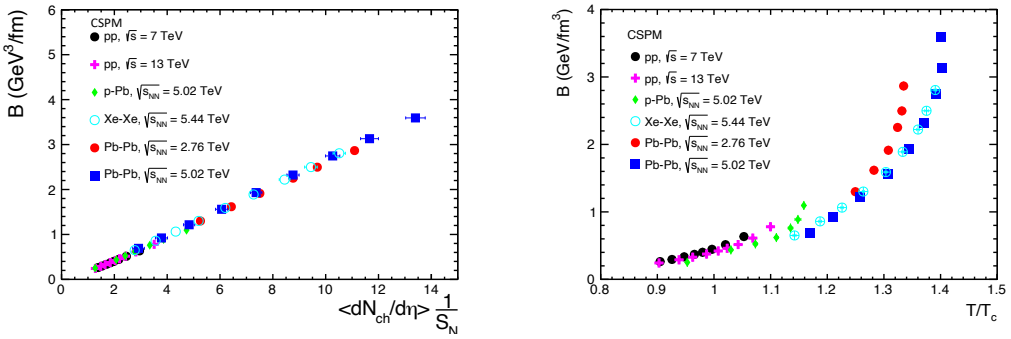

Figure 2.11: Bulk modulus as a function of charged particle multiplicity density (left panel) and initial percolation temperature scaled with the critical temperature (right panel) for pp collisions at $\sqrt{s} = 7$ and 13 TeV, p–Pb collisions at $\sqrt{s_{\rm NN}}$ = 5.02 TeV, Xe–Xe collisions at $\sqrt{s_{\rm NN}} = 5.44$ TeV, Pb–Pb collisions at $\sqrt{s_{\rm NN}} =$ 2.76 and 5.02 TeV [50] estimated from the CSPM.

2.3.8 Jet transport coefficient

When comparing central and peripheral collisions, the final state hadrons created in ultra-relativistic collisions at enormous transverse momenta are significantly suppressed. The suppression of hadrons at high $p_{\rm T}$, also termed jet quenching, is believed to be due to parton energy loss caused by numerous collisions in the strongly interacting medium. It is also associated with the energetic partons' internal $p_{\rm T}$ broadening. The following formula can be used to estimate the jet transport coefficient ($\hat{q}$) within the context of kinetic theory, which is the measure of jet quenching in the medium [76],

$$\hat{q} = n \int d^2q_\perp \; q_\perp^2 \frac{d\sigma}{d^2q_\perp}, \tag{2.34}$$

where n is the number density of the constituents of the medium and $\frac{d\sigma}{d^2q_\perp}$ denotes the differential scattering cross-section of the particles inside the medium.

The transport parameter of jet quenching, $\hat{q}$, and the shear viscosity-to-entropy density ratio (η/s), transport parameters describing the exchange of

energy and momentum between fast partons and medium, are directly related to each other by the relation [77–79],

$$\frac{\eta}{s} \approx \frac{3}{2}\frac{T^3}{\hat{q}} \tag{2.35}$$

One can get the final expression for the jet transport coefficient from Eq. 2.24 and Eq. 2.31 as:

$$\hat{q} \approx \frac{3}{2}\frac{T^3}{\eta/s} \approx \frac{15}{2}\frac{T^2(1-e^{-\xi})}{L} \tag{2.36}$$

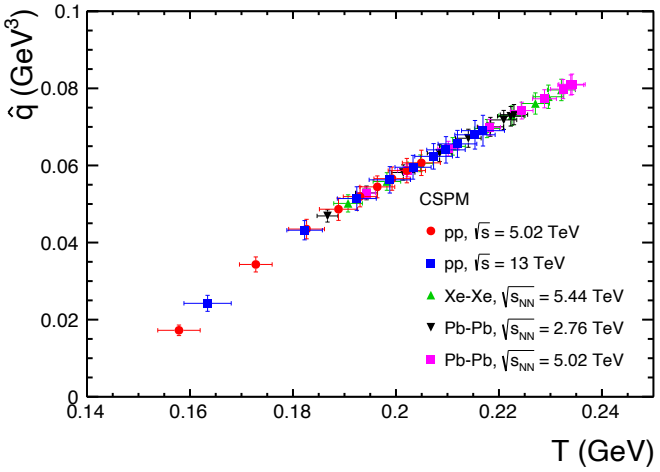

Figure 2.12: Jet quenching parameter $\hat{q}$ as a function of temperature within the CSPM for pp collisions at $\sqrt{s} = 5.02$ and 13 TeV, Xe–Xe collisions at $\sqrt{s_{\rm NN}} = 5.44$ TeV and Pb–Pb collisions at $\sqrt{s_{\rm NN}} = 2.76$ and 5.02 TeV [81] estimated from the CSPM.

The jet quenching parameter $\hat{q}$ is shown as a function of the initial percolation temperature in Fig. 2.12. For both pp and A–A collisions, we see a linear increase in $\hat{q}$ as temperature increases. At low temperatures, the jet quenching parameter has a value of around 0.02 GeV. At high temperatures, its value steadily rises to a maximum of 0.08 GeV.

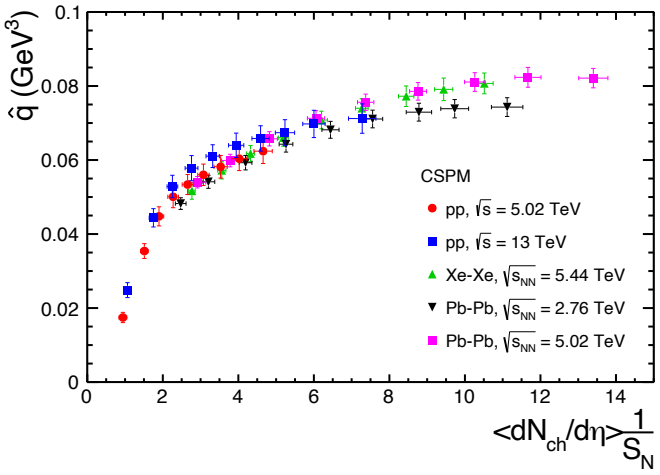

Figure 2.13: Jet quenching parameter $\hat{q}$ as a function charged particle multiplicity scaled with transverse overlap area ($S_\perp$) within the CSPM for pp collisions at $\sqrt{s}$ = 5.02 and 13 TeV, Xe–Xe collisions at $\sqrt{s_{\rm NN}}$ = 5.44 TeV and Pb–Pb collisions at $\sqrt{s_{\rm NN}}$ = 2.76 and 5.02 TeV [81] estimated from the CSPM.

The Jet collaboration has also estimated $\hat{q}$ values with initial temperatures of T_0 = 346–373 (RHIC) and 447–486 MeV (LHC) from five distinct hydrodynamic models. Different hydrodynamic models' interpretations of $\hat{q}$ are regarded as theoretical uncertainty. The scaled jet quenching parameter $\hat{q}/T^3$ at the highest temperatures reached in the most central Au–Au and Pb–Pb collisions are [80]

$$\frac{\hat{q}}{T^3} \approx \begin{cases} 4.6 \pm 1.2 & \text{at RHIC} \\ 3.7 \pm 1.4 & \text{at LHC.} \end{cases}$$

The corresponding absolute values for $\hat{q}$ for a 10 GeV quark jet are,

$$\hat{q} \approx \begin{cases} 0.23 \pm 0.05 \\ 0.37 \pm 0.13 \end{cases} \text{GeV}^3 \text{ at } \begin{matrix} \text{T = 346-373 MeV (RHIC),} \\ \text{T = 447-486 MeV (LHC),} \end{matrix}$$

at an initial time $\tau_0 = 0.6$ fm/c.

In our work, we use the charged particle spectra to calculate $\hat{q}$ within the CSPM approach, hence we can't reach the initial temperature used by the JET

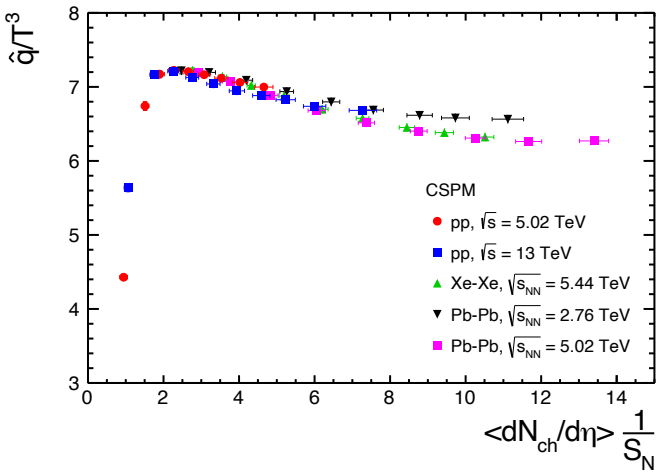

Figure 2.14: $\hat{q}/T^3$ vs charged particle multiplicity scaled by $S_\perp$ for pp collisions at $\sqrt{s}$ = 5.02 and 13 TeV, Xe–Xe collisions at $\sqrt{s_{\rm NN}}$ = 5.44 TeV and Pb–Pb collisions at $\sqrt{s_{\rm NN}}$ = 2.76 and 5.02 TeV [81] estimated from the CSPM.

collaboration. Therefore, our $\hat{q}$ is significantly smaller than the value published by the JET collaboration for the most central Pb–Pb collisions at $\sqrt{s}$ = 2.76 TeV at the LHC.

In Fig. 2.13, we have plotted $\hat{q}$ as a function of charged particle multiplicity scaled with transverse overlap area for pp collisions at $\sqrt{s}$ = 5.02 and 13 TeV, Xe–Xe collisions at $\sqrt{s_{\rm NN}}$ = 5.44 TeV and Pb–Pb collisions at $\sqrt{s_{\rm NN}}$ = 2.76 and 5.02 TeV. One can see that $\hat{q}$ shows a steep increase at lower charged particle multiplicities in pp collisions and gets saturated at very high multiplicity for all studied energies. This behaviour suggests that at lower multiplicities, the system is not dense enough to highly quench the partonic jets, whereas, with the increase of multiplicity, the quenching of jets becomes more prominent.

The dimensionless quantity, $\hat{q}/T^3$, is shown in Fig. 2.14 as a function of charged particle multiplicity scaled with transverse overlap area. In the low multiplicity regime, we observe a steep increase in $\hat{q}/T^3$, and after reaching a maximum at $\langle d{\rm N_{ch}}/{\rm d}\eta\rangle/{\rm S_N} \sim 2$ it starts decreasing regardless of the collision system or collision energy. The $\hat{q}/T^3$ decreases faster in Pb–Pb and Xe–Xe than

in the *pp* collisions.

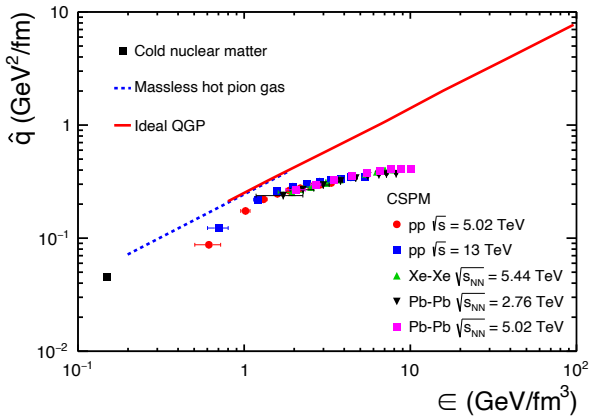

Figure 2.15: Jet quenching parameter $\hat{q}$ as a function of initial energy density for *pp* collisions at $\sqrt{s} = 5.02$ and 13 TeV, Xe–Xe collisions at $\sqrt{s_{\rm NN}} = 5.44$ TeV and Pb–Pb collisions at $\sqrt{s_{\rm NN}} = 2.76$ and 5.02 TeV [81]. The blue dotted line is for massless pion gas, the solid red curve is for ideal QGP, and the black square is for cold nuclear matter [82] estimated from the CSPM.

The variation of $\hat{q}$ as a function of initial energy density is shown in Fig. 2.15. To better understand, we have compared our results with cold nuclear matter, massless hot pion gas, and ideal QGP calculations [82]. Our CSPM result is closer to the massless hot pion gas at low energy density. As initial energy density increases, $\hat{q}$ values increase and then show a saturation towards heavy-ion collisions, which produce a denser medium. The saturation behaviour observed at high energy densities suggests that $\hat{q}$ remains unaffected after a certain energy density. Similar behaviour is observed when $\hat{q}$ is studied as a function of multiplicity (shown in Fig. 2.13). The jet energy loss inside a denser QCD medium goes toward saturation after a threshold in the final state multiplicity is reached. If we compare the behaviour of η/s as a function of T/T_c for $T > T_c$ (the domain of validity of CSPM), we observe an increasing trend, which in principle should be reflected reversely in the observable $\hat{q}/T^3$. However, the interplay of higher

temperature and lower η/s decides the high-temperature behavior of $\hat{q}$ as shown in Fig. 2.15. Further, one observes the CSPM-based estimations of $\hat{q}$ showing a deviation from the ideal QGP behaviour for energy densities higher than 1 GeV/fm^3. This is because the ideal QGP calculations of Ref. [82], assumes ϵ/T^4 a constant value, whereas the CSPM-based estimations show an increasing trend of ϵ/T^4 towards high temperature (energy density or final state multiplicity) [83].

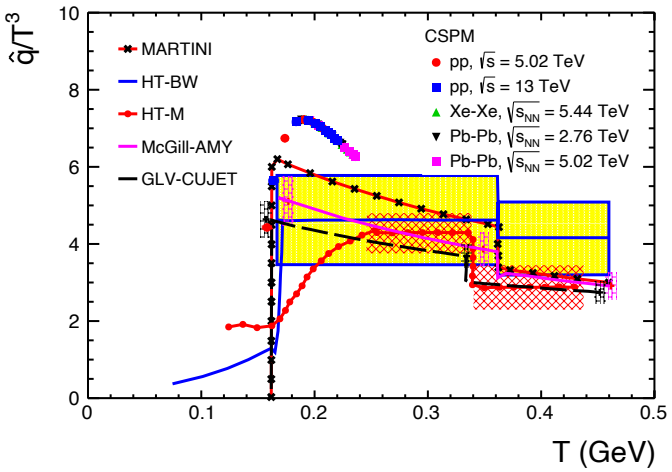

Figure 2.16: Scaled jet quenching parameter $\hat{q}/T^3$ as a function of initial temperature for pp collisions at $\sqrt{s}$ = 5.02 and 13 TeV, Xe–Xe collisions at $\sqrt{s_{\rm NN}}$ = 5.44 TeV and Pb–Pb collisions at $\sqrt{s_{\rm NN}}$ = 2.76 and 5.02 TeV [81] estimated from the CSPM.

The $\hat{q}/T^3$ as a function of initial temperature from five alternative theoretical models that account for particle energy loss in the medium are shown in Fig. 2.16 together with our CSPM estimations. The Gyulassy–Levai–Vitev (GLV) model [84] predicted how the high transverse momentum pion nuclear modification factor would change as energy levels increased from SPS and RHIC to the LHC. By considering the impacts of the multi-scale running of the QCD coupling $\alpha(Q^2)$, CUJET 1.0 model was able to explain why $R_{\rm AA}$ at RHIC and LHC were identical [85]. The scaled $\hat{q}$ was calculated by the combined GLV-

CUJET. In order to describe the space-time ecolution of the local temperature and flow velocity in the medium throughout the jet propagation route, the HT-BW (High Twist-Berkeley–Wuhan) model applies 3+1D ideal hydrodynamics [86]. The HT-M (High Twist-Majumder) model provides the space-time evolution of the entropy density using a 2+1D viscous hydrodynamic model [87]. The MARTINI model describes the suppression of hadron spectra in heavy-ion collisions at RHIC with a fixed value for the strong coupling constant [88]. In the MCGILL-AMY (Arnold–Moore–Yaffe) model [89], the evolution of hard jets is derived from the using thermal QCD, hard thermal loop effects, and Landau-Pomeranchuck–Migdal interference. $\hat{q}$ has been estimated from all these various models which take different initial conditions into account. We note that the behaviour of $\hat{q}/T^3$, as determined using the CSPM model, is comparable to that noted by the JET collaboration.

Chapter 3

Hadronic phase lifetime and QGP phase boundary

Tremendous research is going on to understand the evolution of matter produced in ultra-relativistic collisions. The system produced in such collisions goes through various phases with unique and exciting consequences. However, as the whole evolution happens for a very short time period, about a few fm/c (10^{-23} s), it is impossible to have direct experimental observation to obtain any significant conclusions. Thus, it is essential to study and understand the different phases of evolution through necessary theoretical and phenomenological approaches. Minimal attention has been given to estimate the lifetime of the matter produced in such collisions. It is challenging to study the four-dimensional evolution of the system after a collision, as various complicated dynamical processes contribute to the expansion and eventual cooling of the hot and dense matter. Nevertheless, it is crucial to properly understand the QGP phase and the subsequent hadronic phase lifetime. This chapter discusses a possible way to estimate the hadronic phase lifetime by employing a phenomenological toy model.

3.1 Estimating the hadronic phase lifetime

As can be seen from Fig. 3.1, the time interval between the chemical and kinetic freeze-out is the hadronic phase lifetime. After the chemical freeze-out, the inelastic collision seizes, and the particle number gets fixed. In the hadronic phase, the hadrons interact elastically, transferring momenta. However, the highly unstable resonances can decay within the hadronic phase. Their daughter particles can interact with other particles in the medium, thus changing their momenta. Therefore, the information about their parent particles gets lost while doing invariant mass reconstruction, and the yields of the parent particles decrease. This process is called rescattering. On the other hand, two particles in the medium can recombine and form a heavier particle through a process called regeneration, thus increasing the yield of the heavier particle. Previously, the hadronic phase in *pp* collisions was thought to be almost negligible as they are considered small systems and do not produce a QGP-like medium. However, even for heavy-ion collisions, estimating the hadronic phase lifetime is nontrivial. Very few works in the literature have explored this direction [90–92]. Hence, it is essential to have a phenomenological study to estimate the hadronic phase lifetime for various collision systems at different collision energies. In addition, the Monte-Carlo and transport models can be given proper hadronic phase lifetime inputs while studying the heavy-ion collisions to have a better comparison with the experimental data.

3.1.1 Hadronic resonances as probes

We use the hadronic resonance particles to estimate the hadronic phase lifetime of an ultra-relativistic collision. Resonances are the higher excited states of stable hadrons, having higher masses, higher decay widths, thus, lower lifetimes. For example, pion ($\pi^{\pm}, \pi^{0}$) has rho meson ($\rho^{\pm}, \rho^{0}$) as its resonance counterpart, kaon

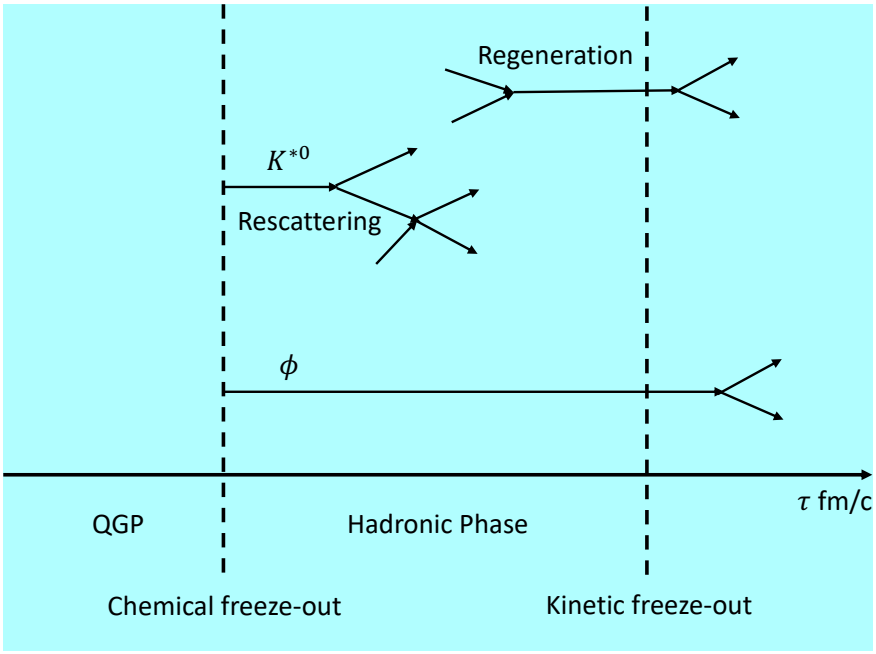

Figure 3.1: A schematic representation of the hadronic phase with rescattering and regeneration.

$(K^0, K^{\pm})$ has K^{0*} and $K^{\pm *}$, lambda (Λ) has Λ^*, etc. These resonances can decay relatively earlier than their stable partners; thus, these can be useful in studying the hadronic phase. However, the value of the lifetimes of the resonances matters. For instance, $\phi(1020)$ is a resonance particle with a lifetime of about 42.6 fm/c. Even though this is very short-lived relative to other stable hadrons such as pions, its lifetime is still relatively high compared to the time period of the evolution of a heavy-ion collision. This means ϕ will not decay in the hadronic phase of the evolution and pass through without significant interactions. Thus, it is a bad probe to study the hadronic phase lifetime. On the other hand, K^{0*} has a lifetime of about 4.26 fm/c, which is comparable to the time period of the evolution of a heavy-ion collision. This makes K^{0*} a better probe to study the hadronic phase lifetime as it can decay within the hadronic phase. One might naively guess that any particle which has a relatively short lifetime can be a

good candidate for our probe. Yet this assumption is premature. For example, ρ^0 has a lifetime of 1.2 fm/c; however, ρ^0 will decay to two pions, which can then easily recombine with each other or other pions present in the hadronic medium, thus, the regeneration effect is also dominant. Hence, the ρ^0/π^0 ratio will remain relatively unaffected throughout the hadronic phase. Considering all the above reasons, we choose K^{0*} as our tool to estimate the hadronic phase lifetime, which has a relatively small regeneration effect. This has also been suggested in literature, where it is observed that the pion-pion interaction cross-section is five times larger than the and pion-kaon interactions cross-section, making the regeneration effect lesser [93, 94]. Nevertheless, considering the effect of even minimal regeneration, the hadronic phase lifetime estimated with K^{0*} as a probe will be the lower limit. An alternative option can be the $\Lambda(1520)$ hyperon, which has a lifetime of 12 fm/c. The hadronic phase lifetime estimated by taking Λ particle as the probe can give us an upper limit for the same.

3.1.2 Hadronic phase lifetime

We employ a simple nuclear decay-type formula to estimate the hadronic phase lifetime. The nuclear decay formula is given by,

$$N_{\mathrm{t}} = N_0 e^{-t/\tau}, \tag{3.1}$$

where, N_0 is the initial nuclear sample, N_{t} is the sample after a time t and τ is the decay lifetime of that sample. Similarly, we can construct a formula to estimate the hadronic phase lifetime. The K^{*0}/K ratio can be used for this purpose. K^{*0} will suffer rescattering and regeneration within the hadronic medium; thus, its number will change throughout the evolution. The ratio with K is taken to eliminate the strangeness quantum number dependency. We then take the modified nuclear decay formula, with $(K^{*0}/K)_{\mathrm{chemical}}$ as our initial sample and $(K^{*0}/K)_{\mathrm{kinetic}}$ as the final sample. $(K^{*0}/K)_{\mathrm{chemical}}$ is the ratio of K^{*0}/K at the

chemical freezeout boundary. As it is not trivial to estimate (K^{*0}/K) ratio at the chemical freeze-out boundary, because we detect the particles after the kinetic freezeout, we have assumed K^{*0}/K of low multiplicity and low energy minimum bias pp collisions to be $(K^{*0}/K)_{\rm chemical}$. It is assumed that in these cases, the hadronic phase will be negligible, making the ratio almost the same as the ratio at chemical freeze-out ($(K^{*0}/K)_{\rm chemical} \sim (K^{*0}/K)_{\rm knietic}$), as K^* will suffer the least amount of rescattering and regeneration. Now, the modified formula becomes,

$$[K^{*0}/K]_{\rm kinetic} = [K^{*0}/K]_{\rm chemical} \times e^{-\Delta t/\tau}, \tag{3.2}$$

where τ is the lifetime of K^{*0} in vaccum in its center of mass frame and Δt is the hadronic phase lifetime. Thus, to change the frame from the particle's center of mass frame to the lab frame, Δt is boosted by the Lorentz factor $(\gamma\Delta t)$. $\gamma = \frac{1}{\sqrt{1-\frac{v^2}{c^2}}}$, is calculated using the mean transverse momentum ($\langle p_{\rm T}\rangle$) of K^{*0}, by using velocity $v = \langle p_{\rm T}\rangle/m$, where m is the mass of K^{*0} and $c = 1$. $\langle p_{\rm T}\rangle$ is used as an approximation for momentum for the measurements at midrapidity.

In Fig. 3.2, the K^{*0}/K ratio for Cu–Cu and Au–Au collision systems at $\sqrt{s_{\rm NN}}$ = 62.4 and 200 GeV at RHIC, pp collision system at $\sqrt{s}$ = 7 TeV, p–Pb collision system at $\sqrt{s_{\rm NN}}$ = 5.02 TeV, and Pb–Pb collision system at $\sqrt{s_{\rm NN}}$ = 2.76 and 5.02 TeV at the LHC is plotted as a function of final state charged-particle multiplicity [92, 96–101]. The ratio decreases almost universally as a function of $\langle dN_{\rm ch}/d\eta\rangle$, although a small dependence on the collision energy is also observed. These values become our sample amount at the kinetic freeze-out boundary. A clear decrease in the K^{*0}/K ratio can be observed regardless of the collision system or collision energy. This suggests the dominance of the rescattering effect over the regeneration effect. Here, one should keep in mind that the rapidity range of $\langle dN_{\rm ch}/d\eta\rangle$ is $|\eta| < 0.5$ for LHC energies and $|\eta| < 1.0$ for RHIC energies. On the other hand, in Fig. 3.3, the K^{*0}/K ratio for low energy minimum bias and low multiplicity pp collisions are plotted as a function of the center of

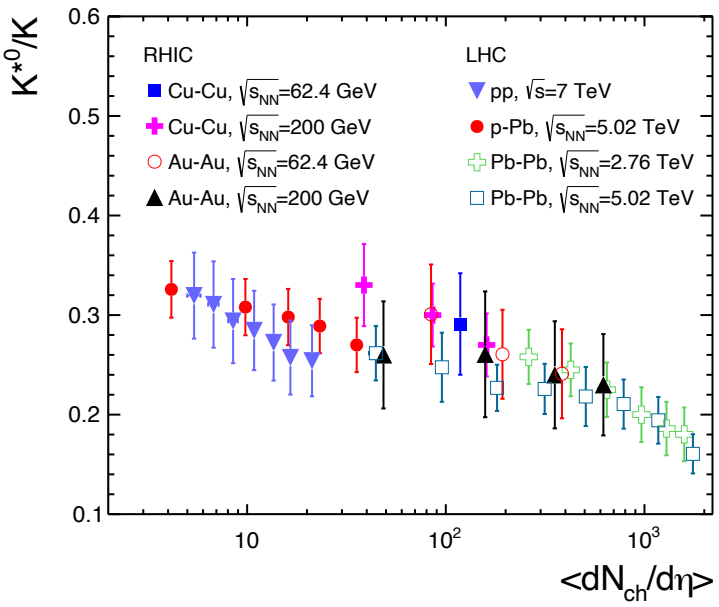

Figure 3.2: K^{*0}/K ratio as a function of charged particle multiplicity for various collision systems and collision energies [95].

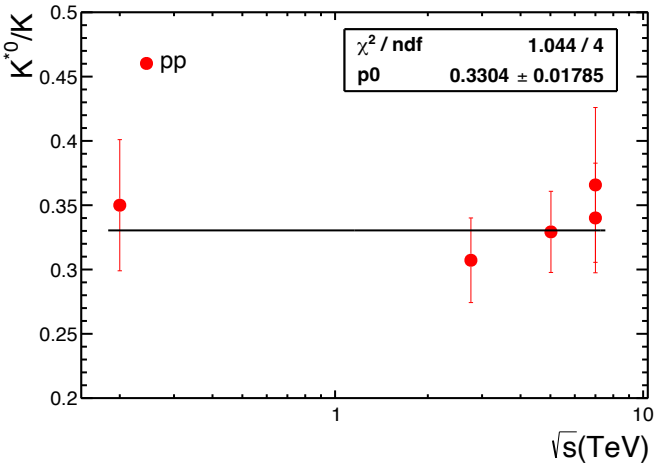

Figure 3.3: K^{*0}/K ratio as a function of the center of mass energies for pp collisions [95].

mass energy. We have then fitted a zeroth order polynomial to the data and obtained an average value of $K^{*0}/K \simeq 0.3304 \pm 0.0178$. This value becomes our initial sample amount at the chemical freeze-out boundary, as we assume that the hadronic phase will be the smallest and almost negligible for low energy and low multiplicity pp collisions.

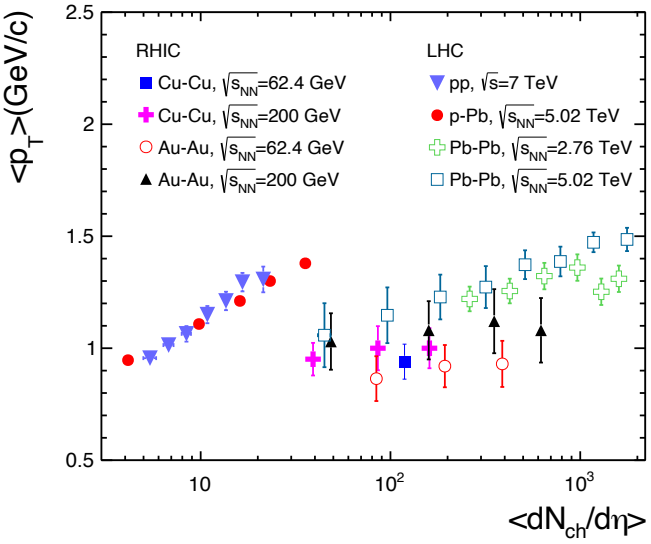

Figure 3.4: Mean transverse momentum of K^{*0} as a function of final state charged particle multiplicity for various collision systems and collision energies [95].

Fig. 3.4 shows the $\langle p_{\mathrm{T}} \rangle$ of K^{*0} as a function of charged particle multiplicity for various collision systems at RHIC and LHC. We see an increasing trend in $\langle p_{\mathrm{T}} \rangle$ with an increase in $\langle dN_{\mathrm{ch}}/d\eta \rangle$, although a clear center of mass energy dependency is observed. The evolution of $\langle p_{\mathrm{T}} \rangle$ across collision systems is not smooth. The trend of the $\langle p_{\mathrm{T}} \rangle$ for small systems, such as pp and p–Pb collisions, are entirely different from those of heavy-ion collisions. The $\langle p_{\mathrm{T}} \rangle$ of the system increases as one progresses to higher domains of collision energy and produces more particles. Particle density in the phase space and $\langle p_{\mathrm{T}} \rangle$ appear to rise in a linked manner. For the same particle density, a greater $\langle p_{\mathrm{T}} \rangle$ would indicate a higher collision rate (rescattering) and, thus, a larger lifespan for the hadronic phase.

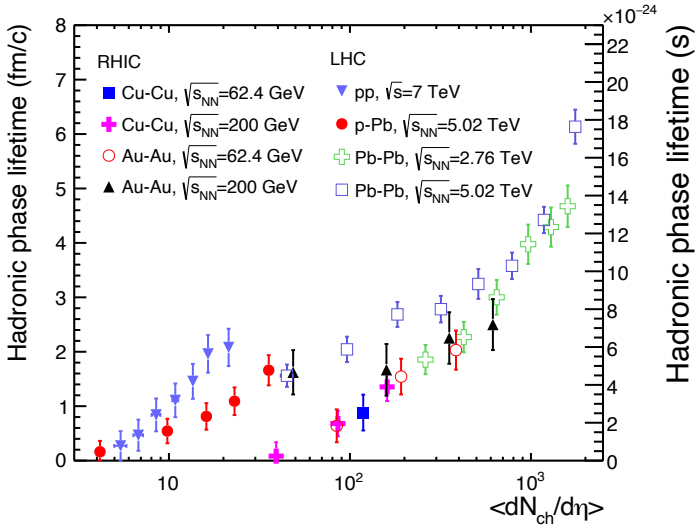

Figure 3.5: Hadronic phase lifetime as a function of charged particle multiplicity for various collision systems and collision energies [95].

We then estimate the hadronic phase lifetime by using the above-mentioned information. As shown in Fig. 3.5, the estimated hadronic phase lifetime using Eq. 3.1 exhibits almost a linear increase as a function of charged particle multiplicity. This implies that for a given charged-particle multiplicity, the hadronic phase lifetime is comparable regardless of the collision energy and collision systems for central heavy-ion collisions like Cu–Cu and Au–Au collisions at RHIC and Pb–Pb collisions at the LHC. The apparent change in trend for peripheral heavy-ion collisions could be attributed to the effect of system size and collision energy; in other words, to the effective energy deposited in the Lorentz contracted region. However, compared to heavy-ion collisions, the trends of the small collision systems at LHC, such as *pp* and p–Pb collisions, are different. This behaviour appears to be propagated from the dependence of $\langle p_{\mathrm{T}} \rangle$ as a function of charged-particle multiplicity. The figure shows how strongly the lifetime changes across collision systems and collision energies. We estimate a finite hadronic phase lifetime for high-multiplicity *pp* collisions of about 2 fm/c, contrasting to

about 6 fm/c for most central Pb–Pb collisions. In Ref. [90], the authors have used a hydrodynamic model to estimate the hadronic phase lifetime. After using 1+1D second-order viscous hydrodynamics in a hadron gas, they have estimated the hadronic phase lifetime for Pb–Pb collisions at $\sqrt{s_{\rm NN}}$ = 5.02 TeV, which is comparable to our estimation. Furthermore, these kinds of studies can provide useful inputs to various event generators such as PYTHIA8 and transport models such as AMPT, where the hadronic phase lifetimes can be set accordingly for a better comparison with data.

3.2 Locating the QGP phase boundary

Much like K^{*0} is used to probe the hadronic phase, ϕ can be used as a tool to locate the QGP phase boundary. ϕ is the lightest bound state of a strange and anti-strange quark ($s\bar{s}$) and is produced relatively early in the evolution compared to pions, kaons and protons. Unlike K^{*0}, ϕ meson is almost unaffected by the rescattering and regeneration processes due to its longer lifetime (42.6 fm/c). This can be noticed from Fig. 3.6 [92]. In addition, it has a very small inelastic scattering cross-section, which means it interacts very little in the hadronic phase with other hadrons. It has also been shown that only 5% of the ϕ mesons rescatter in the hadronic phase of the medium. This percentage also goes down as one moves towards TeV energies, where the matter is almost baryon free. As the interactions of ϕ meson with other hadrons are minimal in the mixed and hadron gas phase, the information of the QGP phase boundary remains unfiltered. These unique qualities make ϕ an excellent probe to study the QGP phase boundary, as it can retain the information from the QGP medium without getting affected in the hadronic phase. Hence, the transverse momentum spectra of ϕ meson will remain unaffected, and thus, one can, in principle, extract useful information about the QGP phase boundary from the ϕ meson $p_{\rm T}$ spectra.

There are various fitting functions in literature which are used to obtain infor-

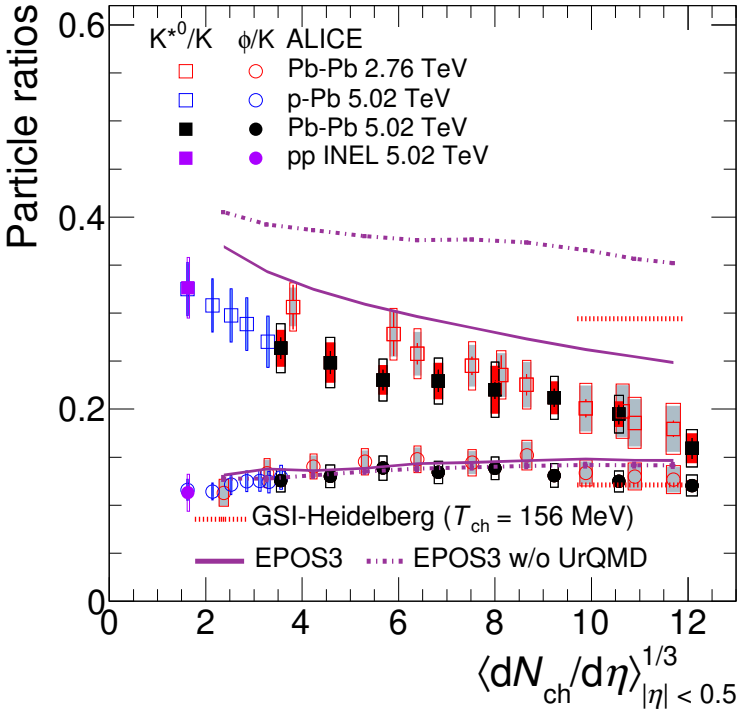

Figure 3.6: K^{*0}/K and ϕ/K ratios for various collision systems and collision energies as functions of final state charged particle multiplicity [92].

mation from the transverse momentum spectra. The most basic yet useful one is the Boltzmann-type exponential function, which is used to extract the temperature of the system. However, this function doesn't explain the spectra beyond the low transverse momentum region. There are also power-law type functions which explain the tail part of the spectra but fail to explain the low transverse momentum region. Tsallis distribution function is an empirical function which is carefully constructed, having the components of both the exponential and power-law type functions [102]. This function describes the transverse momentum spectra up to very high p_{T}. The Tsallis distribution function introduces a new parameter, q, which is the degree of non-equilibrium in the system. Thus, the temperature that one gets from fitting the Tsallis function is not exactly the system's temperature but rather a temperature-like quantity. In Ref. [103], the authors have

proposed a description of the hadron spectra by taking flow into account, which is generally known as the Boltzmann-Gibbs Blastwave (BGBW) function. This essentially gives information of the temperature of the system along with the radial velocity with which the system expands, thus painting a realistic picture of the heavy-ion collisions. We fit the BGBW function to the $p_{\rm T}$ spectra of ϕ meson up to $p_{\rm T} \simeq 3$ GeV/c. We obtain the kinetic freeze-out temperature from the fitting, also known as the thermal temperature ($T_{\rm th}$) and the average velocity of the medium ($\langle\beta\rangle$).

In the BGBW framework, the invariant yield is given as [103],

$$E\frac{d^3N}{dp^3} = D\int d^3\sigma_\mu\ p^\mu exp(-\frac{p^\mu u_\mu}{T}). \tag{3.3}$$

Here, E is the energy, T is temperature, D is the normalisation constant, and the particle four-momentum and four-velocity are respectively given as,

$$p^\mu \ = \ (m_{\rm T}{\rm cosh}y,\ p_{\rm T}\cos\phi,\ p_{\rm T}\sin\phi,\ m_{\rm T}{\rm sinh}y),$$

$$u^\mu = \cosh\rho\ (\cosh\eta,\ \ \tanh\rho\ \cos\phi_r,\ \ \tanh\rho\ \sin\phi_r,\ \ \sinh\ \eta).$$

Here, y and η are rapidity and pseudorapidity, and ϕ and ϕ_r are the azimuthal angles in momentum and coordinate space, respectively. $m_{\rm T} = \sqrt{p_{\rm T}^2 + m^2}$ is the transverse mass.

The kinetic freeze-out surface is parametrized as,

$$d^3\sigma_\mu \ = \ (\cosh\eta,\ 0,\ 0, -\sinh\eta)\ \tau\ r dr\ d\eta\ d\phi_r,$$

where, τ is the proper time. We assume Bjorken correlation in rapidity for simplification, $y = \eta$ [58]. Thus, the BGBW function is expressed as,

$$\left.\frac{d^2N}{dp_{\rm T}dy}\right|_{y=0} = D\ g\int_0^{R_0} r\ dr\ K_1\Big(\frac{m_{\rm T}\ \cosh\rho}{T_{\rm th}}\Big) I_0\Big(\frac{p_{\rm T}\ \sinh\rho}{T_{\rm th}}\Big), \tag{3.4}$$

where, g is the degeneracy factor. $K_1\Big(\frac{m_{\rm T}\ {\rm cosh}\rho}{T_{\rm th}}\Big)$ and $I_0\Big(\frac{p_{\rm T}\ {\rm sinh}\rho}{T_{\rm th}}\Big)$ are the modified Bessel's functions, which are defined as,

$$K_1\Big(\frac{m_{\rm T}\ {\rm cosh}\rho}{T}\Big) = \int_0^\infty {\rm cosh}y\ {\rm exp}\Big(-\frac{m_{\rm T}\ {\rm cosh}y\ {\rm cosh}\rho}{T_{\rm th}}\Big)dy,$$

$$I_0\Big(\frac{p_{\rm T}\,\sinh\rho}{T}\Big) = \frac{1}{2\pi}\int_0^{2\pi} exp\Big(\frac{p_{\rm T}\,\sinh\rho\,\cos\phi}{T_{\rm th}}\Big)d\phi.$$

Here, ρ in the integrand is a parameter given by $\rho = \tanh^{-1}\beta$, with $\beta = \beta_s\,\Big(\xi\Big)^n$ [103] is the radial flow. β_s is the maximum surface velocity and $\xi = \Big(r/R_0\Big)$, where r is the radial distance. For our calculation, we use a linear velocity profile ($n = 1$), and R_0 is the maximum radius of the expanding source at freeze-out ($0 < \xi < 1$). In the BGBW model, the particles that are closer to the center of the fireball move slower than the ones at the edges. The average of the transverse velocity can be evaluated as [104],

$$\langle\beta\rangle = \frac{\int \beta_s\xi^n\xi\; d\xi}{\int \xi\; d\xi} = \Big(\frac{2}{2+n}\Big)\beta_s. \tag{3.5}$$

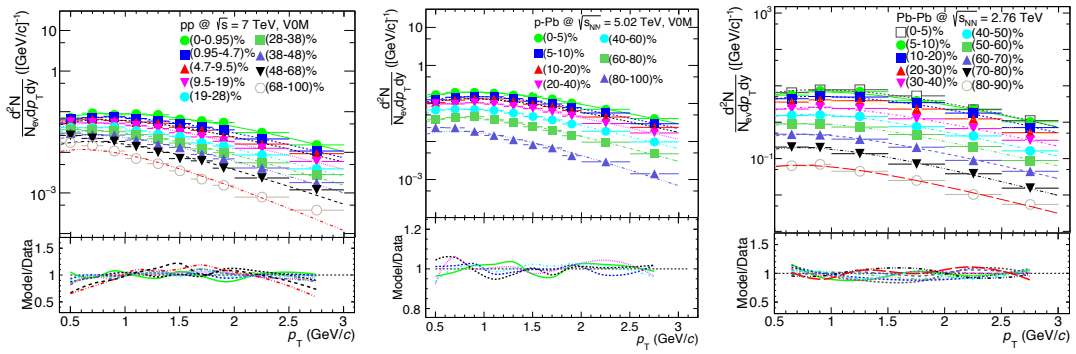

Figure 3.7: Blastwave fits to the transverse momentum spectra of ϕ meson for pp collision at $\sqrt{s} = 7$ TeV, p–Pb collision at $\sqrt{s_{\rm NN}} = 5.02$ TeV and Pb–Pb collision at $\sqrt{s_{\rm NN}} = 2.76$ TeV for various multiplicity classes [95].

The blast-wave fit for $p_{\rm T}$ spectra in pp collisions at $\sqrt{s} = 7$ TeV is shown in the left panel of Fig. 3.7 for various multiplicity classes. Similarly, the middle and right panels of Fig. 3.7 show the blast-wave fit to the $p_{\rm T}$ spectra for p–Pb collisions at $\sqrt{s_{\rm NN}} = 5.02$ TeV and Pb–Pb collisions at $\sqrt{s_{\rm NN}} = 2.76$ TeV respectively. The fitting is done to the soft part of the $p_{\rm T}$ spectra up to $p_{\rm T} = 3$ GeV/c, which has thermal information of the system. The fit-to-data ratio is displayed in the lower panels of the figures. For Pb–Pb, p–Pb, and high-multiplicity pp collisions, the

highest fit variation does not exceed 10%, and the fit qualities are reasonable. Due to the less likely blast-wave situation in low-multiplicity *pp* collisions, the fit quality is lower, which is expected for these collisions.

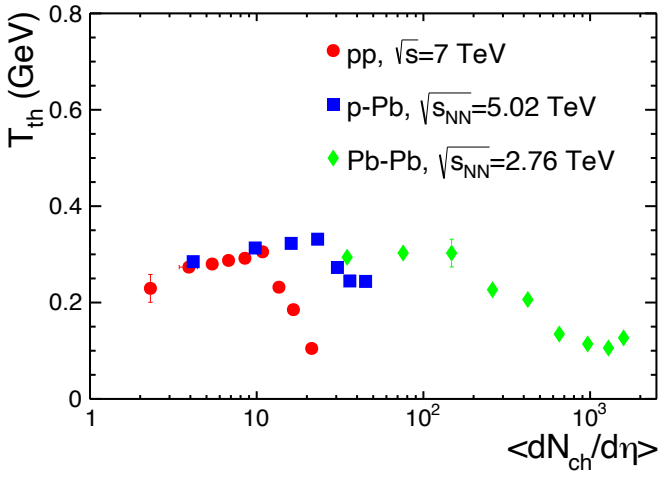

Figure 3.8: Thermal temperature of ϕ mesons as a function of charged particle multiplicity for *pp* collision at $\sqrt{s} = 7$ TeV, p–Pb collision at $\sqrt{s_{\rm NN}} = 5.02$ TeV and Pb–Pb collision at $\sqrt{s_{\rm NN}} = 2.76$ TeV [95].

We extract the values of and $T_{\rm th}$ for all collision systems in various multiplicities from these fits, which can be used in the following equation; $T_{\rm eff} = T_{\rm th} + \frac{1}{2}m\langle\beta\rangle^2$, to determine the effective temperature ($T_{\rm eff}$) of the ϕ mesons. It is noteworthy that this formula is only valid for $p_{\rm T} \lesssim 3$ GeV/c. For high $p_{\rm T}$, one uses a Doppler-modified formula. Fig. 3.8 depicts the relationship between charged-particle multiplicity and the kinetic freeze-out temperature for ϕ meson, designated by $T_{\rm th}$. One can see that the temperature essentially maintains a flat trend until a specific $\langle dN_{\rm ch}/d\eta\rangle$, at which point it suddenly begins to decline. This can be explained by considering that the system freezes out early for low charged-particle multiplicity, which means it freezes out at high $T_{\rm th}$. However, the system is assumed to have experienced a QGP phase as the multiplicity of charged particles increases, which leads to the system taking a longer time to

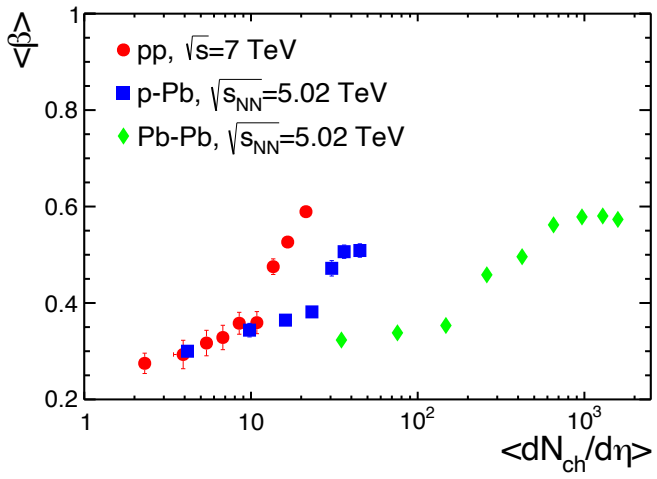

Figure 3.9: Average radial velocity of ϕ mesons as a function of charged particle multiplicity for pp collision at $\sqrt{s}$ = 7 TeV, p–Pb collision at $\sqrt{s_{\rm NN}}$ = 5.02 TeV and Pb–Pb collision at $\sqrt{s_{\rm NN}}$ = 2.76 TeV [95].

reach the kinetic freeze-out, thus decreasing the $T_{\rm th}$. This argument is further supported by our observations of longer hadronic phase lifetimes for collisions with higher multiplicities. As a result, the temperature at which kinetic freeze-out occurs in all the collision systems rapidly drops after a certain $\langle dN_{\rm ch}/d\eta\rangle$. We also note that the $T_{\rm th}$ decreases in several collision systems at various charged-particle multiplicities.

Fig. 3.9 shows the average radial flow velocity for several collision systems at the LHC as a function of final state charged-particle multiplicity. It is evident that, up to a point, the trend grows steadily in all collision systems. On the other hand, it exhibits a dramatic increase for pp collisions at a specific charged-particle multiplicity $\langle dN_{\rm ch}/d\eta\rangle \simeq$(10–20). The following additional observations for a shift in system dynamics confirm the detection of this threshold in the final-state multiplicity of charged particles. The limit beyond which the multipartonic interactions (MPI) in pp collisions begin to play a significant role in particle production (mainly quarkonia) at the LHC energies has been determined to be

$N \simeq 10$–20 [105]. The thermodynamic limit beyond which all statistical ensembles describe the freeze-out characteristics of the system is likewise supported by this threshold [106]. We have also noted that the chemical freeze-out temperature, $T_{\rm ch}$, is higher than the kinetic freeze-out temperature after this threshold. We know that a system going through the QGP phase has a greater average radial flow. Once more, this shows a greater likelihood of QGP production following this specific charged-particle multiplicity, which may have been the cause of the abrupt increase in $\langle\beta\rangle$. In addition, as we have discussed in the previous chapter, this threshold of charged particle multiplicity signifies a change in dynamics in the system and may hint towards the possible formation of QGP droplets in high multiplicity *pp* collisions.

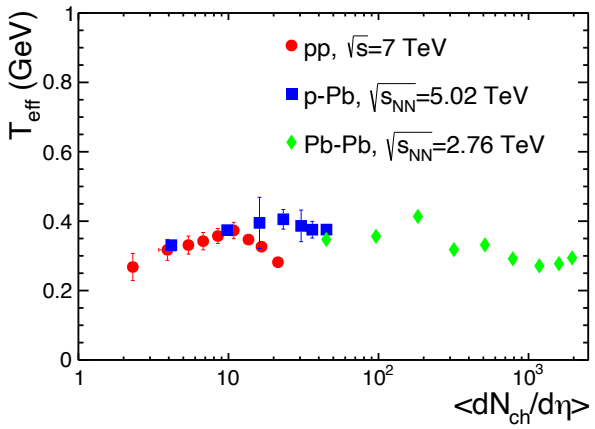

Figure 3.10: Effective temperature of ϕ mesons as a function of charged particle multiplicity for *pp* collision at $\sqrt{s} = 7$ TeV, p–Pb collision at $\sqrt{s_{\rm NN}} = 5.02$ TeV and Pb–Pb collision at $\sqrt{s_{\rm NN}} = 2.76$ TeV [95].

Finally, the effective temperature of ϕ meson is depicted in figure 3.10 as a function of the charged particles multiplicity. It encodes both the temperature due to thermal motion ($T_{\rm th}$) and the temperature owing to the collective motion. $T_{\rm eff}$ does not depend significantly on $\langle dN_{\rm ch}/d\eta\rangle$ regardless of the collision systems and appears to be flat with respect to charged particle multiplicity. When

$\langle dN_{\rm ch}/d\eta \rangle$ is considered, this behaviour differs from the behaviour seen for $T_{\rm th}$. The trend of $T_{\rm eff}$ indicates that the location of the QGP phase boundary is independent of or minimally dependent on the multiplicity of charged particles since the ϕ meson preserves the information of the QGP phase boundary. $T_{\rm ch}$ was previously shown to be independent of final-state charged particle multiplicity, which is an interesting confirmation of our observation.

According to figures 3.8 and 3.9, the QGP phase exhibits a relatively mild dependency on charged-particle multiplicity, whereas the duration of the hadronic phase exhibits a substantial dependence on the charged-particle multiplicity. This shows that the temperature at which hadronization from a QGP state begins is the same regardless of the number of charged particles, the nature of the collision system, or the collision energy. In contrast, the length of the hadronic phase strongly depends on the number of charged particles in the final state.

Chapter 4

Measurement of ψ(2S) polarization in proton+proton collisions with ALICE

4.1 The Large Hadron Collider

The Large Hadron Collider (LHC) is the biggest man-made instrument ever built [109]. It is a particle accelerator made up of two rings which are installed in an underground tunnel with a circumference of 26.7 km across the Switzerland and France border. The LHC is designed to allow pp collisions up to $\sqrt{s} = 14$ TeV and Pb–Pb collisions up to $\sqrt{s_{\rm NN}} = 5.5$ TeV. For LHC Run 2, the luminosity for pp collisions is $\mathcal{L} = 10^{34}\ cm^{-2}s^{-1}$ and for heavy ion collision is $\mathcal{L} = 10^{27}\ cm^{-2}s^{-1}$. The LHC accelerates two counter-rotating particle beams circulating in two separate beam pipes, which can collide at eight different collision points. We briefly discuss four major experiments installed in four of the interaction points below.

A Toroidal LHC Apparatus (ATLAS) [110] is a general-purpose detector which has a large toroidal superconducting magnet. It was partly responsible for the discovery for the Higgs boson. This detector focuses on the physics beyond the standard model, supersymmetry, extra-dimension, etc. Compact Muon Solenoid (CMS) [111] is also a general-purpose detector built around a large solenoid magnet. The physics aim of CMS is almost the same as that of ATLAS. Large Hadron

Collider beauty (LHCb) [112] detector is situated in the forward rapidity region. This experiment focuses on detecting beauty particles for CP violation studies and rare decays. Finally, A Large Ion Collider Experiment (ALICE) is the fourth major experiment designed explicitly to study QGP through heavy-ion collisions.

The ongoing Run 3 has commenced data-taking with an increased luminosity, resulting in an anticipated increase in statistics by about two orders of magnitude for the ALICE experiment. This will allow for better measurement of heavy-flavour hadrons, quarkonia (heavy quark-anti-quark bound state), and low-mass dileptons at low transverse momenta, together with novel measurements of jets and their constituents and a significant improvement in vertexing and tracking efficiency at low transverse momentum etc.

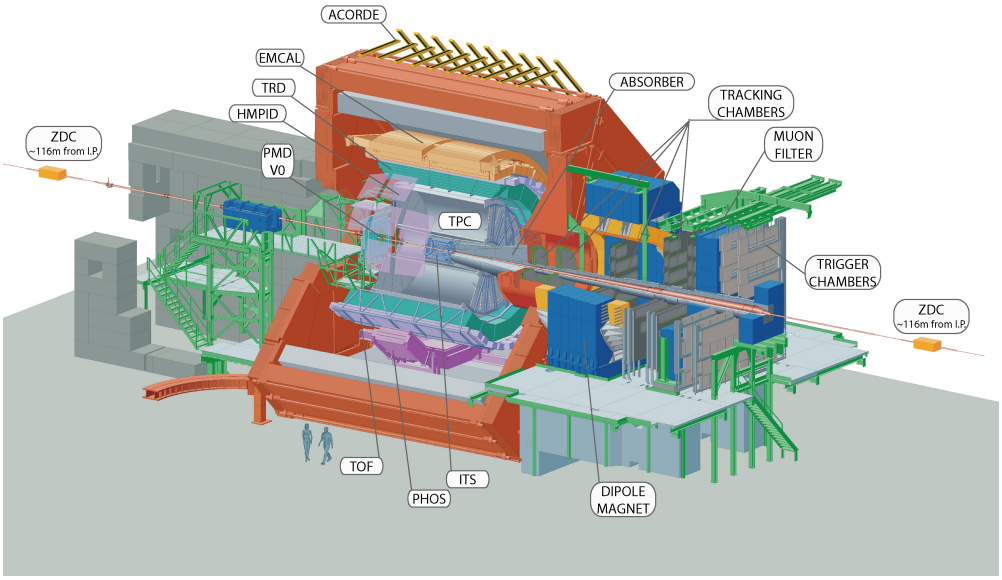

Figure 4.1: A schematic representation of the ALICE detector (Run 2 configuration).

4.2 The ALICE Experiment

The ALICE experiment [113] mainly concerns with the study of the strongly interacting hot and dense matter known as quark gluon plasma. It studies pp, p–Pb and Pb–Pb collisions and can detect photons, hadrons, electrons and muons. A schematic diagram of the ALICE experiment is shown in Fig. 4.1. The ALICE detector consists of two main parts: the central barrel detectors and the forward detectors. The central barrel detectors are put inside a solenoidal magnet with a magnetic field $B = 0.5$ T. These detectors are used for the identification of charged particles (ITS, TPC, TRD, TOF, HMPID) and photons (PHOS and EMCAL). The forward detectors (FMD, PMD, V0, T0 and ZDC) are used for luminosity measurement, triggering and event characterization. Moreover, the muon spectrometer is another important detector in the forward region responsible for muon tracking and triggering. Our study deals with the muon spectrometer, which is briefly discussed below.

4.2.1 Muon spectrometer

The muon spectrometer [114] of ALICE is mainly designed to measure the production of heavy quarkonia such as J/ψ, $\psi(2S)$, $\Upsilon(nS)$ and some low mass mesons such as ρ, ω and ϕ through their dimuon ($\mu^+\mu^-$) decay channel. It is also used to measure the production of muons from decays of heavy-flavor hadrons (D and B mesons) and the $W^{\pm}$ and Z^0 bosons. The muon spectrometer has angular acceptance between $171^\circ < \theta < 178^\circ$ corresponding to the pseudorapidity interval $-4 < \eta < -2.5$. The basic construction of the muon spectrometer is having an absorber to filter the background, a set of tracking chambers before, inside and after the magnet, followed by a set of trigger chambers. The objective of the front absorber is to stop the primary hadrons coming from the collisions. It is made of carbon, concrete, and steel with the task of filtering out hadrons by a factor of

100. The front absorber is the main contributor to the invariant mass resolution of the spectrometer.

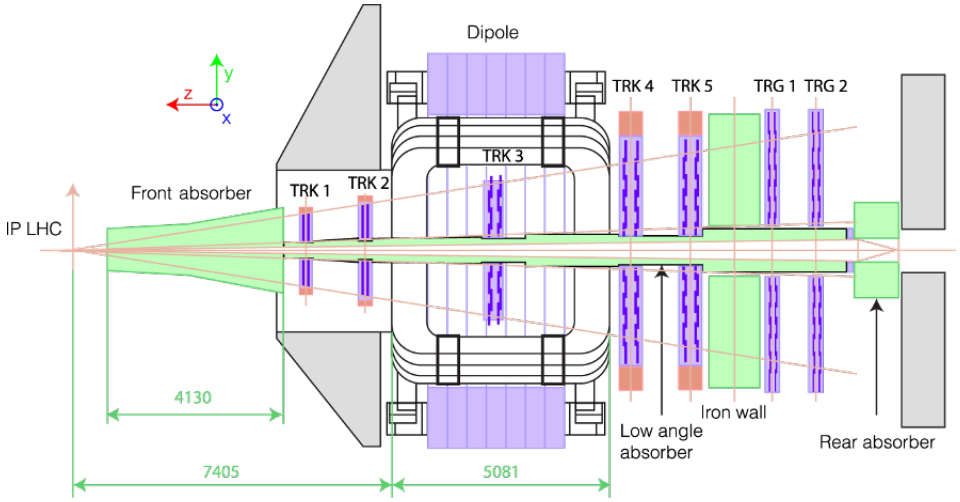

Figure 4.2: A schematic diagram of the muon spectrometer.

The Muon Tracking Chamber (MCH) is vital for reconstructing muon trajectories, comprising five stations, each equipped with two Cathode Pad Chambers. Precision is crucial, requiring spatial resolution better than 100 m in the bending plane to resolve bottomonium states while achieving 1 mm resolution in the non-bending plane. To minimize multiple scattering, chamber thickness is kept minimal, just a few percent of radiation length per plane. These Multi-Wire Proportional Chambers (MWPCs) use a gas mixture of 80% Ar and 20% CO_2, with cathode pads serving as readouts. As charged particles pass through the gas, they ionize it, leading to electron drift towards anode wires, creating secondary electron avalanches. This induces charge distributions on cathode pads, facilitating the determination of particle positions within the chamber.

The third station of the MCH is inside a dipole magnet, producing a 3 Tm integrated magnetic field. The next element is a hadronic interaction-length iron wall, followed by the muon trigger system consisting of two stations, each with two layers of resistive plate chambers. The trigger system has a momentum

resolution of 1%. In addition, there is a conical absorber made of tungsten, lead, and steel that surrounds the beam pipe at small polar angles (less than 2°) with the mission of shielding the spectrometer from secondary particles.

The trigger uses Muon tracks detected in the trigger stations and matched offline to the muon tracks reconstructed in the five tracking stations. The trigger system provides single muon and dimuon triggers for tracks above a programmable transverse-momentum threshold. The threshold can be set to 0.5 to 4 GeV/c as measured by the trigger stations. The efficiency for tracks measured with both the trigger and the tracking chambers increases with transverse momentum, which is approximately 50% at 1 GeV/c. In our analysis, we use the muon spectrometer to study the dimuon decay channel of charmonia, specifically ψ(2S).

4.3 Quarkonia Polarization

Heavy quarks (c, b) and their corresponding bound states, $J/\psi(c\bar{c})$, $\Upsilon(b\bar{b})$ are very crucial probes for QGP. These heavy quarks' bound states are called quarkonia, consisting of pairs of charm or bottom quarks. The heavy quarks are produced relatively early in the medium evolution through hard scatterings and can give us essential information about the deconfined medium. Thus, thoroughly studying the quarkonia production and other dynamics is necessary to understand the medium formed in both hadronic and heavy-ion collisions. However, despite significant experimental and theoretical works over the past few decades, the quarkonium production dynamics in hadron collisions are still not fully understood. Quantum chromodynamics predictions in the perturbative and nonperturbative regimes can be tested using measurements of heavy quarkonium production in the hadronic collisions. In the context of QCD, several theoretical models have been developed to clarify the quarkonium production cross-section and polarization as functions of the quarkonium transverse momentum, p_{T}, but none of them can explain both of

them simultaneously. The nonrelativistic quantum chromodynamics (NRQCD) model successfully explains the J/ψ production and its transverse momentum spectra [115]. In the NRQCD, purely perturbative color-singlet production is supplemented by potential nonperturbative transitions from colored quark pairs to the observable bound states. However, it does not adequately explain the polarization of J/ψ mesons [21]. According to NRQCD predictions, the polarization of the S-wave quarkonia directly created at high transverse momentum will be transverse about the direction of their own momentum. But the CDF Collaboration recorded almost no transverse J/ψ polarization, yet a slight longitudinal polarization at high p_{T} [116]. Similarly, the results from the ALICE and CMS collaborations also show almost zero polarization at both low and high p_{T} [18, 117]. This is called the J/ψ polarization puzzle. Thus, some new and improved theories were sought after, namely the CGC+NRQCD approach [118] and the improved color evaporation model (ICEM) where k_T factorization has been considered [119]. However, it is necessary to study the charmonia polarization at a higher centre of mass energies to have a conclusive idea from the perspective of experimental data.

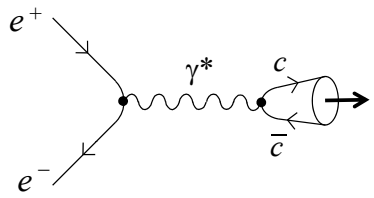

Figure 4.3: Charmoina production through electron-positron annihilation.

In general, spin-polarization is defined as the alignment of the spin of a particle in a given direction. The NRQCD predicts that the initial gluon polarization may be carried to the charm-anticharm pair through their initial hard scatterings, and as the $c\bar{c}$ pair evolves into charmonium, the polarization may be preserved as the

charmonia polarization. In the two-body decay of charmonia, the spin alignment will be reflected in the angular distribution of the decay particles. There are various processes through which the $c\bar{c}$ pair may get polarized. Vector quarkonia ($J^{PC} = 1^{--}$) have the same charge-parity as an electron-positron pair and can be produced from the annihilation of electron-positron pairs with photon as the intermediate particle. The $c\bar{c}$ originating from this process may be polarized due to helicity conservation. The helicity operator, $h = \mathbf{S}.\mathbf{p}/|\mathbf{p}|$ corresponds to the spin projection on the momentum direction. Helicity conservation is a general property of both QED and QCD in the relativistic or massless limits. In the case of massless fermions, their momenta cannot be reversed by Lorentz transformation, and the left-handed and right-handed chiral components become eigenstates of the helicity operator. Thus, chirality conservation becomes helicity conservation. Fig 4.3 suggests that as the intermediate photon has zero helicity, thus the annihilating electron-positron must have opposite helicity due to helicity conservation. In the lab frame, their momenta are opposite; thus, their spin must be parallel. Due to angular momentum conservation, the produced charmonium, therefore, has the third angular momentum component $J_z = \pm 1$ (as J = S + L, assuming L to be zero for the ground state and as the spins of the charm anti-charm are parallel). This means that the charmonia is polarized. As the dilepton system coupled to an intermediate photon is a pure $J_z = \pm 1$ state, this becomes an essential characteristic of the dilepton-decay angular distributions of charmonia or any vector quarkonia.

Similarly, the quark helicity is conserved in QCD in the massless limit. Thus, the charmonia originating from the quark anti-quark annihilation with an intermediate gluon, as shown in Fig. 4.4, will tend to have their angular momentum aligned ($J_z = \pm 1$) along the beam direction, provided they are produced alone. This prediction is in good agreement with the χ_c^1, χ_c^2, J/ψ and $\psi(2S)$ polarization measurement in low energy $p\bar{p}$ collisions [120–122].

Nevertheless, at very high p_T, the quarkonium production in hadronic colli-

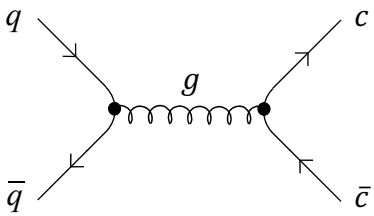

Figure 4.4: Charmoina production from quark anti-quark annihilation.

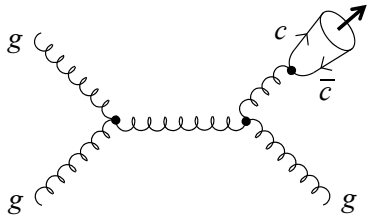

Figure 4.5: Charmoina production through gluon fragmentation.

sions should be dominated by gluon fragmentation processes, as shown in Fig. 4.5. NRQCD predicts that the J/ψ and $\psi(2S)$ production at high p_T is dominated by gluon fragmentation into the color octet $c\bar{c}[^3S_1^{(8)}]$. The creation of other allowed color and angular momentum configurations containing the $c\bar{c}$ pair are suppressed with increasing p_T. The fragmenting gluon is on-shell and has helicity ± 1. Thus, the observed charmonia has the angular momentum component $J_z = \pm 1$ in its own momentum direction.

In other frameworks, such as the Color Evaporation Model (CEM), the $c\bar{c}$ is produced in any color and angular momentum configuration. Contrary to NRQCD, there are no hierarchy constraints imposed on these configurations, resulting in dominated production of $c\bar{c}$ pairs with vanishing angular momentum in either color-singlet or color-octet states. Thus, in this model, there is no preferred alignment of angular momentum. To have a concrete understanding of

the quarkonium production dynamics and their polarization, it is essential to have a thorough study of polarization in the experiment, as there are contradictory theories present.

The quarkonia have different excited states, such as J/ψ being the S-wave quarkonia has ψ(2S) and χ_c. Similarly, $\Upsilon(1S)$ has $\Upsilon(2S)$ and $\Upsilon(3S)$ states. These higher-state particles have relatively higher masses and are produced in lesser numbers than their 1S partners. In *pp* collisions, charmed quarkonia can be created in three ways: directly by hard scattering, through feed-down from higher-mass charmonia states, or by the decay of b-hadrons. The first two of these methods are referred to as prompt production. A small prompt J/ψ polarization can be interpreted as reflecting a mixture of directly produced mesons with those produced in the decays of heavier charmonium states. However, the contribution from feed-down is minimal for ψ(2S) mesons, allowing a simple comparison between observations of prompt production and predictions for direct contributions. Thus, we choose ψ(2S) as our probe and study its polarization measurements.

In literature, ψ(2S) polarization measurement has been done in LHCb and CMS collaboration for *pp* collisions at $\sqrt{s}$ = 7 TeV [18, 20]. The results are consistent with zero within uncertainties, which don't agree with some theoretical expectations. However, going towards a higher centre of mass energy and higher statistics can better resolve the results. Thus, we study ψ(2S) polarization in *pp* collisions at $\sqrt{s}$ = 13 TeV for the first time in the ALICE experiment. ψ(2S) can be created in three angular momentum states related to their polarization state since they are vector mesons ($J^{PC} = 1^{--}$). One can obtain ψ(2S) polarization through the dilepton decay channel by examining the lepton angular distribution in the ψ(2S) rest frame.

4.3.1 Decay channels

There are three primary decay channels of J/ψ or ψ(2S) as given below;

$$J/\psi \rightarrow 3g$$
$$J/\psi \rightarrow \gamma + 2g$$
$$J/\psi \rightarrow \gamma^*.$$

The first decay mode concerns J/ψ decaying to π^+, π^0 and π^- with a branching fraction of 64.1 $\pm$ 1.0 %. However, this decay mode is strongly suppressed due to the OZI (Okubo-Zewig-Izuka) rule. The OZI rule states that a strong interaction will be suppressed if its Feynman diagram can be separated into two disconnected diagrams: one containing all of the initial-state particles and one containing all of the final-state particles, through only the removal of internal gluon lines. For the channels where only internal gluon lines are present, the gluons must have high momentum to produce at least the rest of the mass of the quarks. High momentum transfer results in a decrease in the coupling constant of the gluons. Thus, the process gets OZI suppressed.

The second decay mode has a branching fraction of 8.8 $\pm$ 1.1 %; however, the reconstruction of J/ψ from this channel has large background signals. The third mode concerns J/ψ decaying to γ^*, which further decays to particle-antiparticle pairs or the electromagnetic decay mode. There are three electromagnetic decay channels; the first one decays to hadrons, the other two are $J/\psi \rightarrow e^+e^-$ with branching ratio 5.971 $\pm$ 0.032 % and $J/\psi \rightarrow \mu^+\mu^-$ with branching ratio 5.961 $\pm$ 0.033 %. The hadronic channel is J/ψ decaying to D^+ and D^- mesons. However, this decay mode is kinematically suppressed due to the heavy masses of D-meson. The leptonic decay channels can be used to study the polarization of J/ψ. In the context of the ALICE experiment, the $J/\psi \rightarrow e^+e^-$ decay can be studied with the central barrel detectors, while the $J/\psi \rightarrow \mu^+\mu^-$ can be studied with the forward muon spectrometer. As the e^+e^- signal will be contaminated by various

other electromagnetic decays, there will be a significant background in the signal. On the other hand, the $\mu^+\mu^-$ signal will be cleaner in comparison and can be efficiently studied with the muon spectrometer in the ALICE detector. Thus, in our study we take the decay channel J/ψ (ψ(2S)) $\rightarrow \mu^+\mu^-$.

4.3.2 Angular distribution

The polarization of the parent quarkonium state is reflected in the geometrical shape of the angular distribution of the dileptons in the quarkonium two-body decay ($Q\bar{Q} \rightarrow l^+l^-$). The quarkonium would be considered unpolarized on the average if the distribution is spherically symmetric. On the other hand, polarized quarkonia states are indicated by an anisotropic dilepton distribution. In this section, we describe an experimental method for monitoring the angular distribution of dilepton decay to determine the spin alignment of a vector quarkonium. Although the ψ(2S) is mentioned explicitly as the decaying particle for convenience, the concepts and findings apply to any $J^{PC} = 1^{--}$ state.

The ψ(2S) is formed as a superposition of its three $J = 1$ eigenstates, $J_z = +1, -1, 0$ with respect to the polarization axis z [107]:

$$|\psi(2S)\rangle = b_{+1}\,|+1\rangle + b_{-1}\,|-1\rangle + b_0\,|0\rangle\,. \tag{4.1}$$

The calculations are carried out in the ψ(2S) rest frame, where the reference axis $z^{'}$ is usually orientated in the direction of the positive lepton and is defined by the common direction of the two leptons. The dilepton system coupled to a photon in the process $\psi(2S) \rightarrow \gamma^* \rightarrow \ell^+\ell^-$ has an angular momentum projection ±1 along z', meaning that it can be represented as an eigenstate of $J_{z'}$, $|\ell^+\ell^-; 1, l'\rangle$ with $l' = +1$ or -1. This is because helicity conservation for (massless) fermions in QED holds true. This state is to be expressed as a superposition of J_z, $|\ell^+\ell^-; 1, l\rangle$ eigenstates, where $l = 0, \pm1$. $R(\alpha, \beta, \gamma)$ indicates the rotation from a set of axes (x, y, z) to the other set (x', y', z'), α, β and γ denoting the Euler

angles. The right-hand rule defines positive rotations. The rotation transformation can thus be used to express an eigenstate $|J, M'\rangle$ of $J_{z'}$ as a superposition of the eigenstates $|J, M\rangle$ of J_z.

$$|J, M'\rangle = \sum_{M=-J}^{+J} \mathcal{D}^J_{MM'}(R)\,|J, M\rangle\,. \tag{4.2}$$

The rotation matrix elements $\mathcal{D}^J_{MM'}$ are defined as,

$$\mathcal{D}^J_{MM'}(\alpha, \beta, \gamma) = e^{-iM\alpha} d^J_{MM'}(\beta) e^{-iM'\gamma} \tag{4.3}$$

in terms of the reduced matrix elements,

$$\begin{aligned} d^J_{MM'}(\beta) = & \sum_{t=\max(0,M-M')}^{\min(J+M,J-M')} (-1)^t \\ & \times \frac{\sqrt{(J+M)!\,(J-M)!\,(J+M')!\,(J-M')!}}{(J+M-t)!\,(J-M'-t)!\,t!\,(t-M+M')!} \\ & \times \left(\cos\frac{\beta}{2}\right)^{2J+M-M'-2t} \left(\sin\frac{\beta}{2}\right)^{2t-M+M'}. \end{aligned} \tag{4.4}$$

The rotation aligns two quantization axes (z and z') in this case. The parameters $\beta = \vartheta$ and $\alpha = -\gamma = \varphi$ can be used to parametrize the most generic rotation that performs this projection. Thus, in terms of eigenstates of J_z, the dilepton angular momentum state is given as,

$$|\ell^+\ell^-; 1, l'\rangle = \sum_{l=0,\pm1} \mathcal{D}^1_{ll'}(\varphi, \vartheta, -\varphi)\,|\ell^+\ell^-; 1, l\rangle\,. \tag{4.5}$$

The amplitude of the partial process $\psi(2\mathrm{S})(m) \to \ell^+\ell^-(l')$ is given by,

$$\begin{aligned} B_{ml'} &= \sum_{l=0,\pm1} \mathcal{D}^{1*}_{ll'}(\varphi, \vartheta, -\varphi)\,\langle \ell^+\ell^-; 1, l\,|\,\mathcal{B}\,|\,\psi(2S); 1, m\rangle \\ &= B\,\mathcal{D}^{1*}_{ml'}(\varphi, \vartheta, -\varphi)\,, \end{aligned} \tag{4.6}$$

where the transition operator $\mathcal{B}$ is of the form $\langle \ell^+\ell^-; 1, l\ |\mathcal{B}|\ \psi(2S); 1, m\rangle = B\,\delta_{m\,l}$ because of angular momentum conservation, with B independent of m (for

rotational invariance). The total amplitude for $\psi(2S) \to \ell^+\ell^-(l')$ where $\psi(2S)$ is given by the superposition mentioned in Eq. 4.1 is given by,

$$\begin{aligned} B_{l'} &= \sum_{m=-1,+1} b_m B\, \mathcal{D}^{1*}_{ml'}(\varphi,\vartheta,-\varphi) \\ &= \sum_{m=-1,+1} a_m\, \mathcal{D}^{1*}_{ml'}(\varphi,\vartheta,-\varphi)\,. \end{aligned} \tag{4.7}$$

By squaring Eq. 4.7 and adding up the (unobserved) spin alignments ($l' = \pm 1$) of the dilepton a system, equal weights are assigned to the two configurations to preserve parity. This yields the probability of the transition. The angular distribution may be obtained by applying Eq. 4.3, where $d^1_{0,\pm1} = \pm\sin\vartheta/\sqrt{2}$, $d^1_{\pm1,\pm1} = (1+\cos\vartheta)/2$, and $d^1_{\pm1,\mp1} = (1-\cos\vartheta)/2$ [107].

$$\begin{aligned} W(\cos\vartheta,\varphi) \quad &\propto \sum_{l'=\pm1} |B_{l'}|^2 \;\propto\; \frac{\mathcal{N}}{(3+\lambda_\vartheta)}\,(1 + \lambda_\vartheta \cos^2\vartheta \\ &+ \lambda_\varphi \sin^2\vartheta\cos 2\varphi \;+\; \lambda_{\vartheta\varphi}\sin 2\vartheta\cos\varphi \\ &+ \lambda^\perp_\varphi \sin^2\vartheta\sin 2\varphi \;+\; \lambda^\perp_{\vartheta\varphi}\sin 2\vartheta\sin\varphi)\,, \end{aligned} \tag{4.8}$$

with $\mathcal{N} = |a_0|^2 + |a_{+1}|^2 + |a_{-1}|^2$ and

$$\begin{aligned} \lambda_\vartheta &= \frac{\mathcal{N} - 3|a_0|^2}{\mathcal{N} + |a_0|^2}\,, \\ \lambda_\varphi &= \frac{2\,\mathrm{Re}[a^{(i)*}_{+1} a_{-1}]}{\mathcal{N} + |a_0|^2}\,, \\ \lambda_{\vartheta\varphi} &= \frac{\sqrt{2}\,\mathrm{Re}[a^{(i)*}_0 (a_{+1} - a_{-1})]}{\mathcal{N} + |a_0|^2}\,, \\ \lambda^\perp_\varphi &= \frac{-2\,\mathrm{Im}[a^*_{+1} a_{-1}]}{\mathcal{N} + |a_0|^2}\,, \\ \lambda^\perp_{\vartheta\varphi} &= \frac{-\sqrt{2}\,\mathrm{Im}[a^*_0 (a_{+1} + a_{-1})]}{\mathcal{N} + |a_0|^2}\,. \end{aligned} \tag{4.9}$$

It is important to note that all of the decay parameters in Eq. 4.8 vanish because it is impossible to select the decay amplitudes a_m and, consequently, the

component amplitudes b_m. This implies that a $J = 1$ state's decay has an angular distribution that is never genuinely isotropic. It is possible that a fortuitous cancellation of all decay parameters could result from a lucky superposition of different production processes. However, such an exceptional case would indicate a non-trivial physical polarisation scenario caused by spin randomization effects or (semi-)exclusive configurations in which certain final state objects are produced along with the observed state. To put it another way, polarization is a necessary characteristic of the quarkonium states. It is worth noting that all current Monte Carlo generators assume an isotropic dilepton distribution by default for quarkonium production in hadronic collisions. This is a significant assumption that affects acceptance estimates and, consequently, the normalisations and kinematic dependencies of the measured quarkonium cross-sections.

We exclusively focus on inclusive production, where the experimental definition of the xz plane aligns with the production plane, encompassing the trajectories of the colliding particles and the decaying particle itself. The last two terms in Eq. 4.8 introduce an asymmetry in the distribution through reflection across the production plane, a characteristic not prohibited in individual (parity-conserving) events. In hadronic collisions, owing to intrinsic parton transverse momenta, the polarization plane does not consistently align, on a per-event basis, with the experimental production plane. Nonetheless, the symmetry by reflection must manifest in the observed event distribution when only parity-conserving processes contribute. Specifically, terms such as $\sin^2\vartheta \sin 2\varphi$ and $\sin 2\vartheta \sin\varphi$ remain unobservable due to their vanishing average.

So, the polarization of the ψ(2S) can be measured through the study of the angular distribution of the leptons produced in the $\psi(2S) \to \mu^+ \mu^-$ decay [107]:

$$W(cos\theta, \phi) \propto \frac{1}{3+\lambda_\theta}(1 + \lambda_\theta \, cos^2\theta + \lambda_\phi \, sin^2\theta \, cos2\phi + \lambda_{\theta\phi} \, sin2\theta \, cos\phi) \quad (4.10)$$

where λ_θ, λ_ϕ and $\lambda_{\theta\phi}$ are the ψ(2S) polarization parameters. The combinations

of these parameters can give us information about the polarization of the particle; the values of (λ_θ, λ_ϕ, $\lambda_{\theta\phi}$) = (0,0,0) means there is no polarization, (-1,0,0) suggests pure longitudinal polarization and (+1,0,0) suggests pure transverse polarization.

Alternatively, one can also take a one-dimensional approach and fit the angular distributions integrated over $cos\theta$ and ϕ, such that the distribution function becomes;

$$W(cos\theta|\lambda_\theta) \propto \frac{1}{3+\lambda_\theta}(1+\lambda_\theta\ cos^2\theta) \tag{4.11}$$

$$W(\phi|\lambda_\theta,\lambda_\phi) \propto 1+\frac{2\lambda_\phi}{3+\lambda_\theta}cos2\phi \tag{4.12}$$

$$W(\widetilde{\phi}|\lambda_\theta,\lambda_{\theta\phi}) \propto 1+\frac{\sqrt{2}\lambda_{\theta\phi}}{3+\lambda_\theta}cos\tilde{\phi} \tag{4.13}$$

The variable $\widetilde{\phi}$ is built to estimate $\lambda_{\theta\phi}$ and can be defined as;

$$\tilde{\phi} = \phi - \frac{3}{4}\pi, (cos\theta < 0)$$

$$\tilde{\phi} = \phi - \frac{1}{4}\pi, (cos\theta > 0)$$

4.3.3 Frames of reference

To measure the polarization of quarkonia, one needs to move from the center of mass frame to the quarkonia rest frame. In literature, there are various reference frames one can construct depending on the choice of the quantization axis (z - axis). In the helicity (HE) frame, the momentum direction of the quarkonia is taken as the quantization axis. In the Collin-Soper (CS) frame, the quantization axis is the bisector of the angle between the colliding beams, whereas the Gottfried-Jackson frame chooses one of the beam's momentum directions as the quantization axis. A schematic representation of the various frames has been shown in Fig. 4.6. Although there are several choices, it is necessary to consider

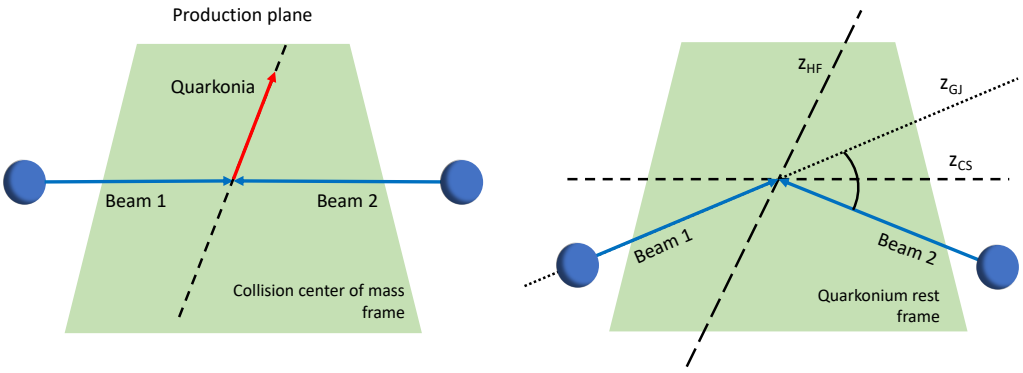

Figure 4.6: Schematic representation of three different definitions of the polarization axis, z, the helicity (HE), Collins-Soper (CS), Gottfried-Jackson (GJ) reference frames, with respect to the direction of motion of the colliding beams (Beam 1 and Beam 2) and the Quarkonia [108].

at least two different frames of reference while studying polarization to exclude any frame-dependent biases. In our analysis, we have chosen the HE and the CS frames and studied the quarkonia polarization.

4.4 Data sample and event selection

In the Muon Spectrometer, the triggered events are reconstructed using the raw information from the detector, represented by the particle hits crossing the tracking chambers. The dataset considered in this analysis corresponds to the data samples collected from 2016 to 2018 for pp collisions at $\sqrt{s} = 13$ TeV. The run list which has been used for data analysis is obtained according to a series of selection steps: during the data taking, the run has to be labelled as a "good run" by the data acquisition expert. The run has to satisfy specific quality requirements (quality assurance or QA) related to the efficiency and stability of the muon trigger chambers, the number of tracks per muon trigger, etc. The full run list used in the analysis can be found in [123]. The $A \times \varepsilon$ correction, as well as the

extraction of the tail parameters of the signal extraction functions, are produced with the LHC23e7 sample, which is anchored to all runs from Run 2 data-taking periods that we have used.

4.4.0.1 Event selection

The sample of dimuons is obtained by combining the muon pairs reconstructed in the Muon Spectrometer acceptance, applying a series of cuts at the single track level. The events used in this analysis have fired the CMUL7-B-NOPF-MUFAST (CMUL7) trigger, which is given by the logical AND of the V0A, V0C and unlike-sign low-p_{T} dimuon trigger inputs. Moreover, the selected events are required to pass the physics selection criteria. The total number of the CMUL7 events after the event selection used in this analysis is around 522 million.

4.4.0.2 (Di)muon track selection

In this analysis, ψ(2S) is studied via the dimuon decay channel. The single muon track candidates are selected with respect to the following criteria:

- 17.6 cm $< \mathrm{R_{abs}} <$ 89.5 cm to remove contamination by tracks crossing the thicker part of the absorber ($\mathrm{R_{abs}}$ = radial coordinate of the muon candidate at the end of the absorber)
- Reconstructed track matching a trigger track with $p_{\mathrm{T}}^{\mu} > 0.5$ GeV/c
- pDCA cut is applied (product of the muon total momentum (p) and its Distance of Closest Approach (DCA) within 6σ of the distribution). This cut is performed because, in this way, its distribution is approximately independent of the muon track momentum.
- Track within the acceptance of the spectrometer $-4 < \eta_{\mu} < -2.5$

  In addition, the dimuon pairs formed with the selected tracks satisfying every selection criteria must also fulfil the following requirements:

- Total charge of the pair = 0
- Dimuon pair within the acceptance of the spectrometer $2.5 < y_{\mu^+\mu^-} < 4$

4.4.1 Signal Extraction

The number of ψ(2S) signals as a function of the angular variables is measured to obtain the polarization parameters by fitting the invariant mass distribution. The continuum background and the signal must be characterized by the function that fits the invariant mass spectrum.

1. The signal of the J/ψ and ψ(2S) are fitted with the double Crystal Ball function (DCB), each for both states. We also fit the NA60 function (see appendix 6.2.3) to the signals to estimate systematic uncertainties.
2. The background is fitted with a variable width Gaussian function (VGW). One can also use the double exponential function for the background fitting.
3. The fitting range is taken to be 2.0–5.0 GeV/c.
4. The tail parameters cannot be left free in the fit due to the complexity of the signal created by combining two DCB functions with a significant number of parameters and restricted statistics. That results in a non-physical shape for the extended tails and a systematic overestimation of the tail component. A tail at low and high invariant mass results from muon multiple scattering, energy loss fluctuations in the front absorber, and misalignment of the tracking chambers. We fix the tail parameters from the corresponding MC spectra fits.
5. The mass and width of ψ(2S) is fixed to that of J/ψ and the rest of the parameters are kept free.

The double Crystal Ball function is given below.

$$f(x;N,\alpha_L,n_L,\alpha_R,n_R,\mu,\sigma) = \begin{cases} A(B-\frac{x-\mu}{\sigma})^{-n_L} & \text{if } \frac{x-\mu}{\sigma} \leq \alpha_L \\ C(D+\frac{x-\mu}{\sigma})^{-n_R} & \text{if } \frac{x-\mu}{\sigma} \geq \alpha_R \\ e^{-\frac{(x-\mu)^2}{2\sigma^2}} & \text{if } \alpha_L < \frac{x-\mu}{\sigma} < \alpha_R \end{cases}$$

$$\text{Here, } A = \left(\frac{n_L}{|\alpha_L|}\right)^{n_L} exp\left(-\frac{|\alpha_L^2|}{2}\right)$$

$$B = \frac{n_L}{|\alpha_L|} - |\alpha_L|$$

$$C = \left(\frac{n_R}{|\alpha_r|}\right)^{n_R} exp\left(-\frac{|\alpha_R^2|}{2}\right)$$

$$D = \frac{n_R}{|\alpha_R|} - |\alpha_R|$$

The variable width Gaussian function is given as;

$$f_{bkg}(x;N,\alpha,\beta,\gamma) = N_B\ exp\left[-\frac{1}{2}\left(\frac{x-\mu}{\sigma}\right)^2\right],\ \text{with } \sigma = \beta + \gamma\frac{x-\alpha}{\alpha}.$$

Firstly, in Fig. 4.7, we have shown the J/ψ and ψ(2S) MC spectra fitted with the DCB function. From the fit to the J/ψ MC spectra, we extract the tail parameters, which we then fix in our dimuon invariant mass fitting. From the fit to the ψ(2S) MC spectra, we can estimate the acceptance times efficiency, which will help us to estimate the corrected ψ(2S) number.

The p_{T} and angular variables integrated dimuon invariant mass spectra are shown in Fig. 4.8. As discussed above, we first fit the MC simulated data with

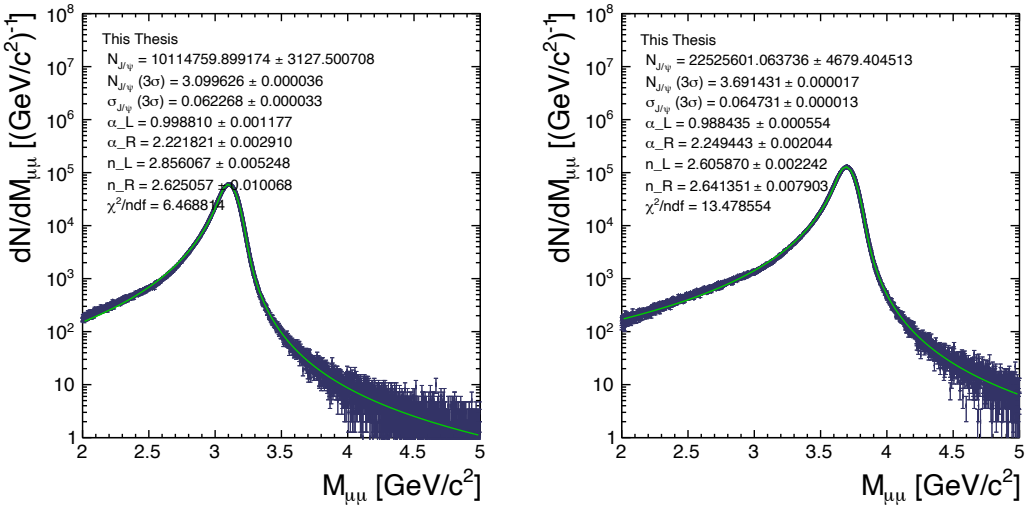

Figure 4.7: The J/ψ (left panel) and ψ(2S) (right panel) MC spectra, the signal is fitted with the double Crystal Ball function (the green line) [123].

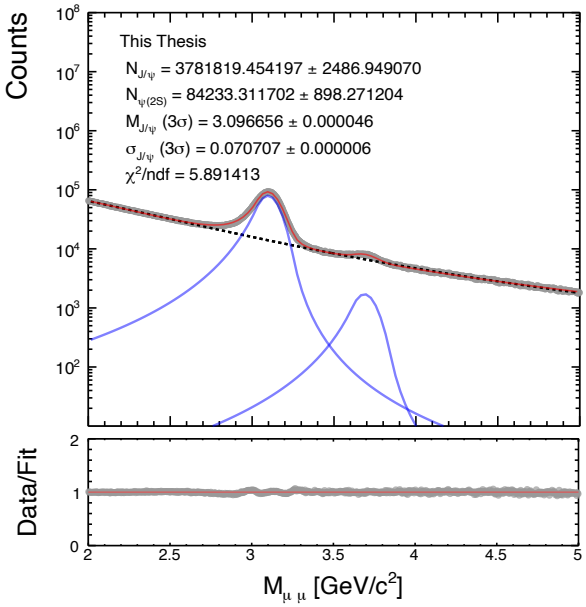

Figure 4.8: The dimuon invariant mass spectra, the signal is fitted with the double Crystal Ball function and the background is fitted with the variable width Gaussian function [123]. The lower panel shows the data by fit ratio.

the DCB function to obtain the tail parameters. We then fix the tail parameters for the signals while keeping the mass and width of J/ψ free. The mass and width of ψ(2S) are fixed to that of J/ψ as follows.

$$m_{\psi(2S)} = m^{FIT}_{J/\psi} + (m^{PDG}_{\psi(2S)} - m^{PDG}_{J/\psi})$$

$$\sigma_{\psi(2S)} = \sigma^{FIT}_{J/\psi} \times \frac{\sigma^{MC}_{\psi(2S)}}{\sigma^{MC}_{J/\psi}}$$

Here, $m^{FIT}_{J/\psi}$ and $\sigma^{FIT}_{J/\psi}$ are the mass and width of J/ψ obtained from the fit to the invariant mass spectrum. $m^{PDG}_{J/\psi} = 3.096$ GeV/c^2 and $m^{PDG}_{\psi(2S)} = 3.686$ GeV/c^2 are the masses of J/ψ and $\psi(2S)$ from the particle data group (PDG). $\sigma^{MC}_{\psi(2S)}$ and $\sigma^{MC}_{J/\psi}$ are the widths of $\psi(2S)$ and J/ψ obtained from the MC simulations.

4.4.2 Yield extraction: p_{T} dependence

We then proceed to fit the invariant mass spectra for different p_{T} bins. We have chosen six bins for this purpose; p_{T} = 0–2, 2–4, 4–6, 6–8, 8–10 and 10–15 GeV/c. We follow the same formalism above; we fit the DCB function to the signal and the VWG function to the background. The tails are extracted and fixed from the MC simulations fits for each respective p_{T} bin as shown in Fig. 4.9. Because there is no background in MC, we only fit the signal function to it. Then, we fit the data shown in Fig. 4.10. All the fits converged, and we obtained the number of ψ(2S) by integrating the function within the 3σ range of the mean value and subtracting the background from it.

We follow the same fitting procedure by changing our signal and background functions. We have four combinations for two signals and two background functions: DCB+VWG, DCB+DoubExpo, NA60+VWG and NA60+DoubExpo. We then obtain the number of ψ(2S) from all these fits. Finally, we obtain the corrected number of ψ(2S), estimated by diving the raw number of ψ(2S) obtained from the fits with the acceptance $\times$ efficiency obtained from the MC simulation.

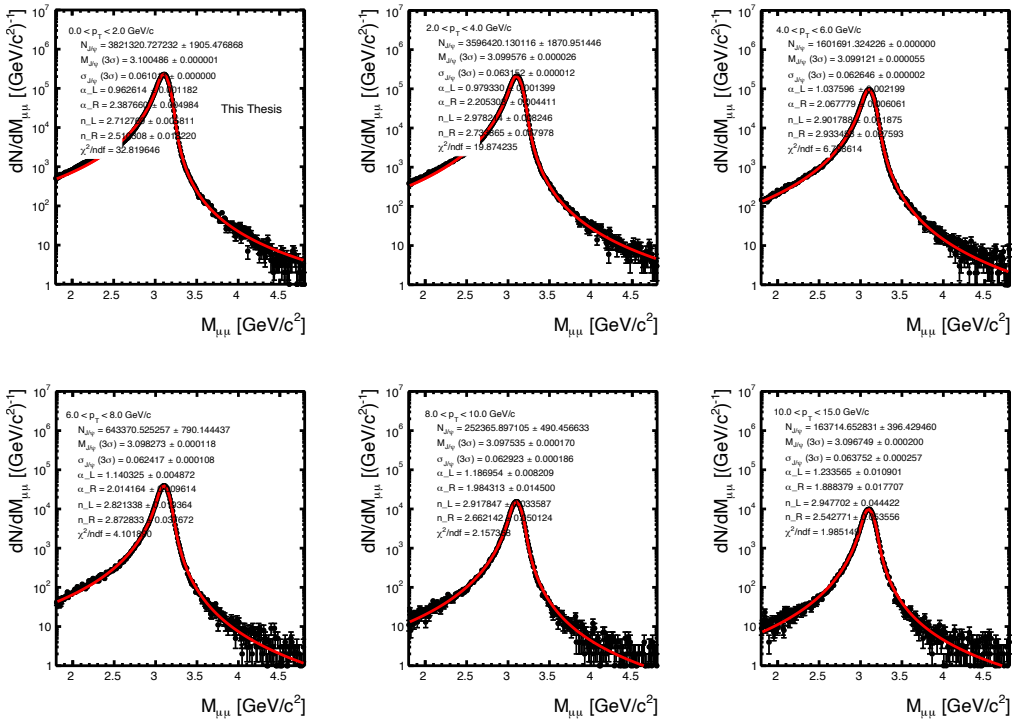

Figure 4.9: p_{T} differential MC invariant mass spectra of J/ψ fitted with the double Crystal Ball function [123].

The term acceptance times efficiency, denoted as $A \times \varepsilon$, represents the product of two factors: Acceptance, which reflects the geometrical coverage of the experimental setup and the kinematics of particle decay. Efficiency accounts for the performance of the detector and the effectiveness of the reconstruction algorithm. Specifically, in the ALICE muon spectrometer, it encompasses the contributions from trigger efficiency, tracking efficiency, and matching efficiency.

The MC simulation process is typically divided into three primary steps:

- Generation of the $\psi(2\mathrm{S})$ particle with specified transverse momentum (p_{T}) and rapidity (y), utilizing input distributions provided for simulation (input shapes). These distributions are directly calibrated against real data. Additionally, the degree of polarization can be adjusted, although it's typically

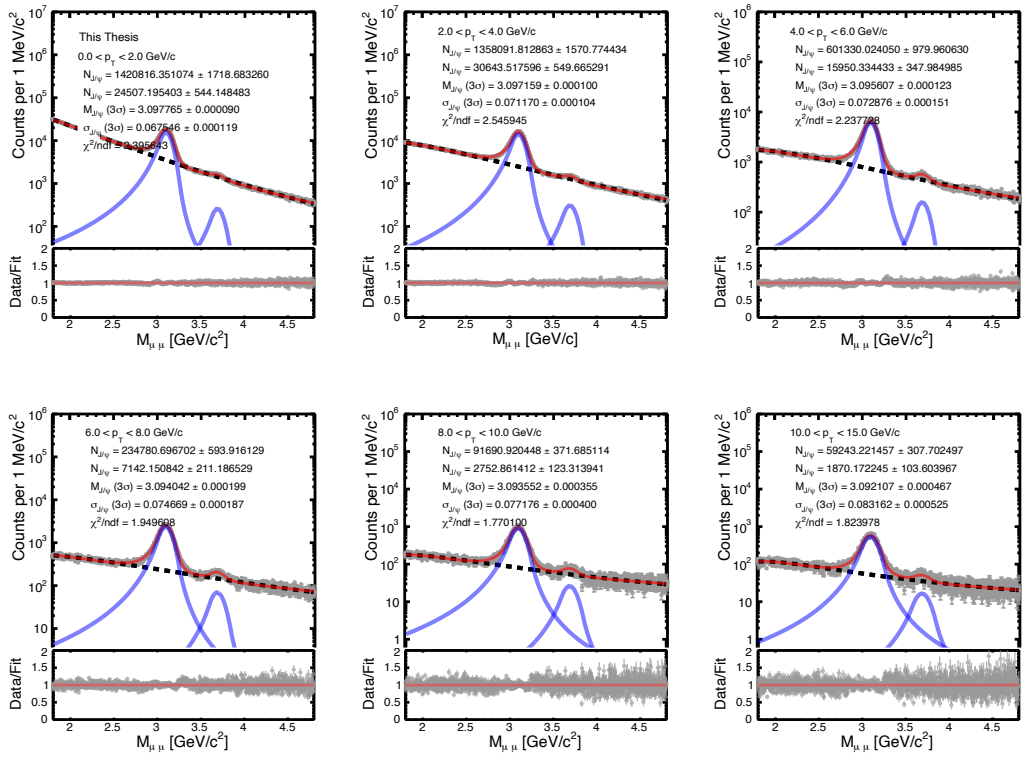

Figure 4.10: p_{T} differential invariant mass spectra of dimuons. The signal is fitted with the double Crystal Ball function, and the background is fitted with the variable width Gaussian function. The lower panels show the data by fit ratio [123].

set to zero in centralized Monte Carlo productions, which are employed in numerous analyses.

- The generated $\psi(2S)$ particle undergoes decay into a muon pair.
- The muon pair is then propagated within the experimental apparatus, and the digital responses of the detectors are recorded. Subsequently, based on this information, the muon tracks are reconstructed using the same algorithm employed for real data.

The output of the MC simulation includes both generated and reconstructed

events. The acceptance × efficiency can be estimated from the following formula;

$$A \times \varepsilon = \frac{N^{rec}_{\psi(2S)}}{N^{gen}_{\psi(2S)}},$$

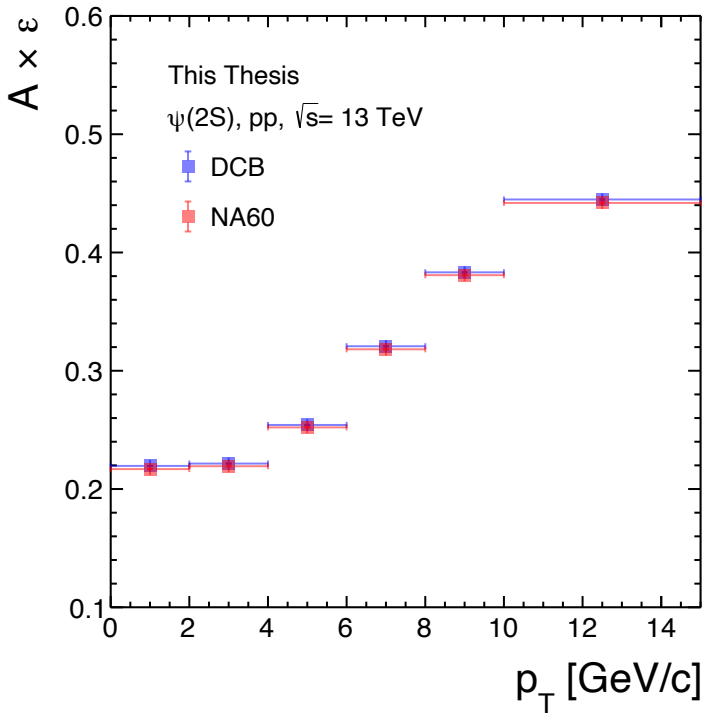

Figure 4.11: The acceptance times efficiency plot as a function of transverse momentum for ψ(2S) from fitting the DCB and NA60 function to the ψ(2S) MC spectra [123].

where $N^{rec}_{\psi(2S)}$ is the reconstructed ψ(2S) from the MC simulation after the implementation of detector information and applying proper kinematic cuts. On the other hand, $N^{gen}_{\psi(2S)}$ is the number generated ψ(2S), which is also called the true MC. Finally, one can get the corrected number of ψ(2S) by the following formula,

$$N^{corr}_{\psi(2S)} = \frac{N^{raw}_{\psi(2S)}}{A \times \varepsilon},$$

Fig. 4.11 shows the acceptance times efficiency of ψ(2S) as a function of p_{T} which has been extracted for two different cases, one by fitting the ψ(2S) MC

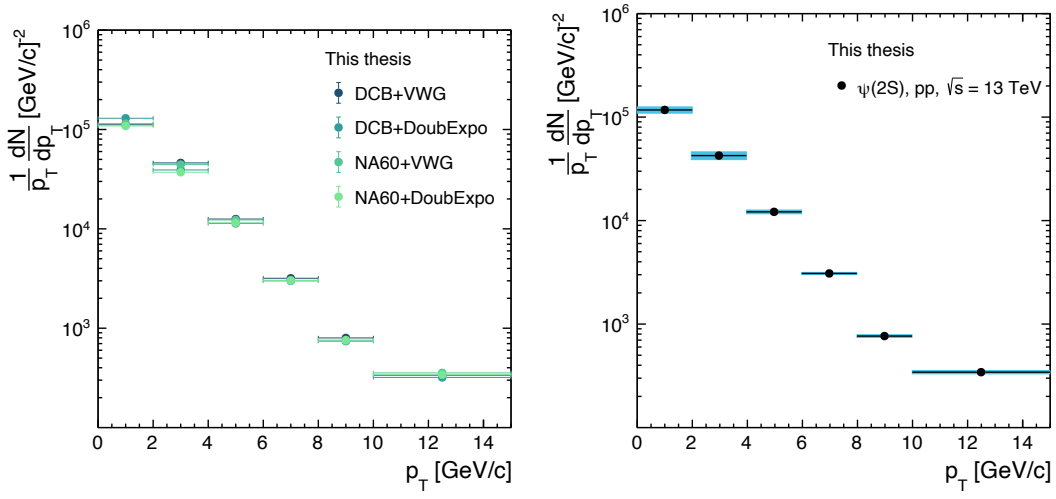

Figure 4.12: Corrected p_{T} spectra of ψ(2S) for various combinations of signal and background function (left panel) and with systematic uncertainties (right panel) [123].

spectra with the DCB function and the other by fitting the NA60 function. These will then help us to estimate the corrected number of ψ(2S) for their respective cases. In the left panel of Fig. 4.12, we have plotted the corrected ψ(2S) for different p_{T} bins divided with p_{T}. This gives us the unnormalized p_{T} spectra of ψ(2S) by using various combinations of signal and background functions. On the other hand, the right panel of Fig. 4.12 shows the corrected p_{T} spectra with systematic uncertainties originating from the choice of fitting functions.

4.4.3 Yield extraction: Angular dependence

In Fig. 4.13, we have plotted the dimuon distribution as a function of p_{T} (in the Y-axis) and angular variables (in the X-axis). For simplicity, we have only shown for the helicity frame. The distribution in the Collin-Soper frame can be seen in the appendix (see Fig. 6.7 and 6.8). We observe that in the *cosθ* distribution, the dimuons have not populated the low p_{T} and high *cosθ* region. Thus, we have

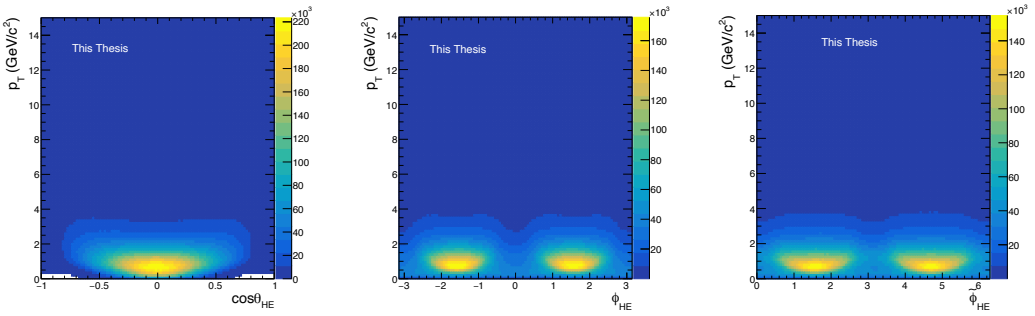

Figure 4.13: Dimuon distribution in the helicity frame as functions of transverse momentum vs $cos\theta$ (left panel), ϕ (middle panel) and $\tilde{\phi}$ (right panel) [123].

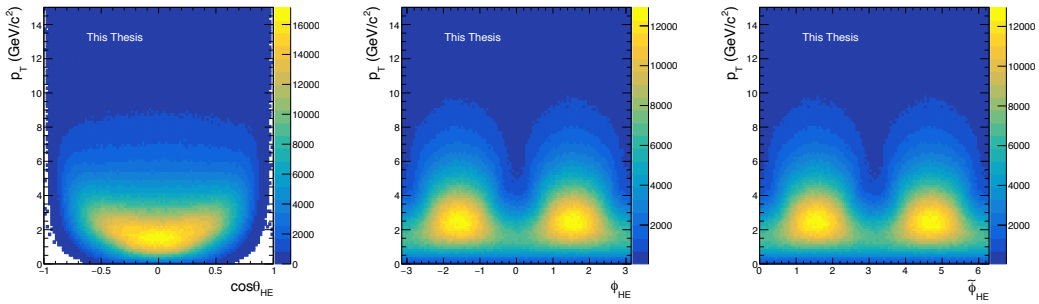

Figure 4.14: Acceptance × efficiency map of ψ(2S) for the helicity frame as functions of transverse momentum vs $cos\theta$ (left panel), ϕ (middle panel) and $\tilde{\phi}$ (right panel) [123].

neglected this area while extracting the raw number of ψ(2S). However, all three distributions show symmetry around a certain point. The same is true for the Collin-Soper frame also.

In Fig. 4.14, we have shown the acceptance × efficiency map of ψ(2S) obtained from the MC simulation in the HE frame. Here, we can see that in the $cos\theta$ distribution, the low p_{T} and higher $cos\theta$ bins are unpopulated, leading to a negligible $A \times \varepsilon$. Thus, we have to avoid these regions while doing the analysis. A similar observation can be made from the acceptance × efficiency map in the CS frame.

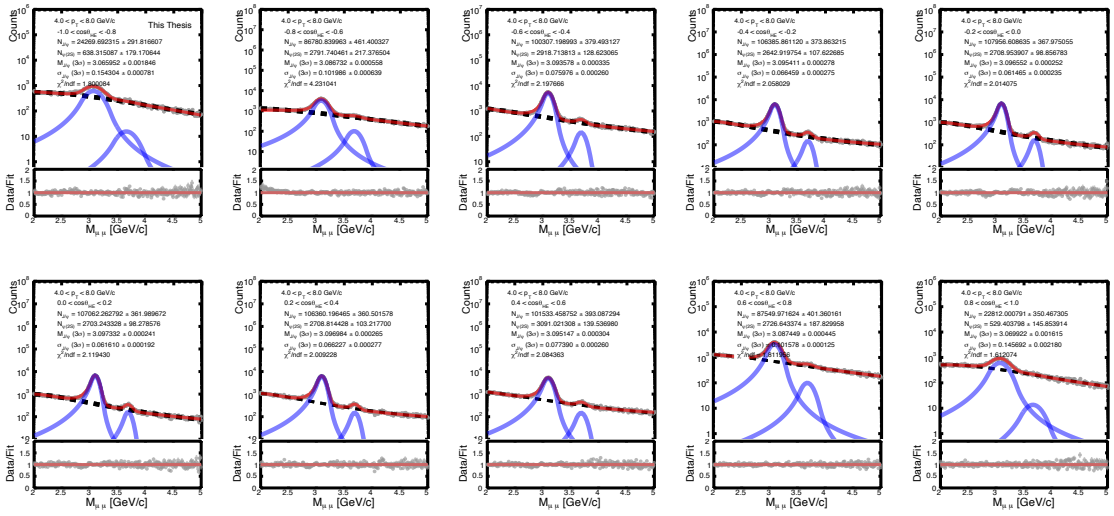

Figure 4.15: Double Crystal Ball + variable width Gaussian function fit to the invariant mass spectra for various $cos\theta$ ranges for $4.0 < p_{\mathrm{T}} < 8.0$ GeV/c in the helicity frame [123].

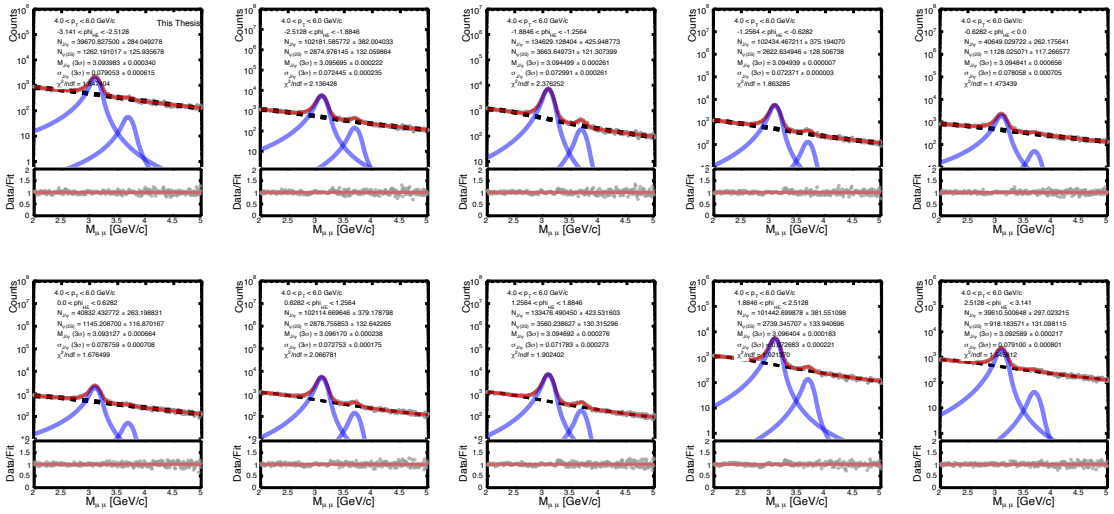

Figure 4.16: Double Crystal Ball + variable width Gaussian function fit to the invariant mass spectra for various ϕ ranges for $4.0 < p_{\mathrm{T}} < 8.0$ GeV/c in the helicity frame [123].

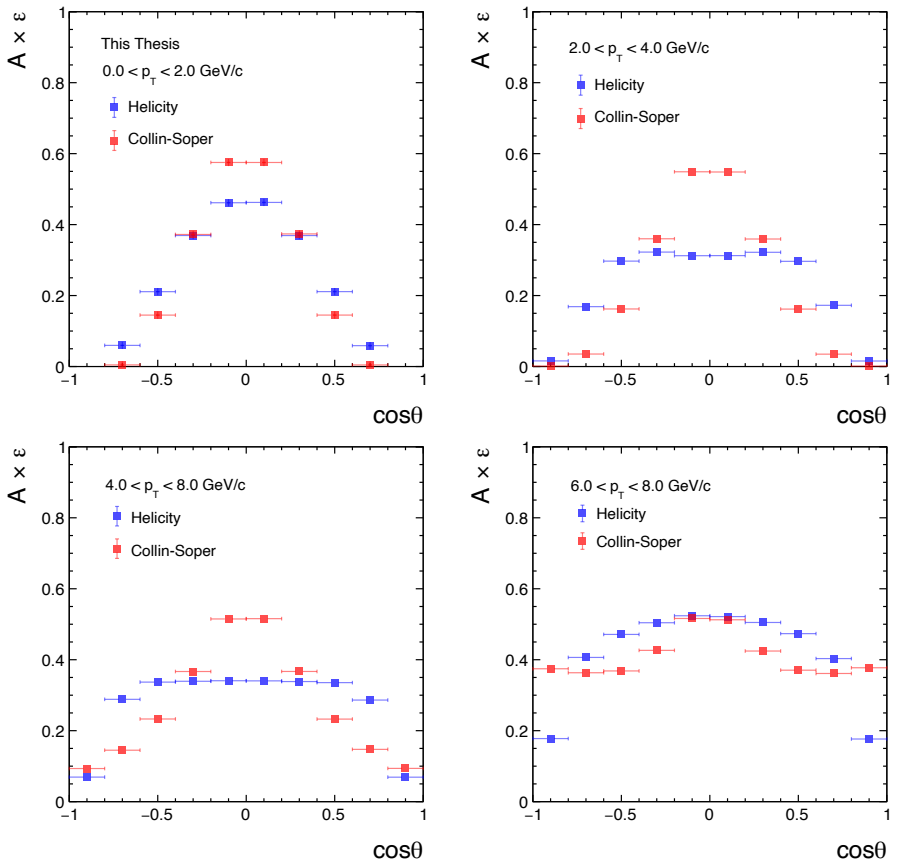

Figure 4.17: A×ε as a function of *cosθ* for both Helicity and Collin-Soper frame [123].

Fig. 4.15 shows the DCB+VWG fits to the dimuon invariant mass spectra for ten *cosθ* bins in the $4.0 < p_{\mathrm{T}} < 8.0$ GeV/c bin in the HE frame. The bins are chosen so that the spectra are symmetric around zero. The lower panels in the plots show the data-to-fit ratio. All the fits are converged and show reasonable χ^2/ndf ratios. We have extracted the raw number of ψ(2S) from these fittings. Such analyses have been done for all p_{T} and *cosθ* bins for HE and CS frames. Similarly, in Fig. 4.16, we have shown the DCB+VWG fits to the dimuon invariant mass spectra for ten ϕ bins in the $4.0 < p_{\mathrm{T}} < 8.0$ GeV/c bin in the HE frame. Here also, the bins are chosen so that the spectra are symmetric around zero. All

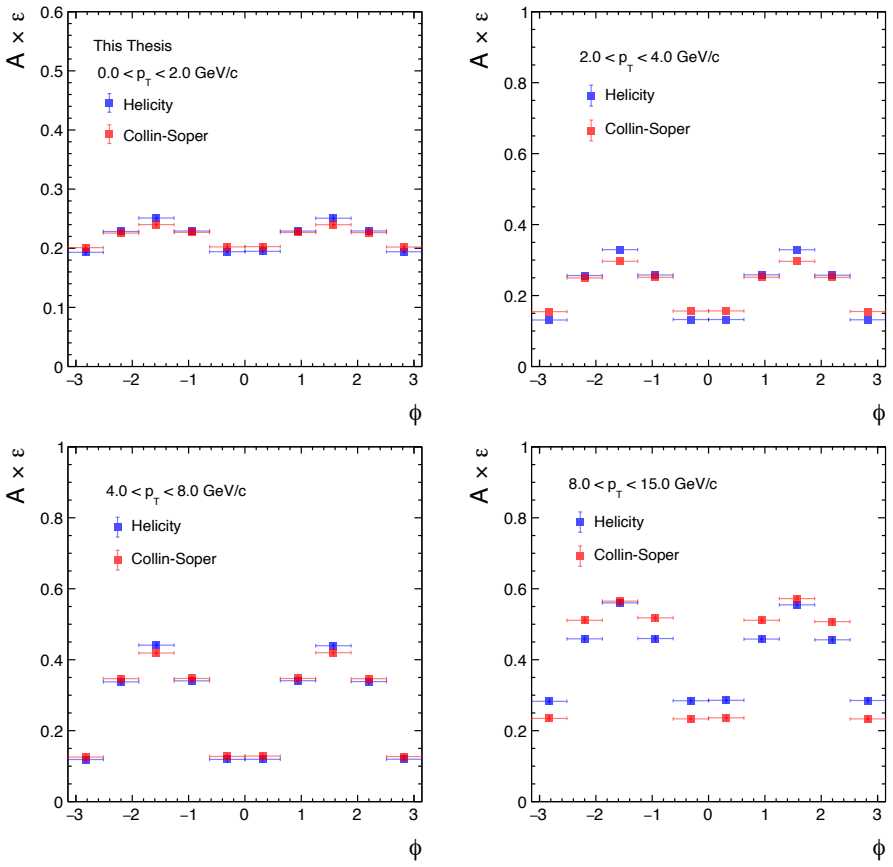

Figure 4.18: A×ε as a function of ϕ for both Helicity and Collin-Soper frame [123].

the fits are converged. The same has been done for all p_{T} bins in both HE and CS frames, and we have extracted the raw ψ(2S) numbers as a function of ϕ and p_{T}. In addition, we have also done the same analysis in ten $\tilde{\phi}$ bins and extracted the raw ψ(2S) numbers in both HE and CS frames.

In Fig. 4.17, we have plotted the $A \times \varepsilon$ as a function of $cos\theta$ for various p_{T} bins in both HE and CS frames. For our analysis, we neglect the bins where the $A \times \varepsilon$ is less than 0.1 to avoid detector inefficiency. Similarly, in Fig. 4.18, we have plotted the $A \times \varepsilon$ as a function of ϕ in both HE and CS frames. This helps us to estimate the corrected number of ψ(2S) in the angular bins, which we will finally fit to extract the polarization parameters.

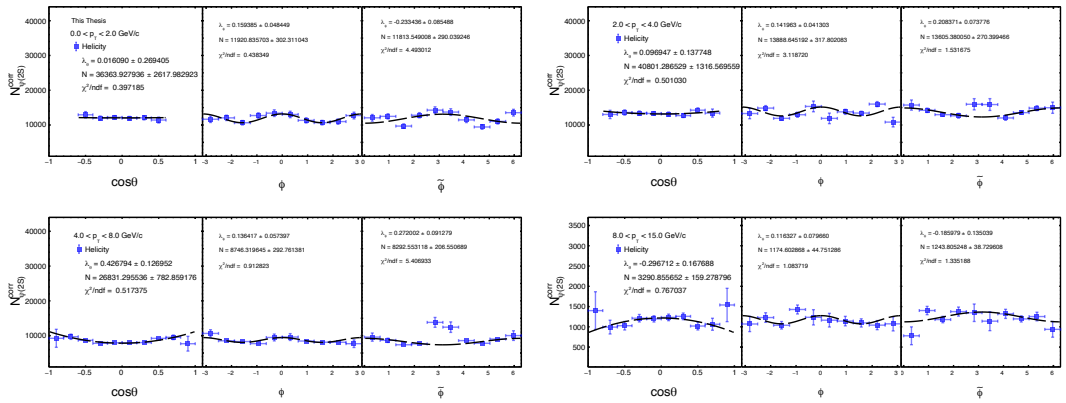

Figure 4.19: Fits to the $cos\theta$, ϕ and $\tilde{\phi}$ spectra for helicity frame for different p_{T} bins [123].

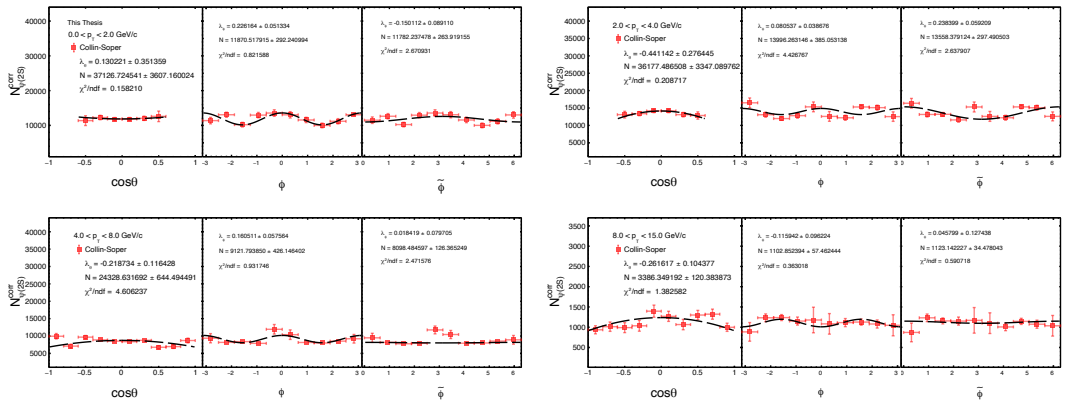

Figure 4.20: Fits to the $cos\theta$, ϕ and $\tilde{\phi}$ spectra for Collin-Soper frame for different p_{T} bins [123].

4.5 ψ(2S) polarization

We have fitted the corrected ψ(2S) angular distributions with Eq. 4.11, Eq. 4.12, Eq. 4.13 and obtained the polarization parameters. Fig. 4.19 shows the fitting to the corrected ψ(2S) angular distributions in the HE frame. Similarly, in Fig. 4.20, we have shown the 1D fits to the corrected angular distributions of ψ(2S) in the CS

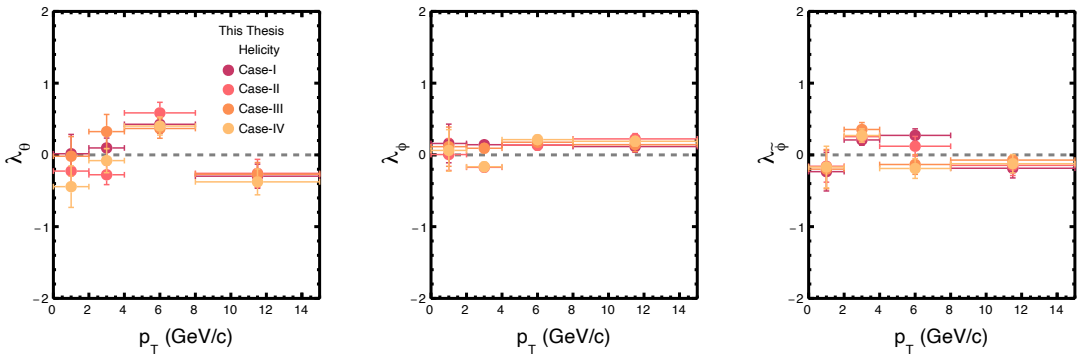

Figure 4.21: Polarization parameters λ_θ, λ_ϕ and $\lambda_{\theta\phi}$ as functions of transverse momentum for helicity frame [123].

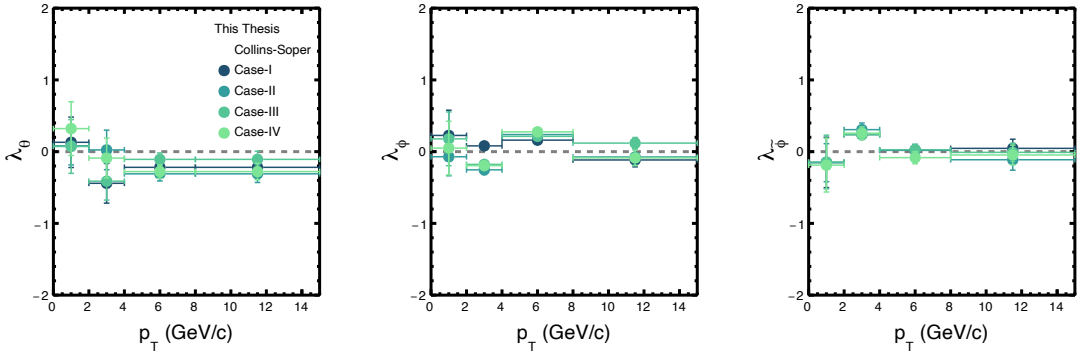

Figure 4.22: Polarization parameters λ_θ, λ_ϕ and $\lambda_{\theta\phi}$ as functions of transverse momentum for Collins-Soper frame [123].

frame. The fits are converged and show reasonable χ^2/ndf values. The extracted polarization parameters are then plotted as functions of transverse momentum.

We have done the same analysis for different combinations of signal and background functions. Case I represents the DCB + VWG fitting scenario, Case II is DCB + Double exponential, Case III is NA60 + VWG, and Case IV is NA60 + Double exponential. The acceptance times efficiency is also estimated by fitting the MC simulated data with both DCB and NA60 functions for their

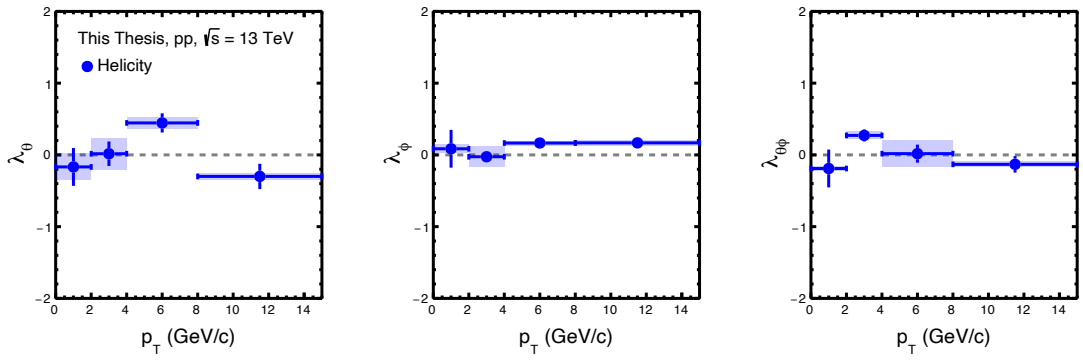

Figure 4.23: Polarization parameters λ_θ, λ_ϕ and $\lambda_{\theta\phi}$ as functions of transverse momentum for helicity frame with systematic uncertainties [123].

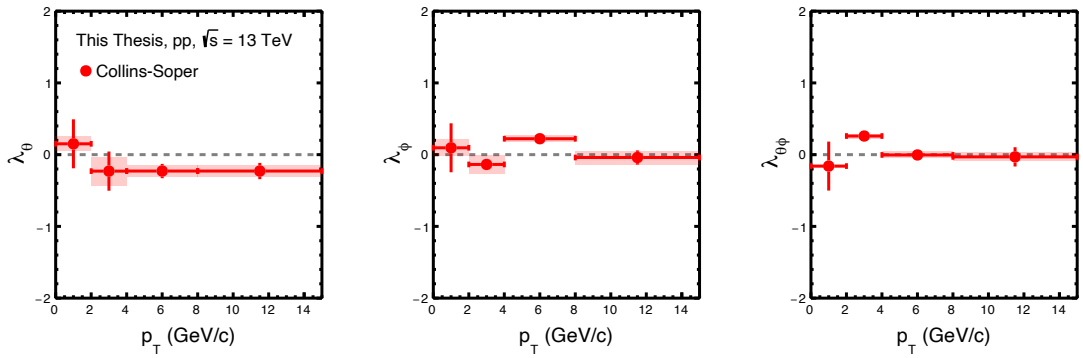

Figure 4.24: Polarization parameters λ_θ, λ_ϕ and $\lambda_{\theta\phi}$ as a function of transverse momentum for Collins-Soper frame with systematic uncertainties [123].

respective cases. Fig. 4.21 shows the polarization parameters λ_θ, λ_ϕ and $\lambda_{\theta\phi}$ as functions of transverse momentum for all four cases in the HE frame. Similarly, Fig. 4.22 shows the same for the CS frame. The estimation from different signal and background functions will contribute to the systematic uncertainties of the polarization parameters.

Fig. 4.23 shows the polarization parameters λ_θ, λ_ϕ and $\lambda_{\theta\phi}$ with the systematic uncertainties as functions of transverse momentum in the HE frame. The

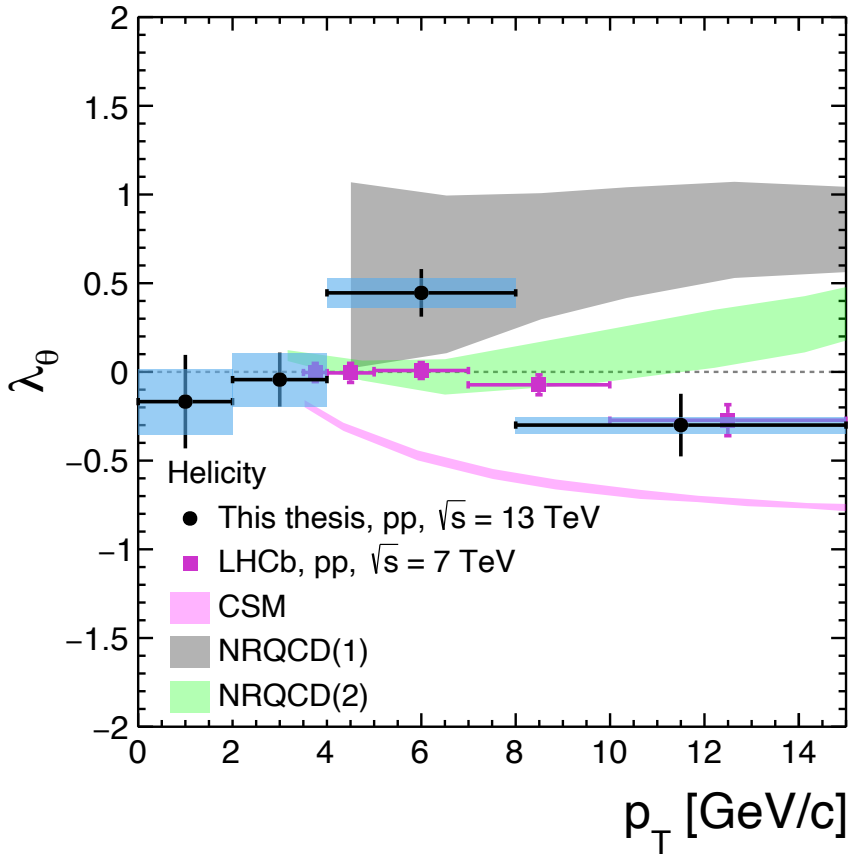

Figure 4.25: λ_θ as a function of transverse momentum for helicity frame [123]. The magneta markers represent the LHCb results for pp collisions at $\sqrt{s} = 7$ TeV [20].

systematic uncertainties come from the different choices of signal and background functions. The bars represent the statistical uncertainties, whereas the shaded boxes represent the systematic uncertainties. We observe that within uncertainties, the polarization parameters are zero, except for $4.0 < p_{\mathrm{T}} < 8.0$ GeV/c, which shows a finite value of λ_θ. In Fig. 4.24, we have plotted the polarization parameters λ_θ, λ_ϕ and $\lambda_{\theta\phi}$ with the systematic uncertainties as function of p_{T} in the CS frame. Here also, we observe that all the polarization parameters are zero within uncertainties.

Finally, in Fig. 4.25, we have compared our estimated λ_θ in the HE frame with

that of the LHCb results for pp collisions at $\sqrt{s} = 7$ TeV. We have also shown the estimations from various theoretical models. A good agreement can be observed between our results and the LHCb one, except for the $4.0 \leq p_{\rm T} \geq 6.0$ GeV/c, where we get a substantial polarization. In addition, no theoretical estimations can explain our results for the whole $p_{\rm T}$ range. The prediction from the color singlet model [21] shows a longitudinal polarization, whereas the NRQCD 1 [21] and NRQCD 2 [124] predict slightly transverse polarization. This means one should study with better statistics and a higher center of mass energies, which can give a conclusive result. Moreover, given this, better theoretical studies have to be done which can explain both the production and polarization of charmonia in high-energy hadronic collisions.

In summary, we have studied the polarization of ψ(2S) in pp collisions at $\sqrt{s}$ = 13 TeV with the ALICE collaboration. We have estimated the polarization parameters; λ_θ, λ_ϕ and $\lambda_{\theta\phi}$ and studied them as functions of $p_{\rm T}$ in both helicity and Collin-Soper frames. We observe almost zero polarization within the uncertainties in both frames. However, the helicity frame observes a 1.58σ deviation from zero in 4.0 – 8.0 $p_{\rm T}$ bin. Our results are almost in agreement with the LHCb results in pp collisions at $\sqrt{s} = 7$ TeV. In addition, no theoretical prediction which has been discussed matches with the experimental results for all $p_{\rm T}$ ranges. Recently, ALICE Run 3 has been going on with a higher luminosity, which results in higher statistics. This means a lower statistical uncertainty, especially for quarkonia production and polarization studies, which will give a conclusive understanding of quarkonium polarization in higher centre of mass energies. With more statistics, one can also explore multiplicity-dependent quarkonia polarization in pp collisions, which will be essential to understanding the polarization results of heavy-ion collision systems. In addition, it will give us information about whether there are other contributors to polarization in hadronic collisions.

Chapter 5

Summary

The research works discussed in this PhD thesis have been carried out at the Indian Institute of Technology (IIT) Indore, India, within the ALICE collaboration at the LHC, CERN, Geneva. The PhD project consists of experimental data analysis and phenomenological studies to understand polarization in the hadronic collisions and the possible quark gluon plasma (QGP) medium formation in high multiplicity proton+proton collisions at ultra-relativistic energies.

In this thesis, we have made an extensive study to look for the possible formation of QGP droplets in the matter formed in high multiplicity pp collisions. For this study, we have taken the help of color string percolation model (CSPM). This is a QCD inspired model which helps us to study the matter formed in ultra-relativistic collisions by taking inputs from the experimental data. Thus, it allows us to have a charged-particle multiplicity as well as center of mass energy-dependent analysis. We have studied various thermodynamic and transport properties such as the mean free path (λ), initial energy density (ϵ), speed of sound squared ($c_{\rm s}^2$), shear viscosity to entropy density ratio (η/s), bulk viscosity to entropy density ratio (ζ/s), isothermal compressibility ($\kappa_{\rm T}$) and bulk modulus (B). The mean free path of the system gives us information about possible thermalization, whereas the initial energy density tells us whether the system can form a deconfined medium. Similarly, the $c_{\rm s}^2$ can tell us about the

interaction in the system and how much deviation there is from an ideal massless gas. Moreover, the η/s and ζ/s can give us information about the fluidity in the system as well as quantify the location of the critical behavior. On the other hand, the isothermal compressibility can tell us about the deviation of the system from perfect fluid. These properties can help us understand and characterize the systems formed in ultra-relativistic collisions. We have also compared our results with estimations from various existing models. Our results from CSPM match with other models qualitatively. We have found a threshold of charged particle multiplicity $\langle dN_{\rm ch}/d\eta\rangle \geq 10$–$20$, after which we observe a change in the dynamics of the system. From the estimation of η/s and $\kappa_{\rm T}$, we have concluded that the matter formed in ultra-relativistic collisions is closest to a perfect fluid found in nature. Furthermore, we also estimated the jet quenching parameter and studied it as a function of charged-particle multiplicity. In addition, we have compared our results with that from various theoretical models, and found our results to be in qualitative agreement with other models. We observed that, through our approach, the high multpilicity pp collisions show a substantial jet quenching which is yet to be observed in experimental data. Our study concludes that after $\langle dN_{\rm ch}/d\eta\rangle \geq 10$–$20$, a system may possibly form a deconfined medium regardless of the collision systems or collision energies.

We have also estimated the hadronic phase lifetime for various collision systems and collision energies. In addition, we have also explored the location of the QGP phase boundary. For these purposes, we have taken the help of hadronic resonance particles. Resonances are higher excited states of stable counterparts, which have higher masses and lower lifetimes. In this study, we have used a nuclear-decay-type toy model for our study, and K^{*0} resonance is taken as our probe. K^{*0} has a very small lifetime of 4.26 fm/c. It also suffers rescattering and regeneration in the hadronic phase, which makes it an excellent probe for estimating the hadronic phase lifetime. K^{*0}/K ratio at the chemical freeze-out is taken as our initial sample, and K^{*0}/K at the kinetic freeze-out boundary is taken as

the final sample. We have then estimated the hadronic phase lifetime as a function of final state charged-particle multiplicity for various collision systems and collision energies. We observe a strong charged-particle multiplicity-dependent trend, although a weak collision energy dependency is also observed. On the other hand, we have used ϕ as our probe for locating the QGP phase boundary. Unlike K^{*0}, ϕ has a relatively longer lifetime and doesn't suffer rescattering and regeneration in the hadronic phase. We fit the Boltzmann-Gibbs Blastwave function to the soft part of the transverse momentum spectra of ϕ and extract the thermal temperature ($T_{\rm th}$) and the average velocity ($\langle\beta\rangle$) of the system. A strong charged-particle multiplicity dependency on both $T_{\rm th}$ and $\langle\beta\rangle$. We also observe that after $\langle dN_{\rm ch}/d\eta\rangle \simeq$ 10–20, after which a change in the dynamics of the system is observed. We then estimate the effective temperature ($T_{\rm eff}$) of the system. We observe that $T_{\rm eff}$ is independent of $\langle dN_{\rm ch}/d\eta\rangle$. This means that ϕ meson freezes out at the same temperature irrespective of the collision system, collision energy or multiplicity. ϕ meson keeps the information of QGP phase boundary intact, thus the trend of $T_{\rm eff}$ suggests that the location of the QGP phase boundary is independent or weakly dependent on charged-particle multiplicity. This observation is supported by earlier studies of of $T_{\rm ch}$ which is also independent of final-state charged particle multiplicity, which concludes that the QGP phase boundary doesn't depend on the collision systems or the final state charged-particle multiplicity.

For the experimental part of this thesis, the first measurement of ψ(2S) meson polarization in pp collisions at $\sqrt{s}$ = 13 TeV with ALICE at the LHC is reported. ψ(2S), a bound state of charm-anticharm quarks, is a unique candidate to study the hadronic collisions, which allows us to test the QCD theories while confronting experimental data. We have given a brief of the ALICE muon spectrometer, which is the detector we have used in our study, because we look into the dimuon decay channels of the charmonia. We have also given a brief introduction to the mathematical formulation of charmonia polarization. Then,

we study the p_{T} differential, as well as the angular differential ψ(2S) production. We have estimated the acceptance times efficiency of ψ(2S) from the MC simulation, which allows us to estimate the corrected ψ(2S) number as a function of transverse momentum and angular variables. After that, we have done 1D fits to the corrected ψ(2S) angular distributions and extracted the polarization parameters, λ_θ, λ_ϕ and $\lambda_{\theta\phi}$. Finally, we have studied the polarization parameters as a function of transverse momentum. All these analyses are done for two frames of reference; the helicity and Collin-Sopper frames. We observe zero polarization within uncertainties for both frames of reference. However, a finite polarization can be seen for $4.0 < p_{\mathrm{T}} < 8.0$ GeV/c. In addition, we have compared our results with that of pp collisions at $\sqrt{s} = 7$ TeV for LHCb collaboration. We have also compared it with various theoretical models. In view of our results, better theoretical studies need to be done which can explain both the charmonia production and polarization in hadronic collisions. Moreover, one needs to study charmonia polarization at a higher center of mass energies and higher statistics which will allow us to have conclusive results. ALICE Run 3 moving towards a higher luminosity will help us to do these studies with higher statistics and lower uncertainties. Furthermore, this will also help one to study the polarization parameters as a function of charged particle multiplicity, which will shed more light on the polarization studies.

Chapter 6

Appendix

6.1 Run Numbers

The following are the run numbers used to analyse ψ(2S) polarization measurement in pp collisions at $\sqrt{s}$ = 13 TeV [123].

LHC18p

294925, 294916, 294884, 294883, 294880, 294877, 294875, 294852, 294818, 294817, 294816, 294815, 294813, 294809, 294775, 294774, 294772, 294769, 294749, 294747, 294743, 294742, 294741, 294722, 294721, 294718, 294716, 294715, 294710, 294703, 294653, 294636, 294634, 294633, 294632, 294593, 294591, 294590, 294588, 294587, 294586, 294563, 294558, 294556, 294553, 294531, 294530, 294529, 294527, 294526, 294525, 294524, 294503, 294502, 294310, 294308, 294307, 294305, 294242, 294241, 294212, 294210, 294208, 294205, 294201, 294200, 294199, 294156, 294155, 294154, 294152, 294131, 294128, 294013, 294012, 294011, 294010, 294009

LHC18o

293898, 293896, 293893, 293891, 293886, 293856, 293831, 293830, 293829, 293809, 293807, 293806, 293805, 293802, 293799, 293776, 293774, 293773, 293741, 293740, 293698, 293696, 293695, 293692, 293691, 293588, 293587, 293497, 293496, 293494, 293475, 293474, 293424, 293413, 293392, 293391, 293388, 293386, 293368,

LHC18m

292397, 292298, 292274, 292273, 292270, 292269, 292265, 292242, 292241, 292240, 292192, 292168, 292167, 292166, 292164, 292163, 292162, 292161, 292160, 292140, 292115, 292114, 292109, 292108, 292107, 292106, 292081, 292080, 292077, 292075, 292062, 292061, 292060, 292040, 292012, 291982, 291953, 291948, 291945, 291944, 291943, 291942, 291803, 291796, 291795, 291769, 291760, 291756, 291755, 291729, 291706, 291698, 291697, 291694, 291692, 291690, 291665, 291661, 291657, 291614, 291590, 291485, 291484, 291482, 291481, 291457, 291456, 291453, 291451, 291447, 291446, 291420, 291419, 291417, 291416, 291402, 291400, 291399, 291397, 291375, 291373, 291363, 291362, 291361, 291360, 291286, 291285, 291284, 291283, 291282, 291265, 291263, 291041, 291037, 291035, 291006, 291005, 291004, 291003, 291002, 290979, 290976, 290975, 290948, 290944, 290943, 290935, 290932, 290895, 290894, 290892, 290862, 290853, 290848, 290790, 290787, 290776, 290774, 290769, 290766, 290764, 290721, 290699, 290696, 290692, 290687, 290665, 290660, 290658, 290645, 290632, 290627, 290615, 290614, 290613, 290612, 290590, 290553, 290550, 290549, 290544, 290540, 290539, 290538, 290501, 290499, 290469, 290459, 290458, 290456, 290428, 290427, 290425, 290423, 290421, 290420, 290418, 290411, 290404, 290401, 290375, 290374, 290350, 290327, 290324, 290323, 290300, 290297, 290293, 290254, 290223, 290222

LHC18l

289971, 289966, 289943, 289941, 289940, 289935, 289931, 289928, 289888, 289884, 289880, 289857, 289856, 289855, 289852, 289849, 289830, 289816, 289815, 289814, 289811, 289808, 289775, 289757, 289731, 289729, 289724, 289723, 289721, 289666, 289664, 289660, 289659, 289658, 289657, 289654, 289632, 289626, 289625, 289582, 289581, 289579, 289577, 289576, 289574, 289494, 289493, 289468, 289466, 289465, 289462, 289444, 289426, 289373, 289370, 289369, 289368, 289367, 289366, 289365, 289363, 289356, 289355, 289354, 289353, 289309, 289308, 289306, 289303, 289300, 289280, 289278, 289277, 289276, 289275, 289254, 289253, 289249, 289247,

LHC18j

288943

LHC18i

288909, 288908, 288903, 288897, 288893, 288892, 288868, 288864, 288862, 288861

LHC18h

288804

LHC18g

288750, 288748, 288743, 288690, 288689, 288688

LHC18f

287977, 287941, 287923, 287783, 287658, 287657, 287656, 287654, 287578, 287576, 287575, 287573, 287524, 287521, 287520, 287517, 287516, 287513, 287484, 287481, 287451, 287389, 287388, 287387, 287385, 287381, 287380, 287360, 287358, 287356, 287355, 287353, 287349, 287347, 287346, 287344, 287343, 287325, 287324, 287323, 287283, 287254, 287251, 287250, 287249, 287248, 287209, 287208, 287204, 287203, 287202, 287201, 287155, 287137, 287077, 287072, 287071, 287066, 287064, 287063, 287021, 287000

LHC18e

286937, 286936, 286933, 286932, 286931, 286930, 286911, 286910, 286908, 286907, 286877, 286876, 286874, 286852, 286850, 286848, 286846, 286810, 286809, 286801, 286799, 286731, 286695, 286661, 286653, 286633, 286594, 286592, 286591, 286569, 286568, 286567, 286566, 286509, 286508, 286502, 286501, 286455, 286454, 286428, 286427, 286426, 286380

LHC18d

286350, 286349, 286348, 286345, 286340, 286337, 286336, 286314, 286313, 286312 286311, 286310, 286309, 286308, 286289, 286288, 286287, 286284, 286282, 286261, 286257, 286254, 286230, 286229, 286203, 286202, 286201, 286199, 286198, 286159, 286130, 286129, 286127, 286124, 286064, 286028, 286027, 286026, 286025, 286018, 286014, 285980, 285979, 285978

LHC18c

285958, 285957, 285946, 285917, 285893, 285892, 285869, 285851, 285830, 285812, 285811, 285810, 285806, 285805, 285804, 285781, 285778, 285777, 285756, 285755,

285754, 285753, 285752, 285751, 285722, 285698, 285697, 285664, 285663, 285662, 285659, 285643, 285642, 285641, 285640, 285639, 285603, 285602, 285601, 285599, 285578, 285577, 285576, 285575, 285557, 285515, 285497, 285496

LHC18b

285396, 285365, 285364, 285347, 285328, 285327, 285291, 285290, 285289, 285287, 285286, 285224, 285222, 285203, 285202, 285200, 285165, 285127, 285125, 285108, 285106, 285066, 285065, 285064, 285015, 285014, 285013, 285012, 285011, 285010, 285009, 285008

LHC17r

282704, 282703, 282702, 282700, 282677, 282676, 282673, 282671, 282670, 282668, 282667, 282666, 282653, 282651, 282629, 282622, 282620, 282618, 282615, 282609, 282608, 282607, 282606, 282580, 282579, 282575, 282573, 282546, 282545, 282544, 282528, 282504

LHC17o

281961, 281956, 281953, 281946, 281940, 281939, 281931, 281928, 281918, 281916, 281915, 281894, 281893, 281892, 281755, 281754, 281753, 281751, 281750, 281741, 281713, 281709, 281707, 281706, 281705, 281651, 281645, 281642, 281640, 281635, 281634, 281633, 281592, 281583, 281581, 281580, 281574, 281569, 281568, 281563, 281562, 281557, 281511, 281509, 281477, 281475, 281450, 281449, 281446, 281444, 281441, 281415, 281321, 281301, 281277, 281275, 281244, 281243, 281242, 281241, 281240, 281213, 281212, 281191, 281190, 281181, 281180, 281179, 281081, 281080, 281079, 281062, 281061, 281060, 281036, 281035, 281033, 281032, 280998, 280997, 280996, 280994, 280990, 280947, 280943, 280940, 280936, 280897, 280890, 280881, 280880, 280856, 280848, 280847, 280845, 280844, 280842, 280793, 280792, 280786, 280768, 280767, 280766, 280765, 280764, 280763, 280761, 280756, 280755, 280754, 280753, 280706, 280705, 280681, 280679, 280676, 280671, 280650, 280648, 280647, 280645, 280639, 280637, 280634, 280613, 280583, 280581, 280576, 280575, 280574, 280551, 280550, 280547, 280546, 280519, 280518, 280448, 280447, 280446, 280445, 280443, 280419, 280418, 280415, 280413, 280412, 280406, 280405, 280403, 280375,

280374, 280352, 280351, 280350, 280349, 280348, 280312, 280310, 280290, 280286, 280285, 280284, 280283, 280282

LHC17m

280140, 280135, 280134, 280131, 280126, 280118, 280114, 280111, 280108, 280066, 280052, 280051, 280049, 279955, 279954, 279952, 279893, 279890, 279886, 279884, 279880, 279879, 279855, 279854, 279853, 279830, 279827, 279826, 279773, 279749, 279747, 279719, 279718, 279715, 279689, 279688, 279684, 279682, 279679, 279677, 279676, 279642, 279641, 279600, 279598, 279597, 279583, 279565, 279564, 279563, 279562, 279561, 279560, 279559, 279488, 279487, 279483, 279441, 279439, 279435, 279410, 279391, 279355, 279354, 279349, 279348, 279344, 279342, 279312, 279310, 279309, 279274, 279273, 279270, 279268, 279267, 279265, 279264, 279242, 279238, 279235, 279234, 279208, 279207, 279201, 279199, 279157, 279155, 279130, 279125, 279123, 279122, 279117, 279106, 279075, 279074, 279073, 279068, 279044, 279043, 279041, 279038, 279037, 279036, 279008, 279007, 279005, 278999, 278964, 278963, 278959, 278941, 278939, 278936, 278915, 278914

LHC17l

278216, 278215, 278191, 278189, 278167, 278166, 278165, 278164, 278163, 278130, 278127, 278126, 278123, 278122, 278121, 277996, 277991, 277989, 277988, 277987, 277952, 277930, 277907, 277904, 277903, 277901, 277900, 277899, 277898, 277897, 277876, 277870, 277848, 277847, 277842, 277841, 277836, 277834, 277801, 277800, 277799, 277795, 277794, 277749, 277747, 277746, 277725, 277577, 277576, 277575, 277574, 277537, 277536, 277531, 277530, 277479, 277478, 277476, 277473, 277472, 277470, 277418, 277417, 277389, 277386, 277384, 277383, 277360, 277314, 277312, 277310, 277293, 277262, 277256, 277197, 277196, 277194, 277193, 277189, 277188, 277184, 277183, 277182, 277181, 277180, 277155, 277121, 277117, 277091, 277087, 277082, 277079, 277076, 277073, 277037, 277017, 277016, 277015, 276972, 276971, 276970, 276969, 276920, 276917, 276916, 276762, 276675, 276674, 276672, 276671, 276670, 276669, 276644, 276608, 276557, 276553, 276552, 276551

LHC17k

276508, 276507, 276506, 276500, 276462, 276461, 276439, 276438, 276437, 276435, 276434, 276432, 276429, 276351, 276348, 276302, 276297, 276294, 276292, 276291, 276290, 276259, 276230, 276205, 276178, 276177, 276170, 276169, 276166, 276145, 276141, 276140, 276108, 276105, 276104, 276102, 276099, 276098, 275664, 275661, 275657, 275650, 275648, 275624, 275559, 275558, 275515, 275472, 275471, 275467, 275459, 275457, 275453, 275452, 275448, 275406, 275404, 275401, 275369, 275361, 275360, 275357, 275332, 275328, 275283, 275247, 275246, 275245, 275188, 275177, 275175, 275174, 275173, 275151, 275150, 275149, 275076, 275075, 275073, 275070, 275068, 275067, 274979, 274978, 274886, 274884, 274883, 274882, 274822, 274817, 274815, 274811, 274807, 274806, 274803, 274802, 274801, 274743, 274736, 274708

LHC17i

274442, 274390, 274387, 274385, 274364, 274363, 274360, 274357, 274355, 274329, 274283, 274281, 274280, 274278, 274276, 274271, 274270, 274269, 274268, 274266, 274264, 274263, 274259, 274232, 274212, 274148, 274147, 274125, 274094, 274092, 274064, 274063, 274058, 273986, 273985, 273946, 273942, 273918, 273889, 273887, 273886, 273885, 273825, 273824, 273719, 273711, 273709, 273695, 273690, 273689, 273687, 273654, 273653, 273593, 273592, 273591

LHC17h

273103, 273101, 273100, 273099, 273077, 273010, 273009, 272985, 272983, 272976, 272949, 272947, 272939, 272935, 272934, 272933, 272932, 272905, 272903, 272880, 272873, 272871, 272870, 272836, 272835, 272834, 272833, 272829, 272828, 272784, 272783, 272782, 272762, 272760, 272749, 272747, 272746, 272692, 272691, 272620, 272619, 272608, 272607, 272585, 272577, 272575, 272574, 272521, 272469, 272468, 272466, 272463, 272462, 272461, 272414, 272413, 272411, 272400, 272394, 272360, 272359, 272335, 272194, 272156, 272155, 272154, 272153, 272152, 272151, 272123, 272101, 272100, 272076, 272075, 272042, 272041, 272040, 272039, 272038, 272036, 272020, 271970, 271969, 271962, 271955, 271953, 271946, 271925, 271921, 271912, 271886, 271879, 271878, 271874, 271873, 271871, 271870, 271868

LHC16p

264347, 264346, 264345, 264341, 264336, 264312, 264305, 264281, 264279, 264277, 264273, 264267, 264266, 264265, 264264, 264262, 264261, 264260, 264259, 264238, 264233, 264232, 264198, 264197, 264194, 264188, 264168, 264164, 264138, 264137, 264129, 264110, 264109, 264086, 264085, 264082, 264078, 264076

LHC16o

264035, 264033, 263985, 263984, 263981, 263979, 263978, 263977, 263923, 263920, 263917, 263916, 263905, 263866, 263863, 263861, 263830, 263829, 263824, 263823, 263813, 263810, 263803, 263793, 263792, 263790, 263787, 263786, 263785, 263784, 263744, 263743, 263741, 263739, 263738, 263737, 263691, 263690, 263689, 263682, 263662, 263657, 263654, 263653, 263652, 263647, 263529, 263497, 263496, 263490, 263487, 263332, 262858, 262855, 262853, 262849, 262847, 262844, 262842, 262841, 262778, 262777, 262776, 262768, 262760, 262727, 262725, 262723, 262719, 262717, 262713, 262705, 262635, 262632, 262628

LHC16k

258537, 258499, 258498, 258477, 258456, 258454, 258452, 258426, 258399, 258393, 258391, 258388, 258387, 258359, 258336, 258332, 258307, 258306, 258303, 258302, 258301, 258299, 258280, 258278, 258274, 258273, 258271, 258270, 258258, 258257, 258256, 258204, 258203, 258202, 258197, 258178, 258117, 258114, 258113, 258109, 258108, 258107, 258063, 258062, 258060, 258059, 258049, 258048, 258045, 258042, 258041, 258039, 258019, 258017, 258014, 258012, 258008, 257989, 257986, 257979, 257963, 257960, 257958, 257957, 257939, 257937, 257936, 257932, 257912, 257901, 257893, 257892, 257737, 257735, 257734, 257733, 257727, 257725, 257724, 257697, 257694, 257688, 257687, 257685, 257684, 257682, 257644, 257642, 257636, 257635, 257632, 257630, 257606, 257605, 257604, 257601, 257595, 257594, 257592, 257590, 257588, 257587, 257566, 257565, 257564, 257563, 257562, 257561, 257560, 257541, 257540, 257531, 257530, 257492, 257491, 257490, 257488, 257487, 257474, 257468, 257457, 257433, 257364, 257358, 257330, 257322, 257320, 257318, 257260, 257224, 257095, 257092, 257086, 257084, 257083, 257082, 257080, 257077, 257071, 257026, 257021, 257012, 257011, 256944, 256942, 256941, 256697, 256695, 256694, 256691,

256684, 256681, 256677, 256676, 256658, 256620, 256619, 256591, 256567, 256565, 256564, 256561, 256560, 256557, 256556, 256554, 256552, 256512, 256510, 256506, 256504

LHC16j

256420, 256418, 256417, 256415, 256373, 256372, 256371, 256368, 256366, 256365, 256364, 256363, 256362, 256361, 256356, 256311, 256307, 256302, 256298, 256297, 256295, 256292, 256290, 256289, 256287, 256284, 256283, 256282, 256281, 256231, 256228, 256227, 256223, 256222, 256219, 256215, 256213, 256212, 256210, 256204, 256169, 256161, 256158, 256157, 256156, 256149, 256148, 256147, 256146

LHC16i

255618, 255617, 255616, 255615, 255614, 255592, 255591, 255583, 255577, 255543, 255542, 255540, 255539

LHC16h

255467, 255466, 255465, 255463, 255447, 255442, 255440, 255415, 255402, 255398, 255352, 255351, 255350, 255283, 255280, 255276, 255275, 255256, 255255, 255253, 255252, 255251, 255249, 255248, 255247, 255242, 255240, 255182, 255180, 255177, 255176, 255173, 255171, 255167, 255162, 255159, 255154, 255111, 255091, 255086, 255085, 255082, 255079, 255010, 255009, 255008, 254984, 254983, 254654, 254653, 254652, 254651, 254649, 254648, 254646, 254644, 254640, 254632, 254630, 254629, 254621, 254608, 254606, 254604, 254419

LHC16g

254332, 254331, 254304, 254302, 254293, 254205, 254204, 254199, 254193, 254178, 254175, 254174, 254149, 254148, 254147, 254128

6.2 Data analysis

6.2.1 Fitting with various tail parameters

In order to test whether our fitting was correct, we tried three different sets of tail parameters while fitting the invariant mass spectra. The difference seems minor when compared with the MC tail fitting from another existing analysis [125].

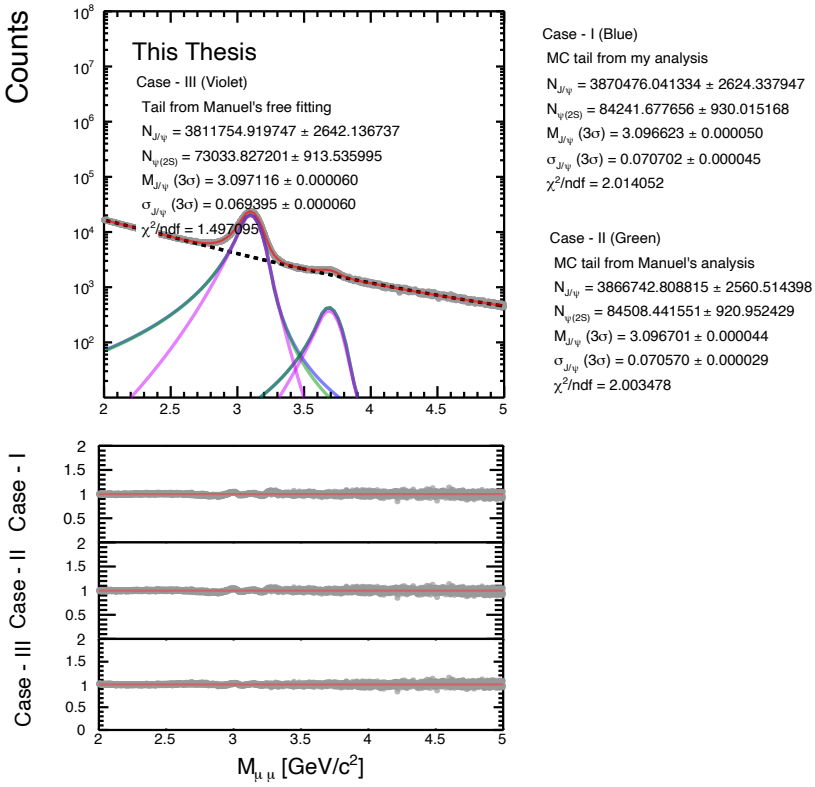

Figure 6.1: Dimuon invariant mass fitting comparison by taking different sets of tail parameters. Case I represents fitting with the tail parameters obtained from my MC analysis. Case II represents fitting with the tail parameters obtained from MC analysis of Ref. [125]. Case III represents fitting with the tail parameters obtained from free fitting in Ref. [125]. The lower panel shows the data by fit ratio for all three cases.

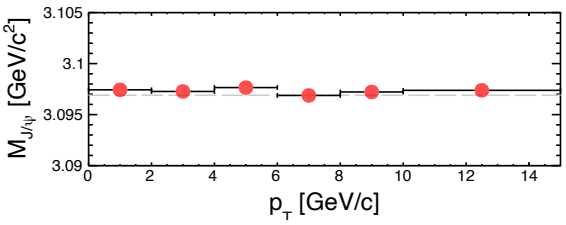

Figure 6.2: Mass of J/psi extracted from the DCB+VWG fitting as a function of transverse momentum. The dashed line represents the PDG value of J/ψ mass.

6.2.2 Effect of change in tail parameters while fitting

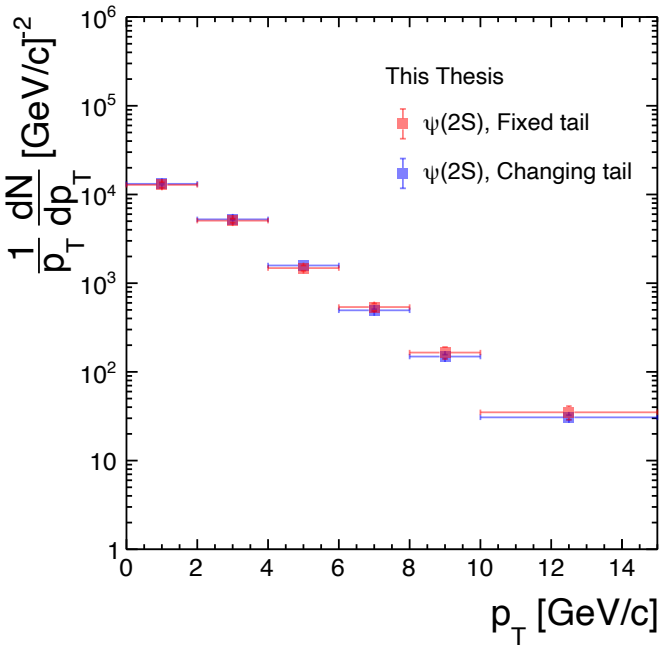

Figure 6.3: The uncorrected ψ(2S) transverse momentum spectra were obtained from two different methods of fixing tail parameters in the fit.

We checked how much the tail parameter in the invariant mass fitting affects the p_{T} spectra. For the DCB fitting, first, we took tail parameters obtained from the fit to the integrated ψ(2S) MC invariant mass spectra and fixed it for all the p_{T} bins while fitting the dimuon spectra. This is denoted in Fig.6.3 as 'Fixed

tail'. Secondly, we have used the tail parameters obtained from the MC spectra fits from different p_{T} bins and fixed them for each corresponding p_{T} bin while fitting the dimuon invariant mass spectra, shown as 'Changing tail' in Fig.6.3. The difference is minor in the low p_{T} and increases slightly for high p_{T}.

6.2.3 NA60 function

The NA60 function was introduced for the charmonium signal extraction by the NA60 collaboration. It is a Gaussian-type function around the resonance pole and has a mass-dependent width on the left and the right side. It is given by the following function;

$$f(x; N, \bar{x}, , t_1, t_2, p_1, ..p_6) = N.e^{-\frac{1}{2}(\frac{t}{t_0})^2}, \text{with } t = \frac{x - \bar{x}}{\sigma} \tag{6.1}$$

where,

$$t_0 = \begin{cases} 1 + (p_1^L(\alpha_L - t))^{p_2^L - p_3^L\sqrt{\alpha_L - t}} & , t \leq \alpha_L \\ 1 & , t_1 < t < t_2 \\ 1 + (p_1^R(\alpha_R - t))^{p_2^R - p_3^R\sqrt{t - \alpha_R}} & , t \geq \alpha_R \end{cases} \tag{6.2}$$

6.2.4 Cross-check with previous analysis

We counter-checked our analysis with a previous analysis [126]. We have compared the width of $J\psi$ extracted from the invariant mass fit with that obtained from Ref. [126]. Our result seems consistent with that of Ref. [126] as seen from the left panel of Fig. 6.6. In addition, we have also checked the ratio of ψ(2S) to J/ψ as shown in the right Fig. 6.6. The discrepancy in the low p_T region may be due to the choice of binning. It is also important to note that, in Ref. [126], the dataset taken (LHC15g, LHC15h, LHC15i, LHC15jcand LHC15l) differ from ours.

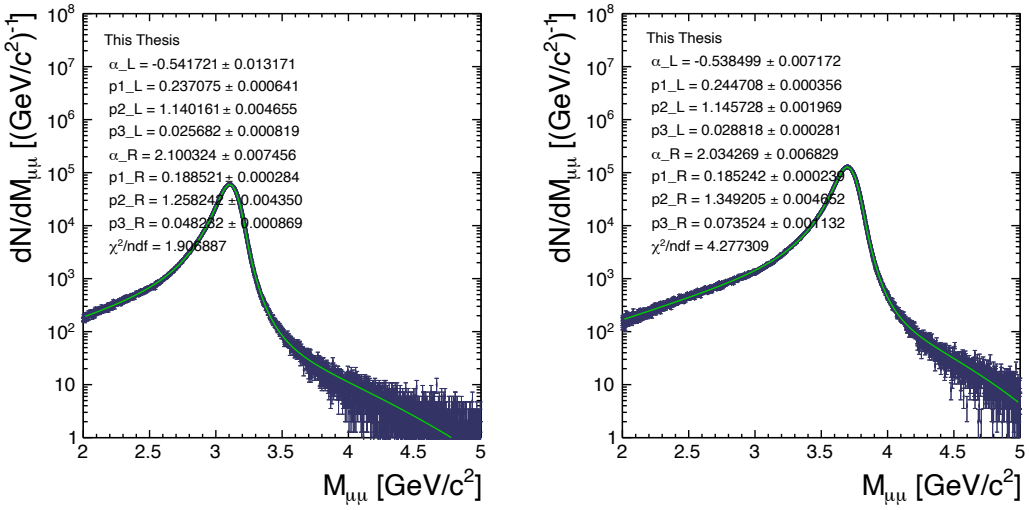

Figure 6.4: The left panel shows the NA60 function fit to the J/ψ MC invrainat mass spectra and the right panel shows the NA60 function fit to the ψ(2S) MC invrainat mass spectra [123].

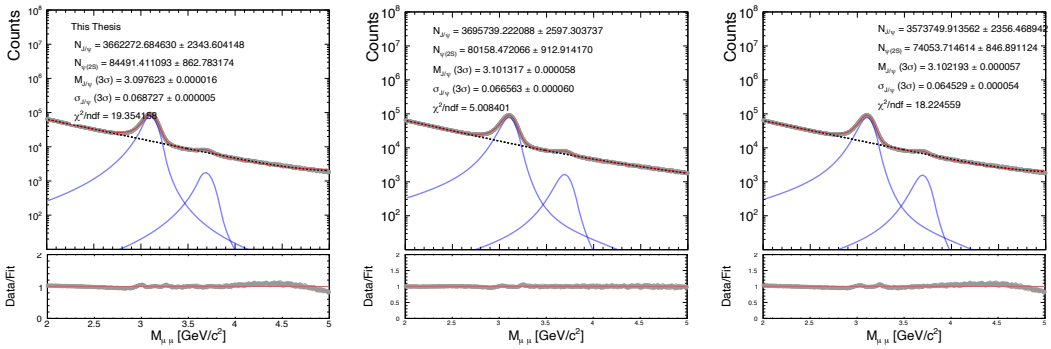

Figure 6.5: The dimuon invariant mass spectra are fitted with the Double Crystal Ball + Double Exponential function (left panel), NA60 + variable width Gaussian function (middle panel), and NA60 + Double Exponential function (right panel) [123].

6.2.5 Yield: Angular dependence

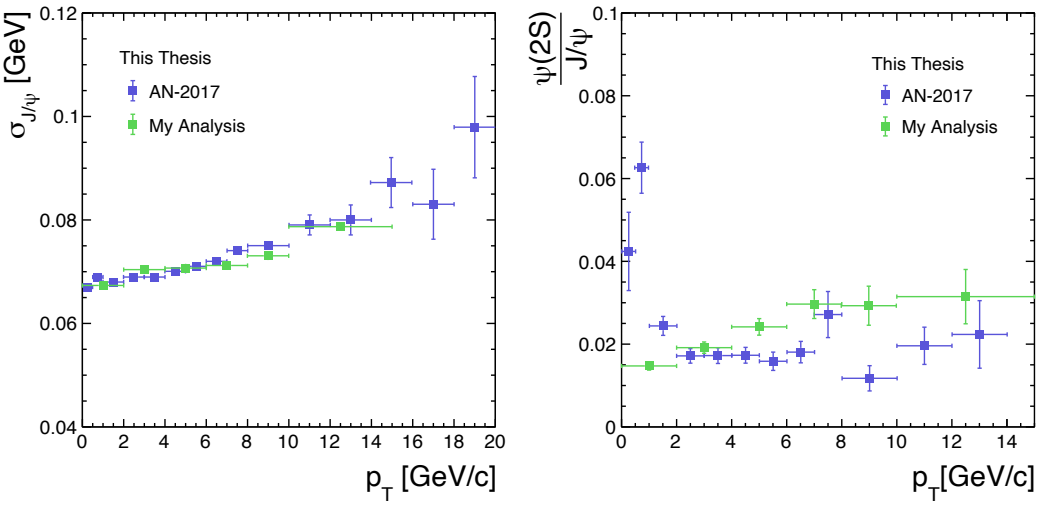

Figure 6.6: Width of $J\psi$ as a function of transverse momentum (left panel), and the ratio of ψ(2S) to J/ψ as a function of transverse momentum (right panel) [123]. The blue markers show the data taken from the analysis note [126].

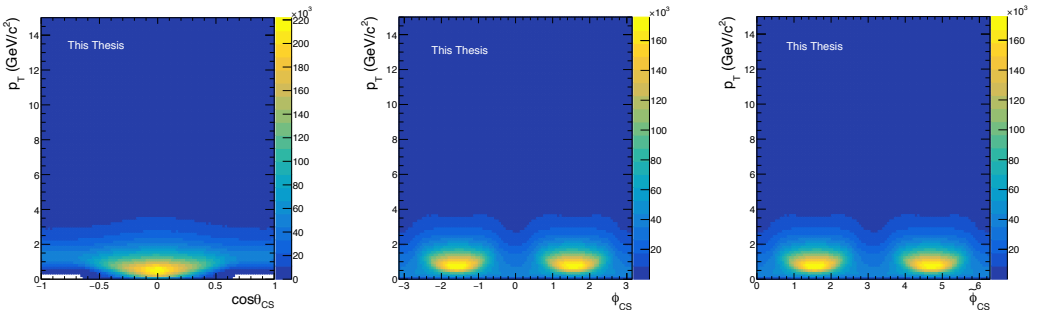

Figure 6.7: Dimuon distribution in the Collin-Soper frame as functions of transverse momentum vs $cos\theta$ (left panel), ϕ (middle panel) and $\tilde{\phi}$ (right panel) [123].

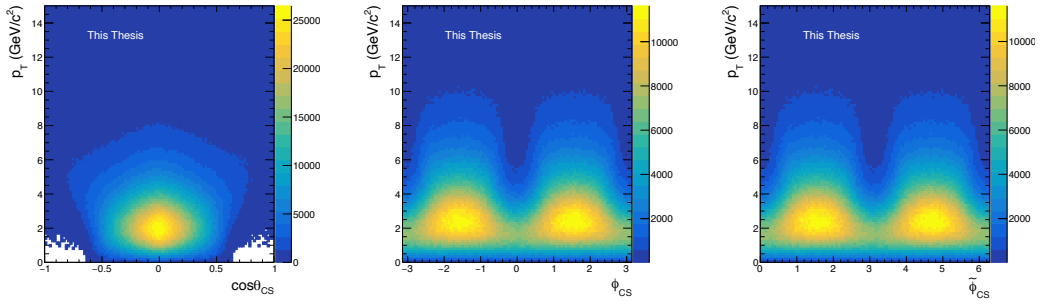

Figure 6.8: Acceptance × efficiency map of ψ(2S) for the Collin-Soper frame as functions of transverse momentum vs $cos\theta$ (left panel), ϕ (middle panel) and $\tilde{\phi}$ (right panel) [123].

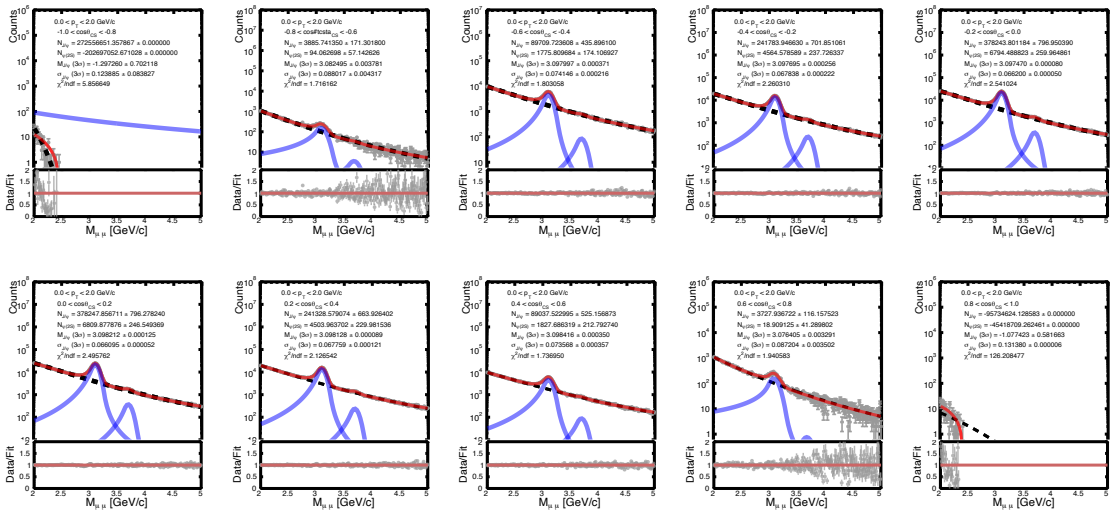

Figure 6.9: Double Crystal Ball + variable width Gaussian function fit to the invariant mass spectra for various $cos\theta$ ranges for $0.0 < p_{\mathrm{T}} < 2.0$ GeV/c in the Collin-Soper frame [123].

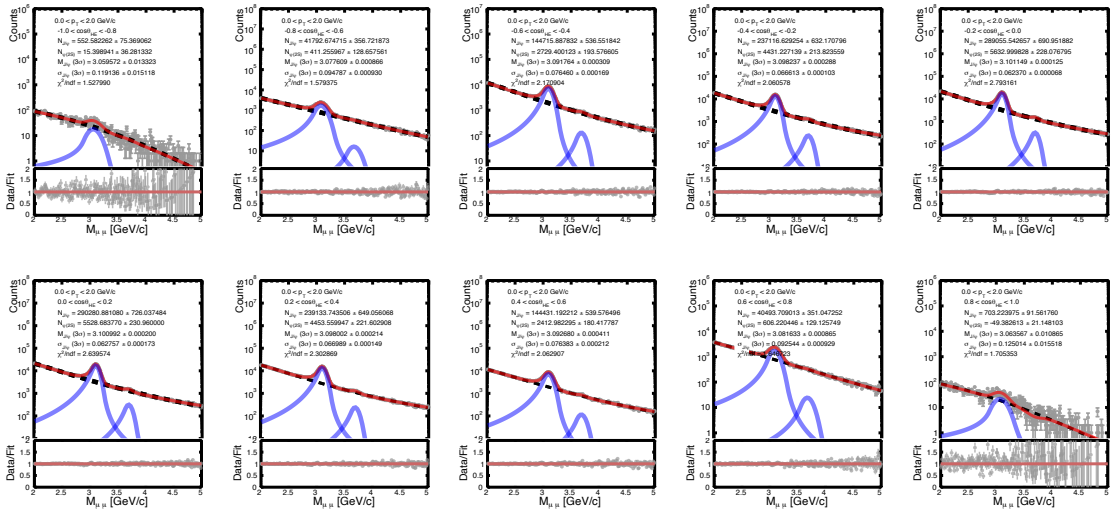

Figure 6.10: Double Crystal Ball + variable width Gaussian function fit to the invariant mass spectra for various $cos\theta$ ranges for $0.0 < p_{\mathrm{T}} < 2.0$ GeV/c in the helicity frame [123].

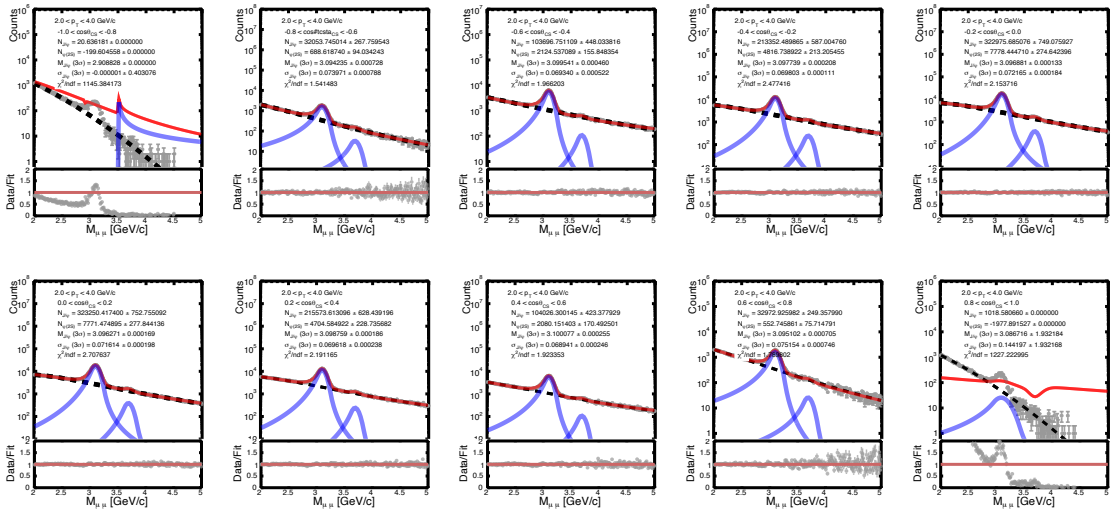

Figure 6.11: Double Crystal Ball + variable width Gaussian function fit to the invariant mass spectra for various $cos\theta$ ranges for $2.0 < p_{\mathrm{T}} < 4.0$ GeV/c in the Collin-Soper frame [123].

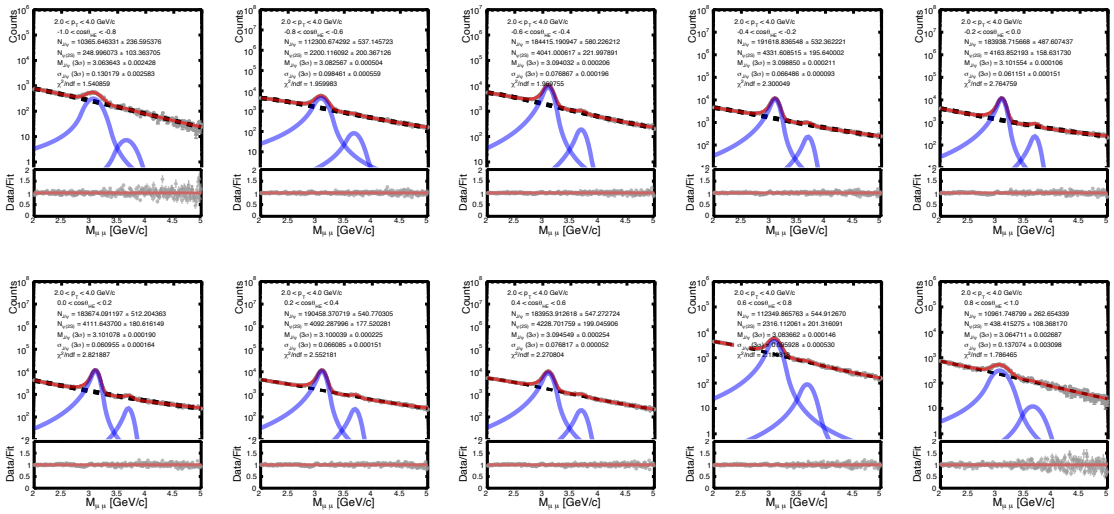

Figure 6.12: Double Crystal Ball + variable width Gaussian function fit to the invariant mass spectra for various $cos\theta$ ranges for $2.0 < p_{\mathrm{T}} < 4.0$ GeV/c in the helicity frame [123].

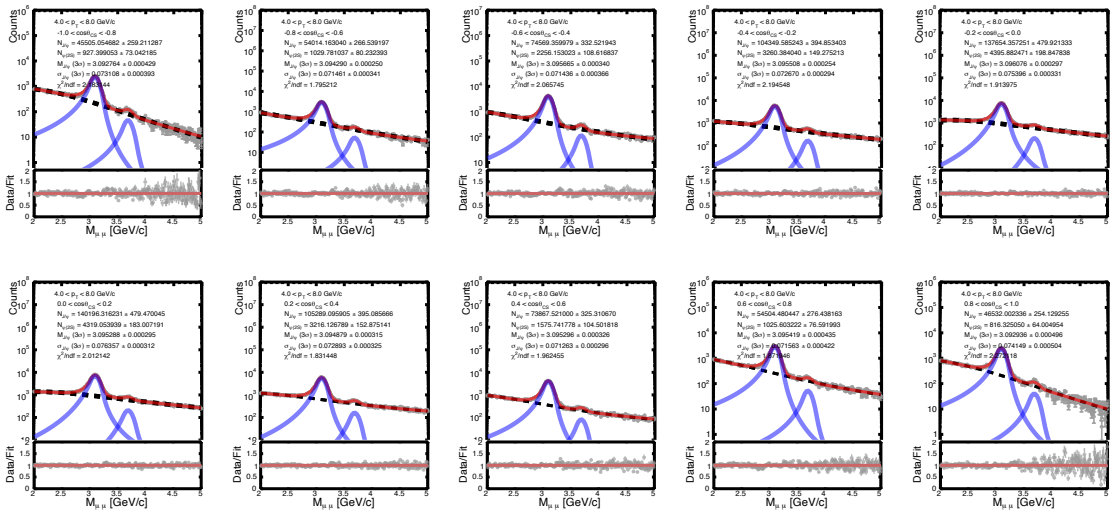

Figure 6.13: Double Crystal Ball + variable width Gaussian function fit to the invariant mass spectra for various $cos\theta$ ranges for $4.0 < p_{\mathrm{T}} < 8.0$ GeV/c in the Collin-Soper frame [123].

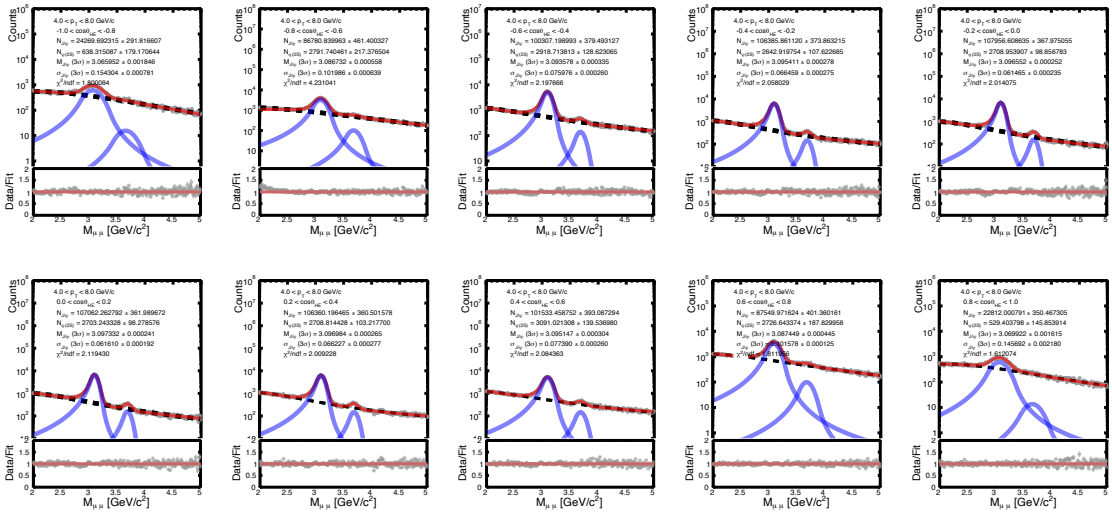

Figure 6.14: Double Crystal Ball + variable width Gaussian function fit to the invariant mass spectra for various $cos\theta$ ranges for $4.0 < p_{\mathrm{T}} < 8.0$ GeV/c in the helicity frame [123].

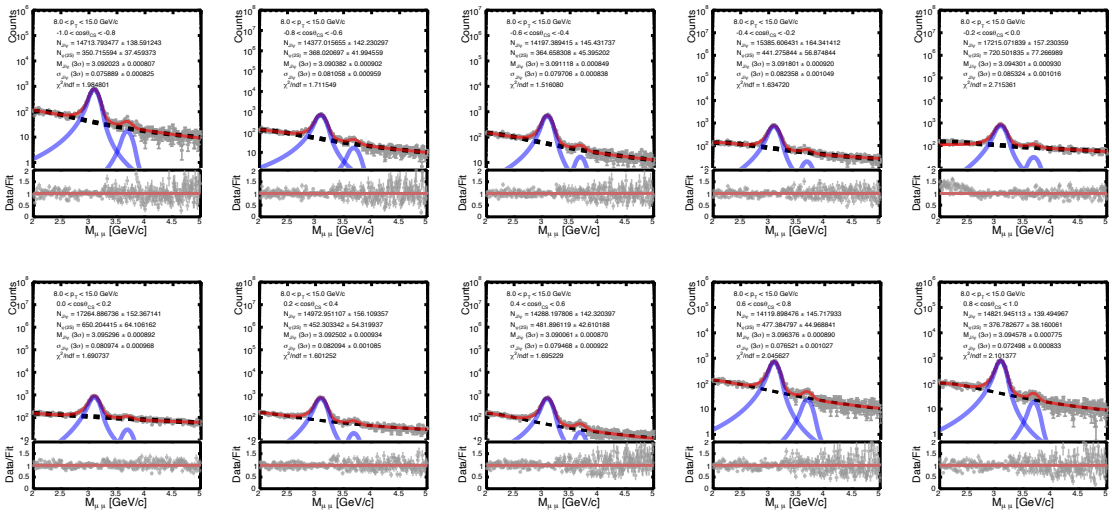

Figure 6.15: Double Crystal Ball + variable width Gaussian function fit to the invariant mass spectra for various $cos\theta$ ranges for $8.0 < p_{\mathrm{T}} < 15.0$ GeV/c in the Collin-Soper frame [123].

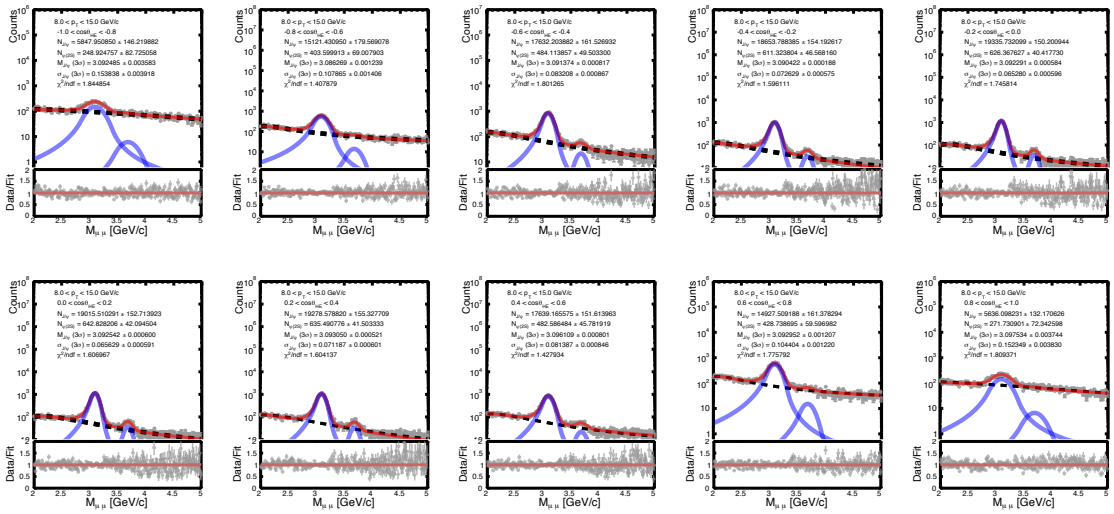

Figure 6.16: Double Crystal Ball + variable width Gaussian function fit to the invariant mass spectra for various $cos\theta$ ranges for $8.0 < p_{\mathrm{T}} < 15.0$ GeV/c in the helicity frame [123].

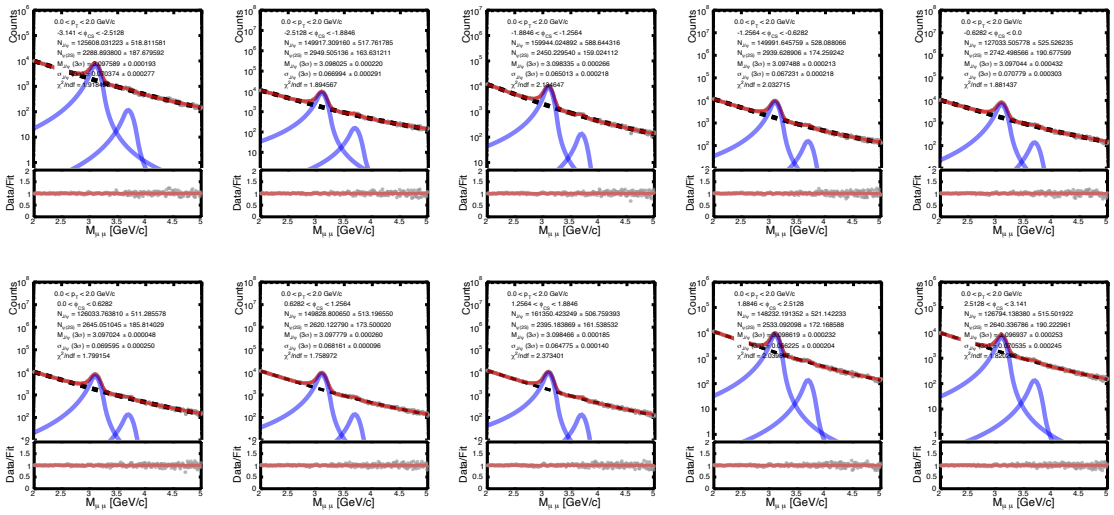

Figure 6.17: Double Crystal Ball + variable width Gaussian function fit to the invariant mass spectra for various ϕ ranges for $0.0 < p_{\mathrm{T}} < 2.0$ GeV/c in the Collin-Soper frame [123].

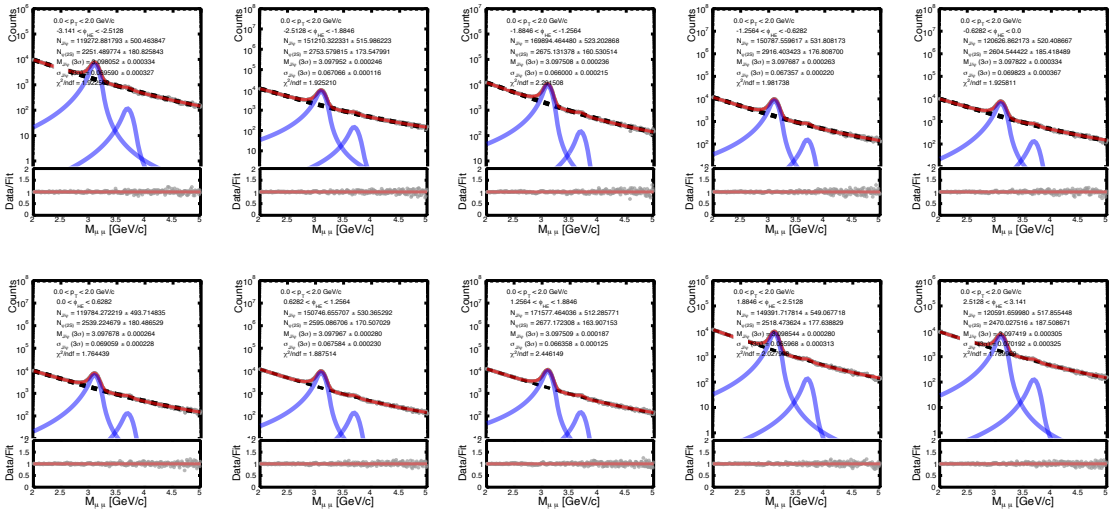

Figure 6.18: Double Crystal Ball + variable width Gaussian function fit to the invariant mass spectra for various ϕ ranges for $0.0 < p_{\mathrm{T}} < 2.0$ GeV/c in the helicity frame [123].

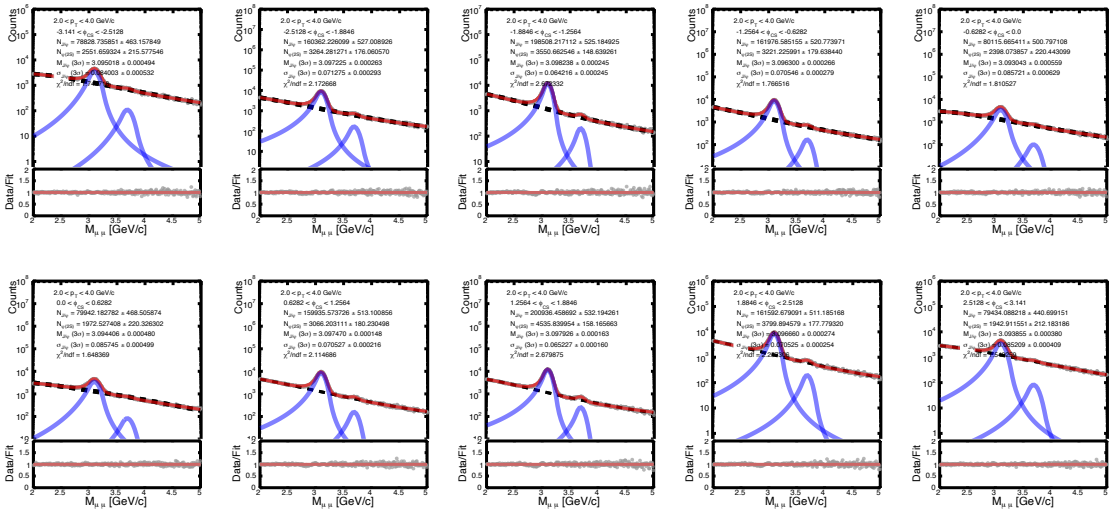

Figure 6.19: Double Crystal Ball + variable width Gaussian function fit to the invariant mass spectra for various ϕ ranges for $2.0 < p_{\mathrm{T}} < 4.0$ GeV/c in the Collin-Soper frame [123].

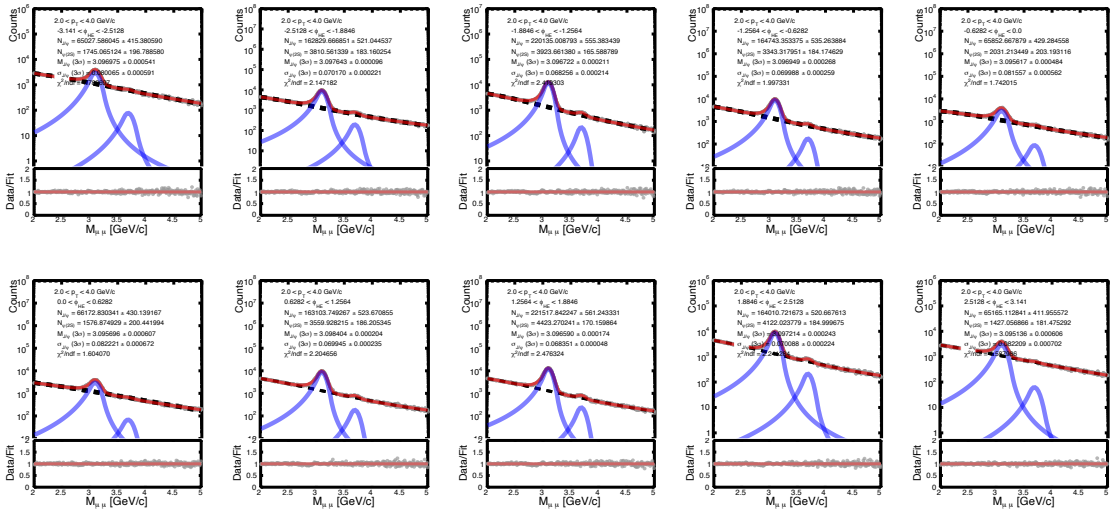

Figure 6.20: Double Crystal Ball + variable width Gaussian function fit to the invariant mass spectra for various ϕ ranges for $2.0 < p_{\mathrm{T}} < 4.0$ GeV/c in the helicity frame [123].

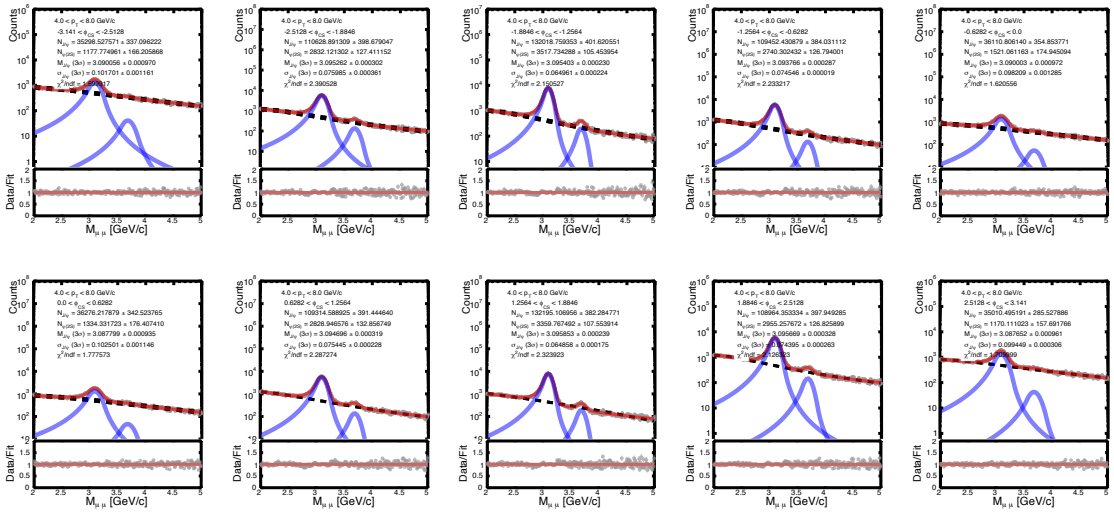

Figure 6.21: Double Crystal Ball + variable width Gaussian function fit to the invariant mass spectra for various ϕ ranges for $4.0 < p_{\mathrm{T}} < 8.0$ GeV/c in the Collin-Soper frame [123].

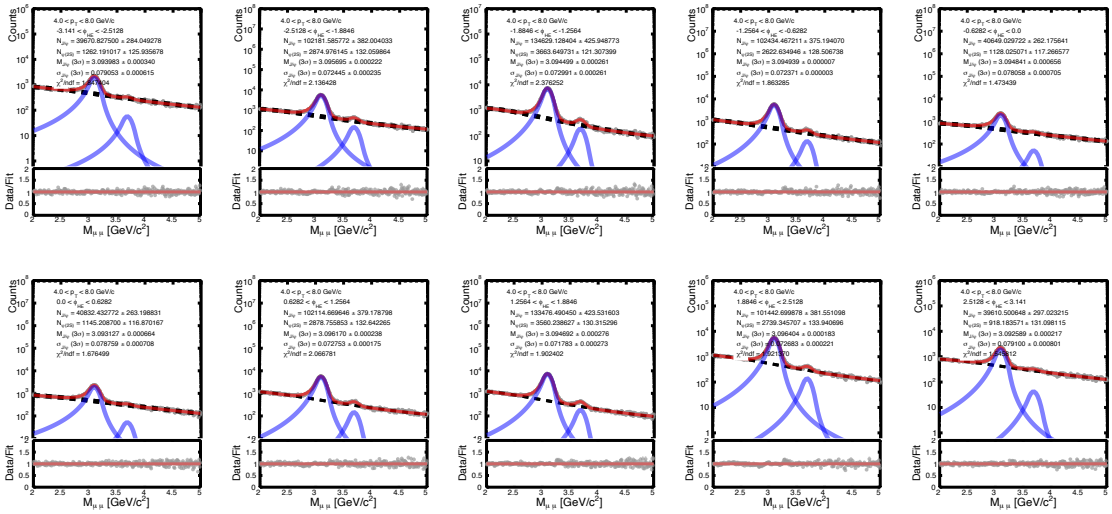

Figure 6.22: Double Crystal Ball + variable width Gaussian function fit to the invariant mass spectra for various ϕ ranges for $4.0 < p_{\mathrm{T}} < 8.0$ GeV/c in the helicity frame [123].

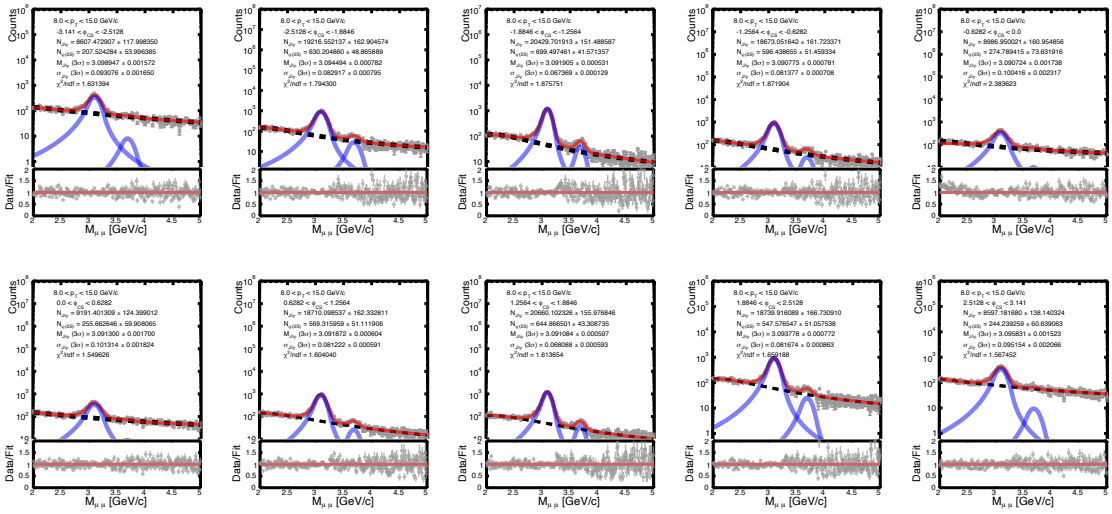

Figure 6.23: Double Crystal Ball + variable width Gaussian function fit to the invariant mass spectra for various ϕ ranges for $8.0 < p_{\mathrm{T}} < 15.0$ GeV/c in the Collin-Soper frame [123].

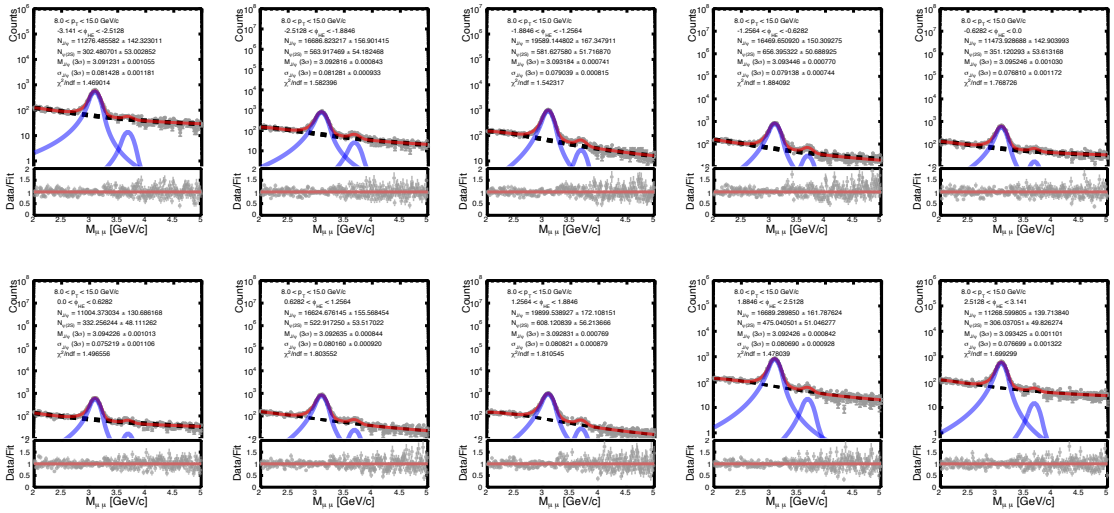

Figure 6.24: Double Crystal Ball + variable width Gaussian function fit to the invariant mass spectra for various ϕ ranges for $8.0 < p_{\mathrm{T}} < 15.0$ GeV/c in the helicity frame [123].

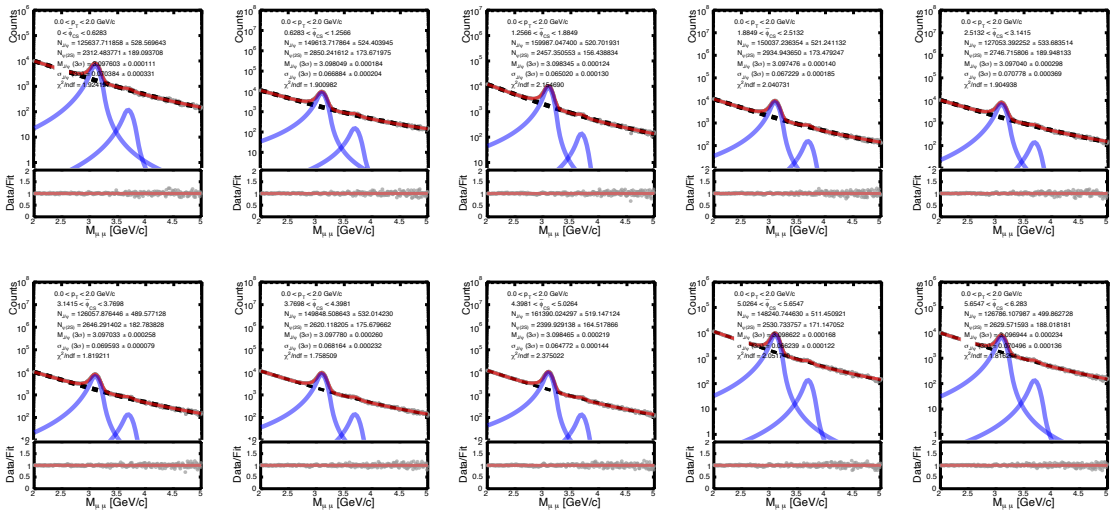

Figure 6.25: Double Crystal Ball + variable width Gaussian function fit to the invariant mass spectra for various $\tilde{\phi}$ ranges for $0.0 < p_{\mathrm{T}} < 2.0$ GeV/c in the Collin-Soper frame [123].

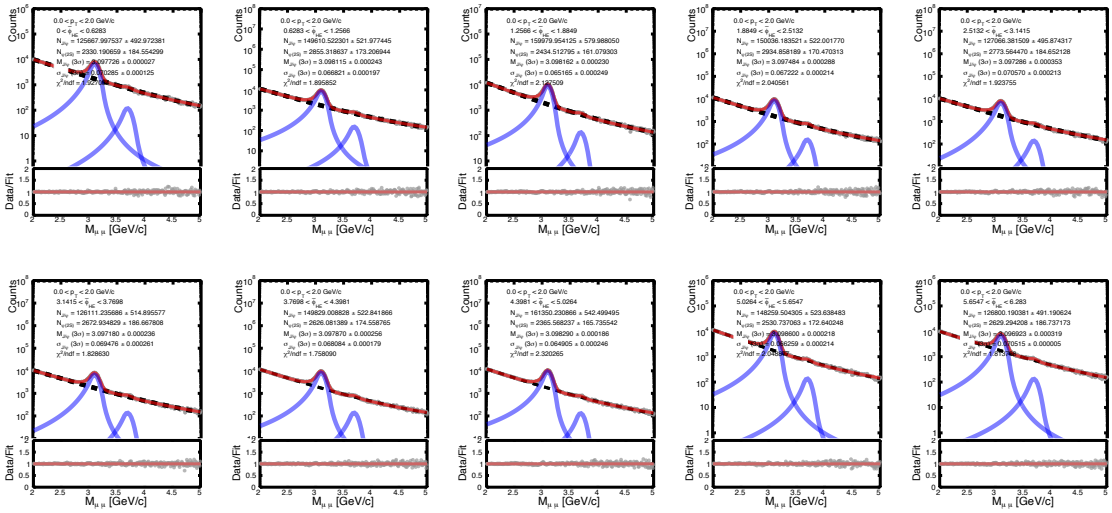

Figure 6.26: Double Crystal Ball + variable width Gaussian function fit to the invariant mass spectra for various $\tilde{\phi}$ ranges for $0.0 < p_{\mathrm{T}} < 2.0$ GeV/c in the helicity frame [123].

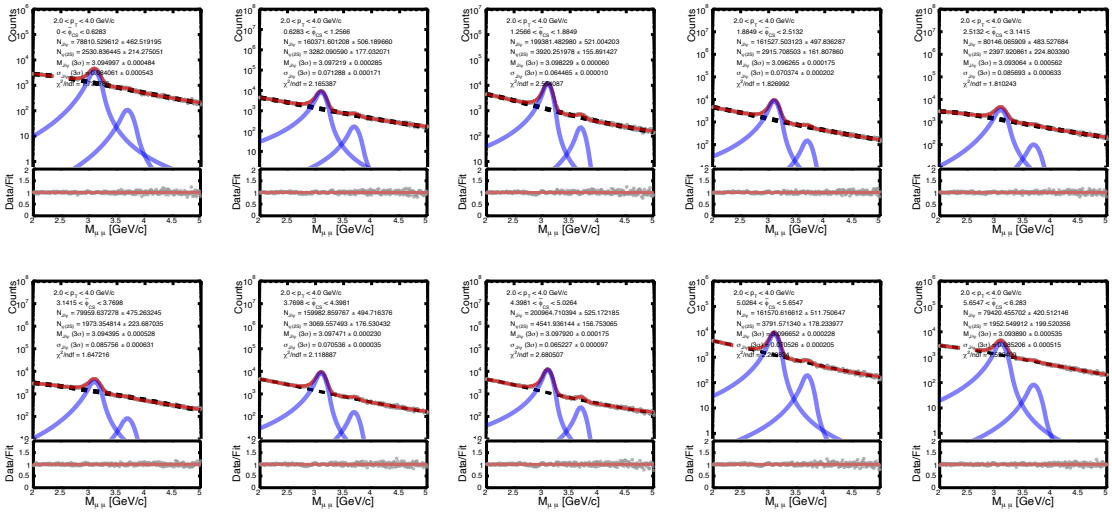

Figure 6.27: Double Crystal Ball + variable width Gaussian function fit to the invariant mass spectra for various $\tilde{\phi}$ ranges for $2.0 < p_{\mathrm{T}} < 4.0$ GeV/c in the Collin-Soper frame [123].

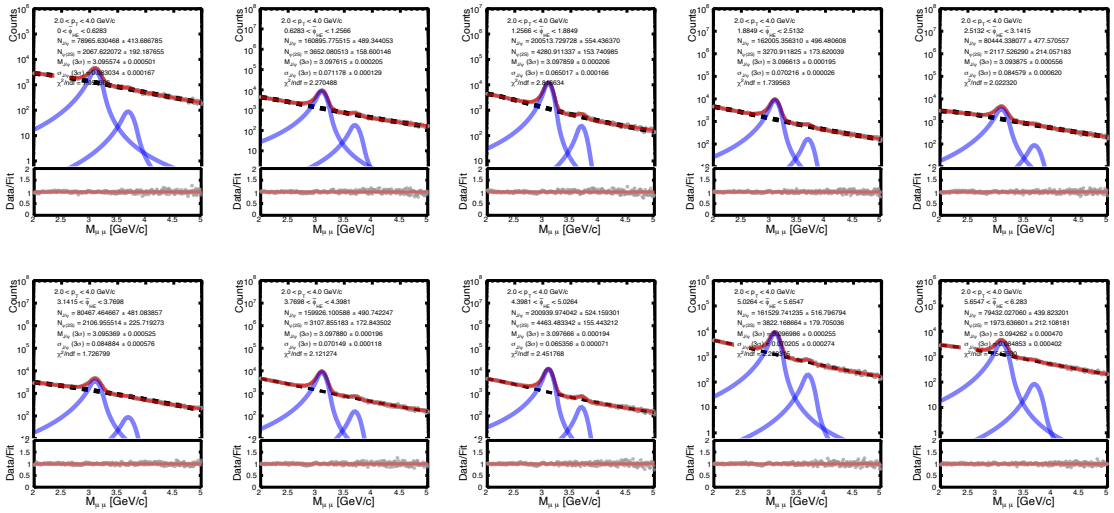

Figure 6.28: Double Crystal Ball + variable width Gaussian function fit to the invariant mass spectra for various $\tilde{\phi}$ ranges for $2.0 < p_{\mathrm{T}} < 4.0$ GeV/c in the helicity frame [123].

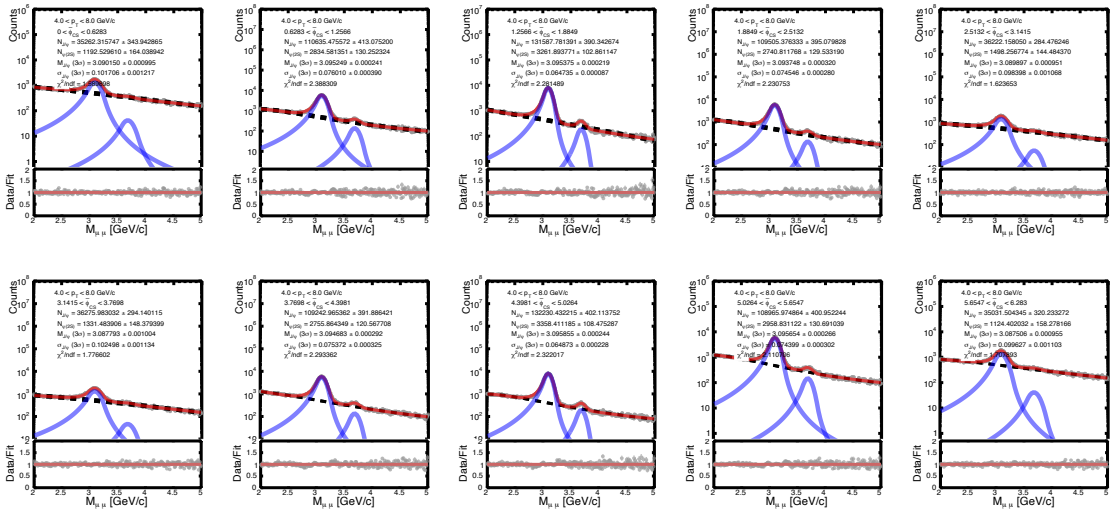

Figure 6.29: Double Crystal Ball + variable width Gaussian function fit to the invariant mass spectra for various $\tilde{\phi}$ ranges for $4.0 < p_{\mathrm{T}} < 8.0$ GeV/c in the Collin-Soper frame [123].

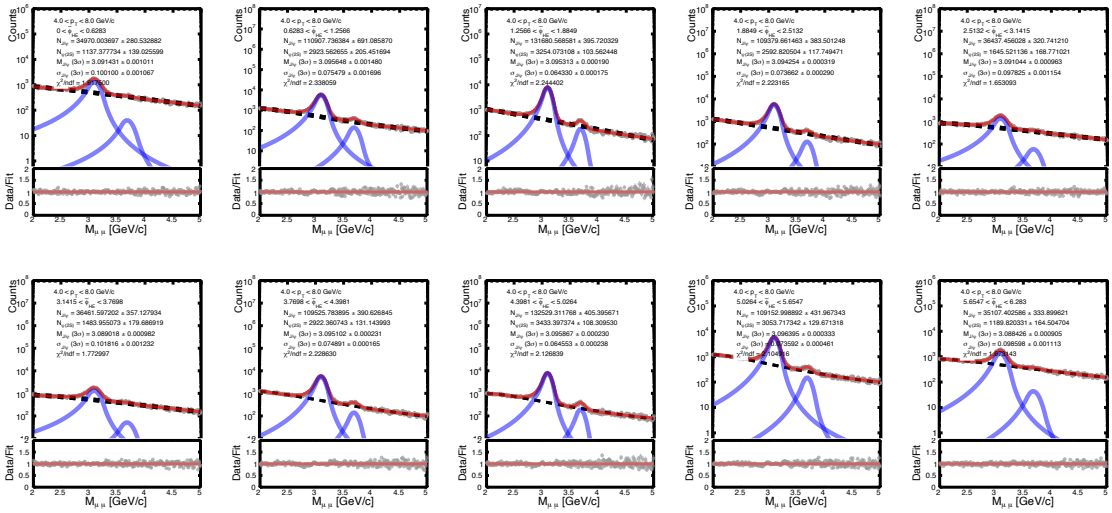

Figure 6.30: Double Crystal Ball + variable width Gaussian function fit to the invariant mass spectra for various $\tilde{\phi}$ ranges for $4.0 < p_{\mathrm{T}} < 8.0$ GeV/c in the helicity frame [123].

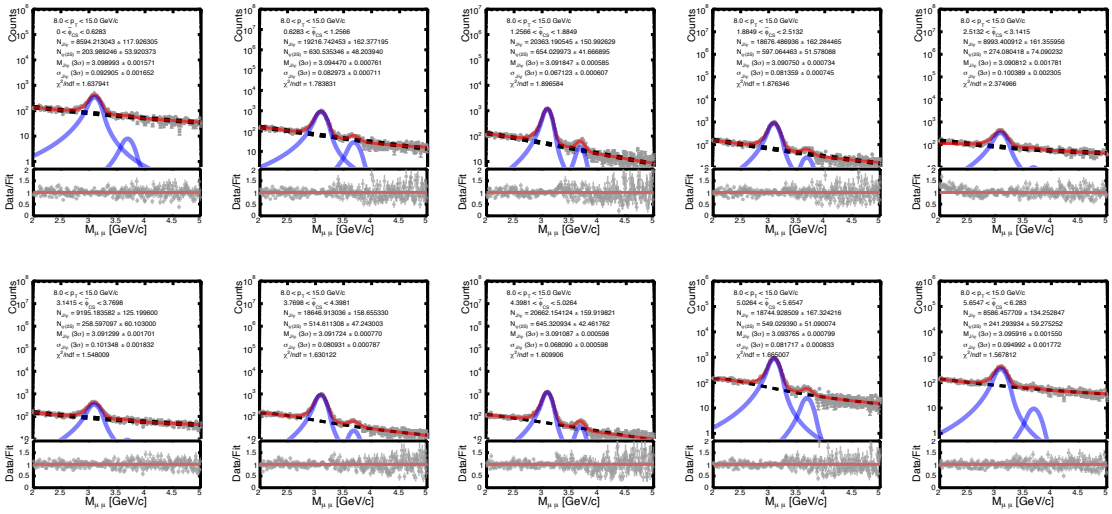

Figure 6.31: Double Crystal Ball + variable width Gaussian function fit to the invariant mass spectra for various $\tilde{\phi}$ ranges for $8.0 < p_{\mathrm{T}} < 15.0$ GeV/c in the Collin-Soper frame [123].

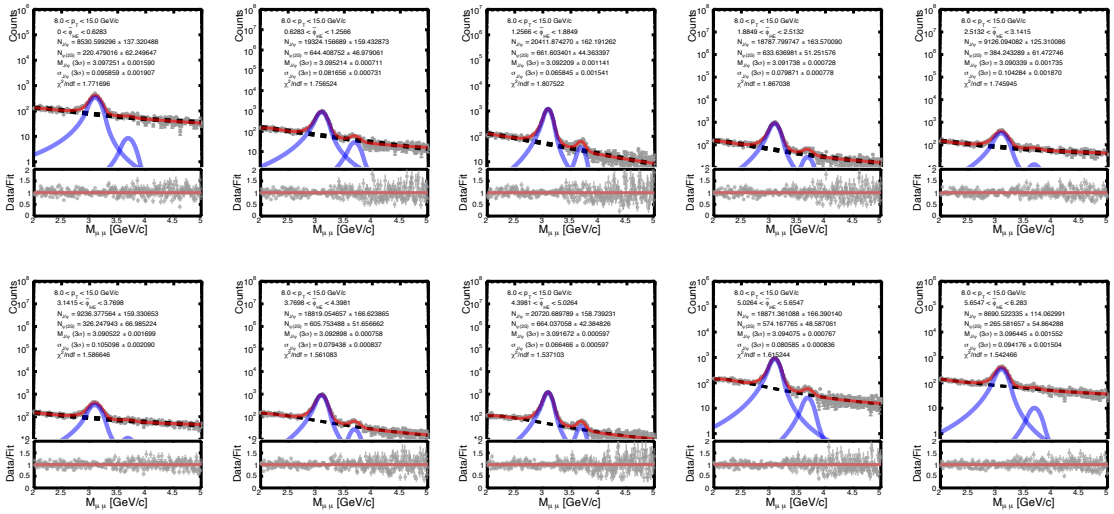

Figure 6.32: Double Crystal Ball + variable width Gaussian function fit to the invariant mass spectra for various $\tilde{\phi}$ ranges for $8.0 < p_{\mathrm{T}} < 15.0$ GeV/c in the helicity frame [123].

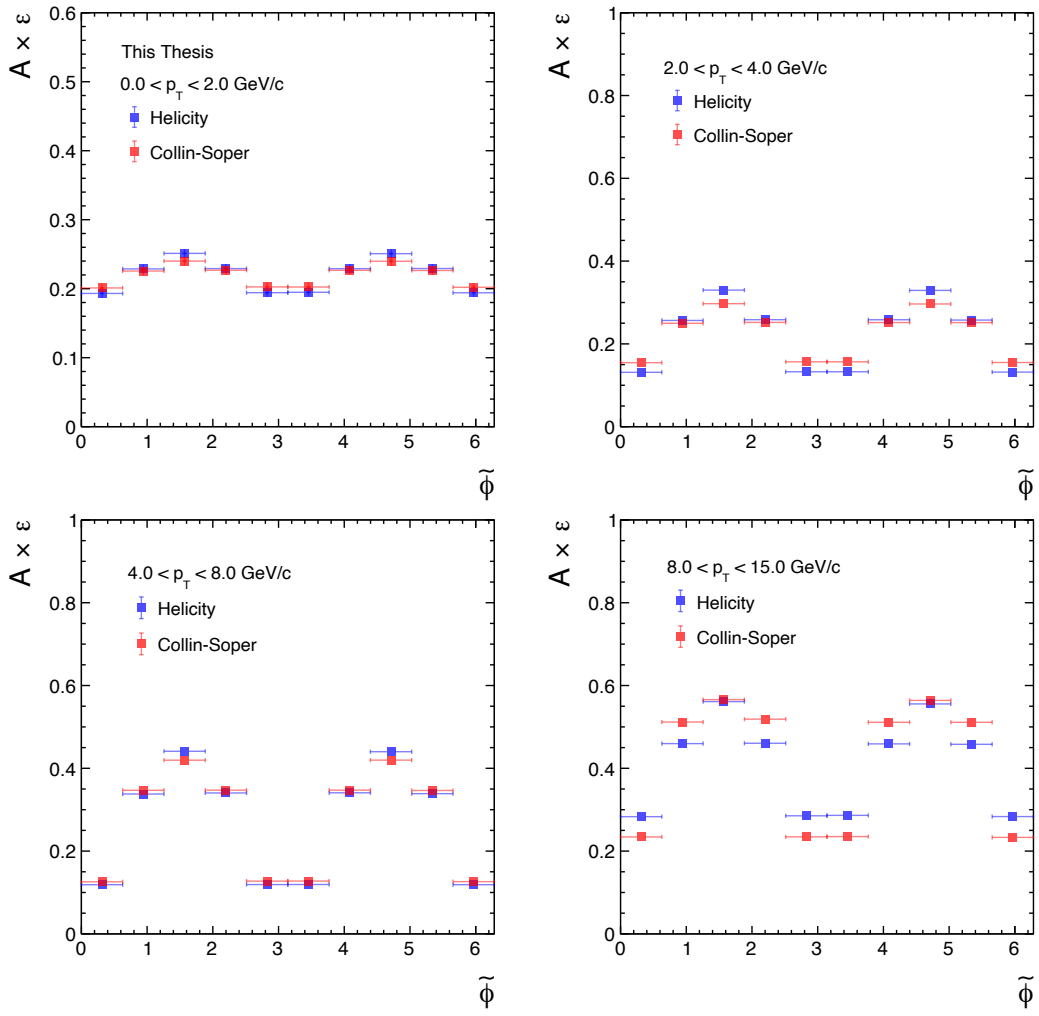

Figure 6.33: Acceptance times efficiency as a function of $\tilde{\phi}$ in both helicity and Collin-Soper frames for four different p_{T} bins [123].

Bibliography

[1] H. D. Politzer, Phys. Rev. Lett. **30**, 1346 (1973).

[2] R. L. Workman *et al.* [Particle Data Group], PTEP **2022**, 083C01 (2022).

[3] https://particlesandfriends.wordpress.com/2016/10/14/evolution-of-collisions-and-qgp/

[4] https://indico.jinr.ru/event/299/?ovw=True

[5] V. Khachatryan *et al.* [CMS], JHEP **04**, 039 (2017).

[6] B. B. Abelev *et al.* [ALICE], Phys. Lett. B **728**, 216 (2014).

[7] S. Acharya *et al.* [ALICE], [arXiv:2303.13361].

[8] B. Sahlmüller [ALICE], Nucl. Phys. A **956**, 421 (2016).

[9] G. D. Moore and D. Teaney, Phys. Rev. C **71**, 064904 (2005).

[10] H. van Hees, V. Greco and R. Rapp, Phys. Rev. C **73**, 034913 (2006).

[11] K. Goswami, D. Sahu and R. Sahoo, Phys. Rev. D **107**, 014003 (2023).

[12] J. Adam *et al.* [ALICE], Nature Phys. **13**, 535 (2017).

[13] S. Acharya *et al.* [ALICE], Eur. Phys. J. C **80**, 693 (2020).

[14] V. Khachatryan *et al.* [CMS], Phys. Lett. B **765**, 193 (2017).

[15] C. R. Singh, S. Deb, R. Sahoo and J. e. Alam, Eur. Phys. J. C **82**, 542 (2022).

[16] J. Adam *et al.* [STAR], Phys. Rev. D **102**, 092009 (2020).

[17] T. Affolder *et al.* [CDF], Phys. Rev. Lett. **85**, 2886 (2000).

[18] S. Chatrchyan *et al.* [CMS], Phys. Lett. B **727**, 381 (2013).

[19] R. Aaij *et al.* [LHCb], Eur. Phys. J. C **73**, 2631 (2013).

[20] R. Aaij *et al.* [LHCb], Eur. Phys. J. C **74**, 2872 (2014).

[21] M. Butenschoen and B. A. Kniehl, Phys. Rev. Lett. **108**, 172002 (2012).

[22] S. Borsanyi, Z. Fodor, C. Hoelbling, S. D. Katz, S. Krieg and K. K. Szabo, Phys. Lett. B **730**, 99 (2014).

[23] A. Bazavov *et al.* [HotQCD], Phys. Rev. D **86**, 034509 (2012).

[24] R. Marty, E. Bratkovskaya, W. Cassing, J. Aichelin and H. Berrehrah, Phys. Rev. C **88**, 045204 (2013).

[25] C. Ratti, S. Roessner, M. A. Thaler and W. Weise, Eur. Phys. J. C **49**, 213 (2007).

[26] W. Cassing and E. L. Bratkovskaya, Nucl. Phys. A **831**, 215 (2009).

[27] O. Soloveva, J. Aichelin and E. Bratkovskaya, Phys. Rev. D **105**, 054011 (2022).

[28] R. Rougemont, R. Critelli, J. Noronha-Hostler, J. Noronha and C. Ratti, Phys. Rev. D **96**, 014032 (2017).

[29] M. A. Braun, J. Dias de Deus, A. S. Hirsch, C. Pajares, R. P. Scharenberg and B. K. Srivastava, Phys. Rept. **599**, 1 (2015).

[30] R. Bellwied, S. Borsanyi, Z. Fodor, S. D. Katz, A. Pasztor, C. Ratti and K. K. Szabo, Phys. Rev. D **92**, 114505 (2015).

[31] C. R. Allton, M. Doring, S. Ejiri, S. J. Hands, O. Kaczmarek, F. Karsch, E. Laermann and K. Redlich, Phys. Rev. D **71**, 054508 (2005).

[32] P. de Forcrand and O. Philipsen, Nucl. Phys. B **642**, 290 (2002).

[33] Z. Fodor and S. D. Katz, JHEP **03**, 014 (2002).

[34] R. Bellwied, S. Borsanyi, Z. Fodor, S. D. Katz and C. Ratti, Phys. Rev. Lett. **111**, 202302 (2013).

[35] Y. Sakai, T. Sasaki, H. Kouno and M. Yahiro, J. Phys. G: Nucl. Part. Phys. **39**, 035004 (2012).

[36] L. Yang and X. J. Wen, Phys. Rev. D **104**, 114010 (2021).

[37] H. Satz, Rept. Prog. Phys. **63**, 1511 (2000).

[38] I. Bautista, C. Pajares, J. G. Milhano and J. Dias de Deus, Phys. Rev. C **86**, 034909 (2012).

[39] D. Sahu, S. Tripathy, R. Sahoo and S. K. Tiwari, Eur. Phys. J. A **58**, 78 (2022).

[40] M. A. Braun and C. Pajares, Eur. Phys. J. C **16**, 349 (2000).

[41] C. Loizides, J. Kamin and D. d'Enterria, Phys. Rev. C **97**, 054910 (2018).

[42] L. McLerran, M. Praszalowicz and B. Schenke, Nucl. Phys. A **916**, 210 (2013).

[43] M. A. Braun, F. del Moral and C. Pajares, Nucl. Phys. A **715**, 791 (2003).

[44] S. W. Hawking, Commun. Math. Phys. **43**, 199 (1975).

[45] W. G. Unruh, Phys. Rev. D **14**, 870 (1976).

[46] P. Castorina, D. Kharzeev and H. Satz, Eur. Phys. J. C **52**, 187 (2007).

[47] J. S. Schwinger, Phys. Rev. **128**, 2425 (1962).

[48] P. Sahoo, S. K. Tiwari, S. De, R. Sahoo, R. P. Scharenberg and B. K. Srivastava, Mod. Phys. Lett. A **34**, 1950034 (2019).

[49] F. Becattini, P. Castorina, A. Milov and H. Satz, Eur. Phys. J. C **66**, 377 (2010).

[50] D. Sahu and R. Sahoo, J. Phys. G: Nucl. Part. Phys. **48**, 125104 (2021).

[51] S. Acharya *et al.* [ALICE], Phys. Lett. B **807**, 135501 (2020).

[52] S. Acharya *et al.* [ALICE], Phys. Rev. C **99**, 024906 (2019).

[53] B. Abelev *et al.* [ALICE], Phys. Rev. C **88**, 044910 (2013).

[54] S. Acharya *et al.* [ALICE], Phys. Rev. C **101**, 044907 (2020).

[55] S. Acharya *et al.* [ALICE], Phys. Lett. B **800**, 135043 (2020).

[56] S. Acharya *et al.* [ALICE], Phys. Lett. B **790**, 35 (2019).

[57] S. Acharya *et al.* [ALICE], Eur. Phys. J. C **79**, 307 (2019).

[58] J. D. Bjorken, Phys. Rev. D **27**, 140 (1983).

[59] N. Sarkar and P. Ghosh, Phys. Rev. C **96**, 044901 (2017).

[60] D. Sahu, S. Tripathy, R. Sahoo and A. R. Dash, Eur. Phys. J. A **56**, 187 (2020).

[61] P. Kovtun, D. T. Son and A. O. Starinets, Phys. Rev. Lett. **94**, 111601 (2005).

[62] L. P. Csernai, J. I. Kapusta and L. D. McLerran, Phys. Rev. Lett. **97**, 152303 (2006).

[63] S. K. Tiwari, P. K. Srivastava and C. P. Singh, Phys. Rev. C **85**, 014908 (2012).

[64] B. Mohanty and V. Roy, Curr. Sci. **103**, 1267 (2012).

[65] T. Hirano and M. Gyulassy, Nucl. Phys. A **769**, 71 (2006).

[66] A. Bazavov *et al.* [HotQCD], Phys. Rev. D **90**, 094503 (2014).

[67] A. Bazavov, T. Bhattacharya, M. Cheng, N. H. Christ, C. DeTar, S. Ejiri, S. Gottlieb, R. Gupta, U. M. Heller and K. Huebner, *et al.* Phys. Rev. D **80**, 014504 (2009).

[68] K. Dusling and T. Schäfer, Phys. Rev. C **85**, 044909 (2012).

[69] F. Karsch, D. Kharzeev and K. Tuchin, Phys. Lett. B **663**, 217 (2008).

[70] M. Mukherjee, S. Basu, A. Chatterjee, S. Chatterjee, S. P. Adhya, S. Thakur and T. K. Nayak, Phys. Lett. B **784**, 1 (2018).

[71] S. Acharya *et al.* [ALICE], Eur. Phys. J. C **81**, 1012 (2021).

[72] S. Mrowczynski, Phys. Lett. B **430**, 9 (1998).

[73] A. Khuntia, S. K. Tiwari, P. Sharma, R. Sahoo and T. K. Nayak, Phys. Rev. C **100**, 014910 (2019).

[74] Rana A. Fine, Frank J. Millero, J. Chem. Phys. **59**, 5529 (1973).

[75] Hugh D. Young; Roger A. Freedman, University Physics with Modern Physics, Addison-Wesley, pp. 356 (2012).

[76] R. Baier and Y. Mehtar-Tani, Phys. Rev. C **78**, 064906 (2008).

[77] J. Casalderrey-Solana and X. N. Wang, Phys. Rev. C **77**, 024902 (2008).

[78] A. Majumder, B. Muller and X. N. Wang, Phys. Rev. Lett. **99**, 192301 (2007).

[79] H. Liu, K. Rajagopal and U. A. Wiedemann, Phys. Rev. Lett. **97**, 182301 (2006).

[80] K. M. Burke *et al.* [JET], Phys. Rev. C **90**, 014909 (2014).

[81] A. N. Mishra, D. Sahu and R. Sahoo, MDPI Physics **4**, 315 (2022).

[82] R. Baier, Nucl. Phys. A **715**, 209 (2003).

[83] A. N. Mishra, G. Paić, C. Pajares, R. P. Scharenberg and B. K. Srivastava, Eur. Phys. J. A **57**, 245 (2021).

[84] M. Gyulassy, P. Levai and I. Vitev, Nucl. Phys. B **571**, 197 (2000).

[85] A. Buzzatti and M. Gyulassy, Phys. Rev. Lett. **108**, 022301 (2012).

[86] X. f. Guo and X. N. Wang, Phys. Rev. Lett. **85**, 3591 (2000).

[87] A. Majumder, Phys. Rev. D **85**, 014023 (2012).

[88] B. Schenke, C. Gale and S. Jeon, Phys. Rev. C **80**, 054913 (2009).

[89] P. B. Arnold, G. D. Moore and L. G. Yaffe, JHEP **11**, 057 (2001).

[90] R. Scaria, C. R. Singh and R. Sahoo, [arXiv:2208.14792].

[91] S. Singha, B. Mohanty and Z. W. Lin, Int. J. Mod. Phys. E **24**, 1550041 (2015).

[92] S. Acharya *et al.* [ALICE], Phys. Lett. B **802**, 135225 (2020).

[93] M. J. Matison, A. Barbaro-Galtieri, M. Alston-Garnjost, S. M. Flatte, J. H. Friedman, G. R. Lynch, M. S. Rabin and F. T. Solmitz, Phys. Rev. D **9**, 1872 (1974).

[94] S. D. Protopopescu, M. Alston-Garnjost, A. Barbaro-Galtieri, S. M. Flatte, J. H. Friedman, T. A. Lasinski, G. R. Lynch, M. S. Rabin and F. T. Solmitz, Phys. Rev. D **7**, 1279 (1973)

[95] D. Sahu, S. Tripathy, G. S. Pradhan and R. Sahoo, Phys. Rev. C **101**, 014902 (2020).

[96] J. Adams *et al.* [STAR], Phys. Rev. C **71**, 064902 (2005).

[97] M. M. Aggarwal *et al.* [STAR], Phys. Rev. C **84**, 034909 (2011).

[98] S. Acharya *et al.* [ALICE], Phys. Rev. C **99**, 024906 (2019).

[99] J. Adam *et al.* [ALICE], Phys. Rev. C **95**, 064606 (2017).

[100] J. Adam *et al.* [ALICE], Eur. Phys. J. C **76**, 245 (2016).

[101] B. Alver *et al.* [PHOBOS], Phys. Rev. C **83**, 024913 (2011).

[102] J. Cleymans and D. Worku, J. Phys. G **39**, 025006 (2012).

[103] E. Schnedermann, J. Sollfrank and U. W. Heinz, Phys. Rev. C **48**, 2462 (1993).

[104] K. Adcox *et al.* [PHENIX], Phys. Rev. C **69**, 024904 (2004).

[105] D. Thakur, S. De, R. Sahoo and S. Dansana, Phys. Rev. D **97**, 094002 (2018).

[106] N. Sharma, J. Cleymans, B. Hippolyte and M. Paradza, Phys. Rev. C **99**, 044914 (2019).

[107] P. Faccioli, C. Lourenco, J. Seixas and H. K. Wohri, Eur. Phys. J. C **69**, 657 (2010).

[108] B. Sahoo, D. Sahu, S. Deb, C. R. Singh and R. Sahoo, Phys. Rev. C **109**, 034910 (2024)

[109] L. Evans and P. Bryant, JINST **3**, S08001 (2008).

[110] G. Aad *et al.* [ATLAS], JINST **3**, S08003 (2008).

[111] S. Chatrchyan *et al.* [CMS], JINST **3**, S08004 (2008).

[112] A. A. Alves, Jr. *et al.* [LHCb], JINST **3**, S08005 (2008).

[113] K. Aamodt *et al.* [ALICE], JINST **3**, S08002 (2008).

[114] [ALICE Collaboration], "ALICE technical design report of the dimuon forward spectrometer," CERN-LHCC-99-22.

[115] G. T. Bodwin, E. Braaten and G. P. Lepage, Phys. Rev. D **51**, 1125-1171 (1995) [erratum: Phys. Rev. D **55**, 5853 (1997)].

[116] E. Braaten, B. A. Kniehl and J. Lee, Phys. Rev. D **62**, 094005 (2000).

[117] B. Abelev *et al.* [ALICE], Phys. Rev. Lett. **108**, 082001 (2012).

[118] Y. Q. Ma, T. Stebel and R. Venugopalan, JHEP **12**, 057 (2018).

[119] V. Cheung and R. Vogt, Phys. Rev. D **98**, 114029 (2018).

[120] M. Ambrogiani *et al.* [E835], Phys. Rev. D **65**, 052002 (2002).

[121] J. Z. Bai *et al.* [BES], Phys. Lett. B **591**, 42 (2004).

[122] M. Ambrogiani *et al.* [E835], Phys. Lett. B **610**, 177 (2005).

[123] D. Sahu and R. Sahoo, https://alice-notes.web.cern.ch/node/1472 (ALICE internal).

[124] B. Gong, L. P. Wan, J. X. Wang and H. F. Zhang, Phys. Rev. Lett. **110**, 042002 (2013).

[125] M. Guittière, https://alice-notes.web.cern.ch/node/1043 (ALICE internal).

[126] A. Morreale, https://alice-notes.web.cern.ch/system/files/notes/analysis/497/2017-Aug-11-analysis_note-pp13TeV-analysis_note.pdf (ALICE internal).